Charge-state-resolved spectroscopy of multiply-charged tin ions

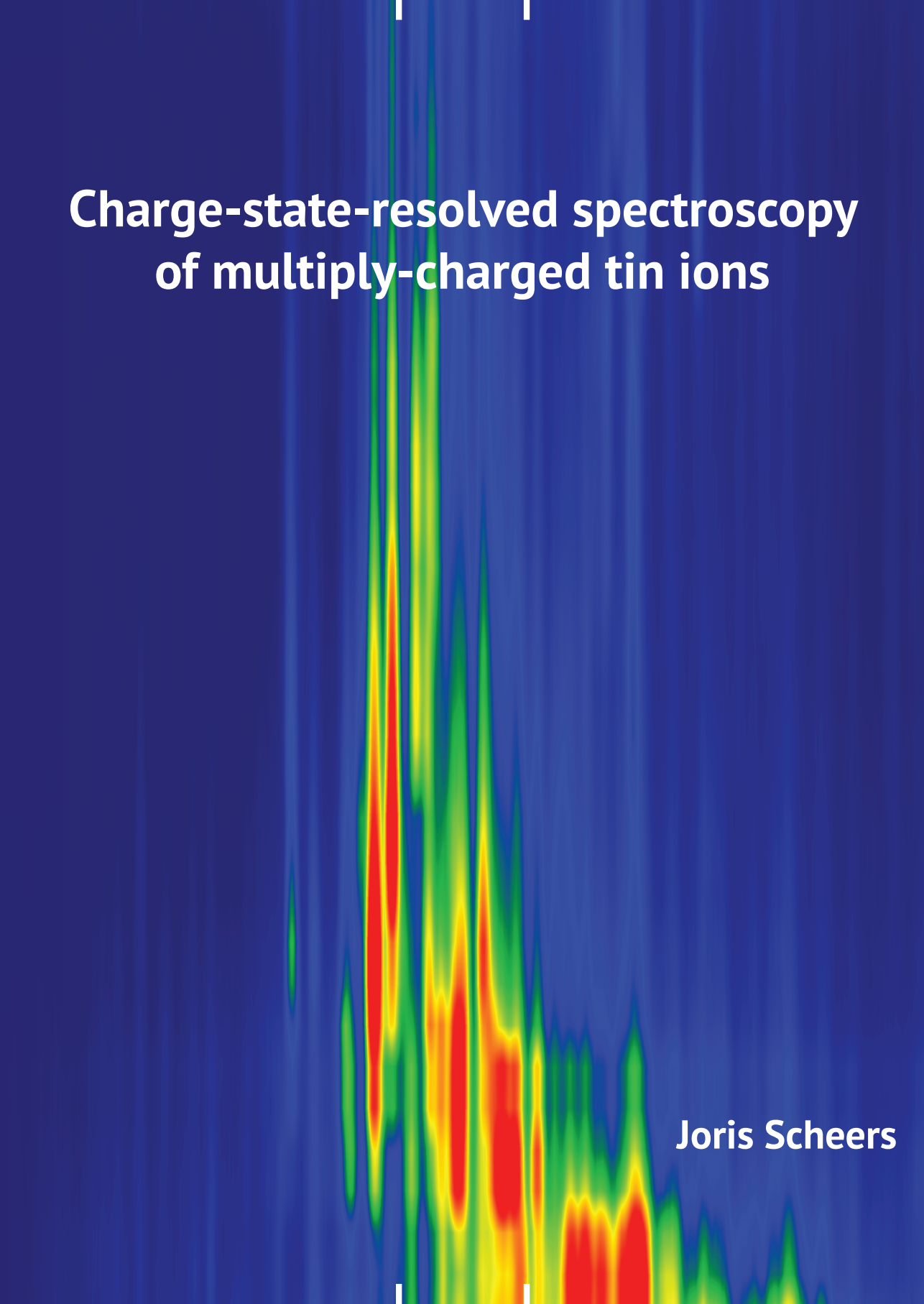

Joris Scheers

VRIJE UNIVERSITEIT

CHARGE-STATE-RESOLVED SPECTROSCOPY OF MULTIPLY-CHARGED TIN IONS

ACADEMISCH PROEFSCHRIFT

ter verkrijging van de graad Doctor
aan de Vrije Universiteit Amsterdam,
op gezag van de rector magnificus
prof.dr. V. Subramaniam,
in het openbaar te verdedigen
ten overstaan van de promotiecommissie
van de Faculteit der Bètawetenschappen
op dinsdag 10 november 2020 om 13.45 uur
in de aula van de universiteit,
De Boelelaan 1105

door

Joris Scheers

geboren te Goes

promotoren: dr. O.O. Versolato
prof.dr.ir. R.A. Hoekstra
prof.dr. W.M.G. Ubachs

This thesis was approved by the members of the reviewing committee:

prof.dr. A. Borschevsky (University of Groningen)
prof.dr. M.L. Groot (Vrije Universiteit Amsterdam)
prof.dr.ir. H.B. van Linden van den Heuvell (University of Amsterdam)
prof.dr. G. O'Sullivan (University College Dublin)
dr. W.J. van der Zande (ASML)

The research reported in this thesis was carried out at the Advanced Research Center for Nanolithography (ARCNL), a public-private partnership between the University of Amsterdam (UvA), Vrije Universiteit Amsterdam (VU Amsterdam), the Netherlands Organization for Scientific Research (NWO), and the semiconductor equipment manufacturer ASML.

Cover: Spectral intensity map of the emission from Sn ions, constructed from measurements taken at an electron-beam ion trap at the Max-Planck-Institut für Kernphysik in Heidelberg, Germany. See Chapter 1 for more information. The white vertical bars indicate a 2% bandwidth centered at 13.5 nm wavelength corresponding to the wavelength band that can be reflected by the multilayer mirrors used in nanolithographic applications.

ISBN: 978-94-92323-39-2

Contents

Introduction

The invention of the transistor in 1947 [1] was one of the most significant inventions of the 20th century, for which a Nobel prize in physics was awarded to Shockley, Bardeen and Brattain in 1956. Transistors are embedded into integrated circuits that form the basis of nearly all electronic equipment that we use every day, such as mobile phones, computers, cars, laundry machines, and other household equipment. The Apollo guidance computer, responsible for landing the first men on the moon in 1969, had a random access memory (RAM) of just 4 kilobytes and a read only memory (ROM) of 72 kilobytes [2]. A typical mobile phone nowadays has several gigabytes of RAM and tens of gigabytes of ROM. This considerable progress was made possible by the systematic shrinking of the transistor due to technological progress. Gordon Moore, one of the founders of the Intel corporation, predicted in 1965 that the amount of transistors on an affordable chip would double roughly every year [3]. This trend was revised in 1975, by Moore, to a doubling every two years [4]. This trend became known as Moore's law and it is seen as a driving force for progress in the semiconductor industry. To this day, Moore's law has been maintained despite numerous predictions of that it would end.

The economics of Moore's law tends to be favorable to both consumers and producers of semiconductor products. The customer is able to buy more powerful hardware at a lower price than previous generations, while semiconductor manufacturers are able to sell more transistors, as innovations often need more computing power at a manageable energy consumption. Microelectronic devices are manufactured using a repetitive process in which thin layers of functional material are deposited onto a silicon wafer, patterned, and etched using a chemical process. Photolithography is the step in which patterns are imprinted on a photosensitive layer using light and is one of the most costly processing steps in the manufacturing of chips. As the transistor density increases the costs of lithography per pixel, here defined as the feature size squared, is a relevant economical figure of merit [5]. Fig. I.1 shows the time evolution of the cost per pixel for several generations of lithography machines from the Dutch lithography tool manufacturer ASML [6], sorted by the operating wavelength of the light source and the wafer size. The figure shows that the cost per pixel decreases at a similar, inverted rate as given by Moore's law. Shorter wavelengths enable smaller features to be patterned onto the photoresist layer, with the wavelength-dependent Rayleigh's resolving criterion being the limiting factor in obtaining smaller features. This criterion is directly related to the minimum reachable feature

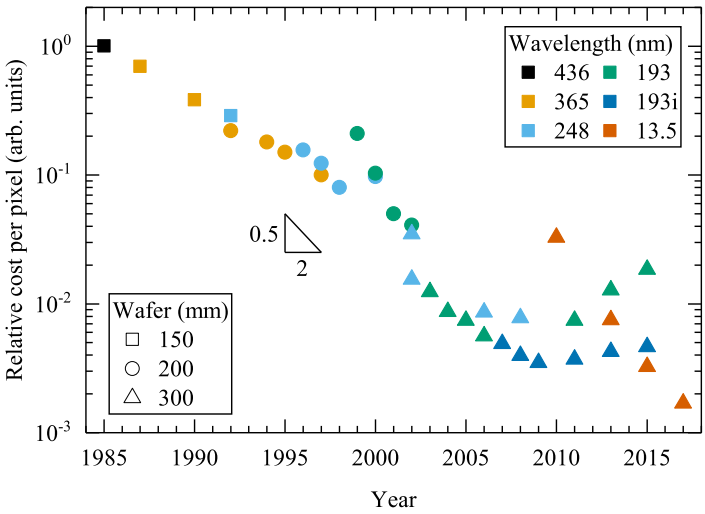

FIGURE I.1: Relative cost per pixel over time, sorted by different generations of photolithography machines produced by ASML as well as by wafer size. Here, a pixel is defined as the feature size squared. The generations are sorted by the wavelength of the light source used. Figure reproduced from data contained in Ref. [6].

size, commonly referred to as the critical dimension (CD):

$$\mathrm{CD} = k_1 \cdot \frac{\lambda}{\mathrm{NA}}, \tag{1}$$

with k_1 a constant related to the specifics of the lithography process, λ the wavelength of the light used, and NA the numerical aperture of the optical system. Each new generation of lithography machines typically employs shorter wavelengths in order to reach smaller feature sizes. Besides the wavelength, the numerical aperture can be increased to increase resolution. In the latest generation of lithography machines using a wavelength of 193 nm (indicated with 193i in Fig. I.1), a layer of water is included between the imaging optics and the wafer which increases the numerical aperture as the refractive index of water is higher than air. The relative cost of lithography is seen to increase after about 2010 as other methods, such as multiple patterning, are used to achieve further shrinking of feature sizes well below the lithography wavelength. Production costs are driven up due to the complexity and amount of processing steps needed for multiple patterning. To combat this cost increase, see Fig. I.1, and enable further shrinking of feature size, extreme ultraviolet lithography at a wavelength of 13.5 nm is currently being introduced in high-volume manufacturing.

The industrial development of a lithography tool based on extreme ultraviolet (EUV) light took several decades, mostly due to the complexity of the light source and the required mirrors [7, 8]. This industrial development went hand in hand with tremendous academic research efforts [8–24]. EUV light is absorbed by almost any medium, including air, setting the need for Bragg reflections in order to guide the light through the system. Multilayer mirrors act as Bragg reflectors, consisting of a stack of alternating layers of molybdenum and silicon. These mirrors have a record reflectivity of about 70%, but only within a narrow 2% bandwidth around 13.5 nm [25]. Light emitted in this range is commonly referred to as 'in-band' emission. State-of-the-art lithography machines use a droplet-based laser-produced plasma that brightly emits EUV light within the required wavelength range.

The laser-produced plasma is generated by illuminating a Sn droplet with a high-intensity laser pulse. For optimum laser-matter interaction, the target geometry can be changed into, e.g., a disk shape or a droplet mist, by using a so-called pre-pulse. The pre-pulse provides a kinetic push to the droplet, where fluid motion causes the geometrical change [26–29]. After the pre-pulse, a main pulse is applied to turn the target into a hot and dense plasma. The energy of the laser pulse is absorbed by means of inverse bremsstrahlung up to a laser-wavelength-dependent critical electron density [30]. The plasma electron density and temperature quickly increases to 10^{19}–10^{21} $e^{-}\mathrm{cm}^{-3}$ and around 10–100 eV, respectively, which enables efficient production of EUV light [31]. In industrial applications, pulsed CO_2 lasers with a wavelength of 10.6 μm are used because of their ability to operate at high intensities and high repetition rates. In our research we utilize a solid-state Nd:YAG laser with a wavelength of 1.064 μm. This change in drive laser wavelength has several consequences, one of which is that the pulse penetrates deeper into the plasma due to the higher critical density, and additionally opacity effects broaden the spectral feature at 13.5 nm [32–34]. There are however several benefits to using a solid-state laser, such as a smaller footprint and a better wall-plug efficiency [23]. The produced plasma is highly dependent on the laser wavelength, pulse length, spatial and temporal profiles, and other factors, such as the way in which the target is deformed by the pre-pulse. These factors influence the time-evolution of the plasma density and temperature and therefore the emitted spectrum. One can adjust all plasma parameters, but fully independent of all other plasma parameters is the underlying atomic structure of the highly charged ions that determines the transition wavelengths at which EUV radiation can be emitted. Understanding the atomic structure of highly charged Sn ions is therefore vital for improving the performance of such sources.

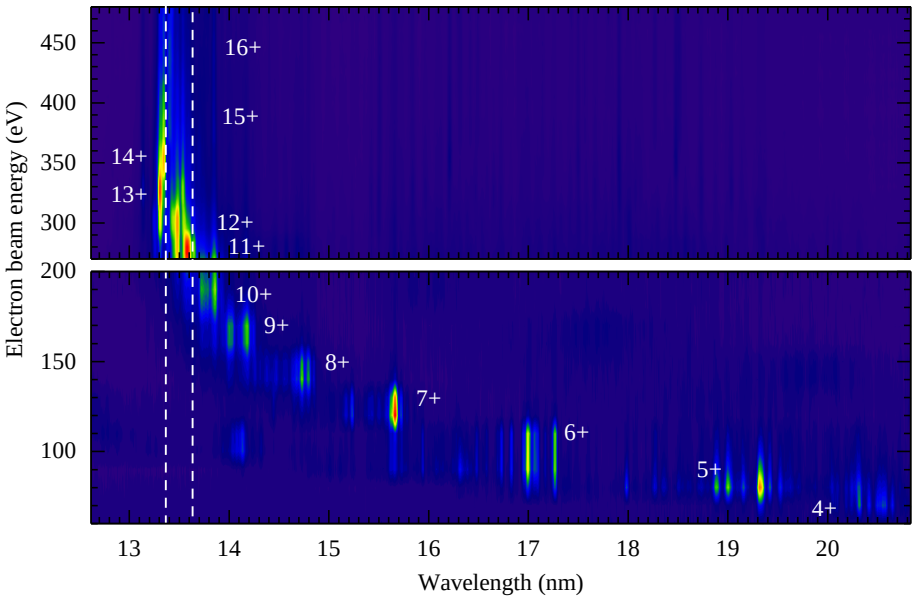

FIGURE I.2: Spectral intensity map of Sn ions constructed from measurements taken at an electron-beam ion trap facility at the Max-Planck-Institut für Kernphysik in Heidelberg, Germany. The upper graph shows emission from $4p$–$4d$ and $4d$–$4f$ transitions in Sn^{11+}–Sn^{16+} (see Chapter 1 for further details. The lower graph shows emission features from the same transition arrays in Sn^{4+}–Sn^{10+}. In Chapter 2 an investigation is performed on the emission features found in this spectral range for diagnostics of laser-produced plasma sources.

The atomic structure of Sn ions can be investigated by various means, such as: laser-produced plasmas [35], vacuum spark discharges [36], charge-exchange recombination spectroscopy [20, 21, 37], and electron-beam ion traps [38–40]. The light that is emitted in the vicinity of 13.5 nm manifests itself in so-called unresolved transition arrays (UTAs) originating from adjacent states. These transition arrays are unresolved due to the very high numbers of transitions possible in the open-$4d$ subshells of the ions considered. The transition arrays $4p^6 4d^m$–$4p^5 4d^{m+1}$ and $4p^6 4d^m$–$4p^6 4d^{m-1} 4f$ ($m = 6$–0) in Sn^{8+} to Sn^{14+} are known for their bright emission around 13.5 nm [8–19, 21, 24]. The overlap of these UTAs within a small band around 13.5 nm makes Sn an ideal atomic light source. Plasma diagnostics are however hampered by this atomic serendipity. Spectroscopic results presented in this thesis identify, for the first time, emission features from Sn^{15+} contributing to the 2% bandwidth around 13.5 nm. Recently it was found that emission from multiply-excited states also contribute to the in-band emission [35].

Diagnostics of the plasma by analyzing EUV light emission is made viable by observing so-called out-of-band radiation, outside of the 2% bandwidth around 13.5 nm. On the short wavelength side, between 7 and 12 nm, spectral features from different transition arrays belonging to the same ions as those which emit in-band radiation (Sn^{8+}–Sn^{14+}) are found [9, 15, 22, 23]. In the longer wavelength range, between 14 and 20 nm, spectral features belonging to Sn^{4+}–Sn^{11+} are readily identified. These features, obtained from charge-state-resolved spectroscopy in an electron-beam ion trap, are shown in Fig. I.2.

Spectral measurements in the optical regime are relatively straightforward to perform as light can be observed through a viewport in a vacuum system and standard optics can be used. Lowly ionized charge states, from neutral tin to Sn^{3+}, emit light in the optical range. Their optical lines emerge when the hot and dense plasma is in the cooling-down phase as the plasma expands and recombines. Space- and time-resolved measurements give insights into the temperature and density decrease of the expanding plasma [41–43]. Spectral line broadening and shifting from the Stark effect due to the interaction of ions with plasma electrons [44] enables the analysis of time- and space-dependent plasma parameters. Future experiments using optical spectroscopies, including measurements of the anisotropy of plasma expansion, could provide further diagnostic tools for industrially-relevant laser-produced plasmas.

Thesis outline and summary

This thesis provides an improved understanding of Sn spectroscopy through the identification of spectral lines in both lowly and highly charged tin ions, and applying this knowledge to investigate relevant Sn plasmas. Charge-state-resolved measurements on highly charged tin ions, which emit brightly in the EUV regime, are performed at the Max-Planck-Institut für Kernphysik in Heidelberg, Germany. Spectral measurements in the optical and EUV range on laser-produced plasmas have been performed in the EUV Plasma Processes group at the Advanced Research Center for Nanolithography in Amsterdam.

Chapter 1 presents measurements on highly charged tin ions as measured in the electron-beam ion trap (EBIT) facility in Heidelberg in a collaborative effort with spectroscopists from the Russian Academy of Sciences' Institute of Spectroscopy (ISAN) and theorists from the Australian University of New South Wales (UNSW). This chapter focuses on the EUV spectra of Sn^{13+}, Sn^{14+} and Sn^{15+} ions, typical measurement data for these ions of which is shown in the upper graph of Fig. I.2. A method is introduced to unravel convoluted spectra resulting from a charge state mixture as is present in the trap. The method is benchmarked by confirming transitions in Sn^{13+} and Sn^{14+} around 13.5 nm. Spectral identifications of Sn^{15+} are performed for the first time, highlighting strong emission features within the 2% bandwidth around 13.5 nm. Line identifications were made with guidance from the Cowan code and the collisional-radiative modeling capabilities of

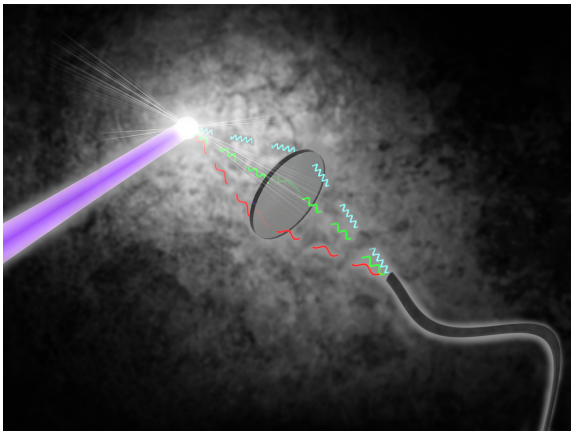

FIGURE I.3: Artistic illustration of the laser-produced plasma and experimental setup capturing optical light. A laser pulse, shown in violet, irradiates a Sn droplet. The resulting plasma emits optical light that is captured by a lens which images the light onto a fiber array connected to a spectrograph. Figure by Ricardo Struik.

the Flexible Atomic Code. Furthermore, state-of-the-art *ab initio* level structure calculations were performed using the configuration interaction many-body perturbation code AMBiT.

EUV spectra from highly charged tin ions are further investigated in Chapter 2, in which the EBIT measurements are compared to data obtained using the laser-produced plasma setup at ARCNL. Spectra obtained in this setup are analyzed for various laser energies and for two different target geometries: a planar solid target and a droplet target. The spectrum with the most intense spectral feature around 13.5 nm shows that spectral features overlap at this wavelength, thus complicating plasma diagnostics. Out-of-band spectral features are therefore studied in order to help understand the in-band EUV spectrum. This goal of this chapter is to analyze the spectra of charge states Sn^{5+} to Sn^{10+}. Measurements on these ions obtained in the EBIT, see Fig. I.2, are used to describe the various spectral features obtained. The spectral features are typically UTAs associated with the superposition of many thousands of spectral lines in this range, which complicates line identifications. In collaboration with ISAN we have identified numerous spectral features in the EBIT spectra, several of which have not been reported previously. Using the obtained data we identify features observed in the LPP spectra and demonstrate the potential of using long-wavelength out-of-band emission to individually probe the charge states contributing to the spectra relevant for nanolithography.

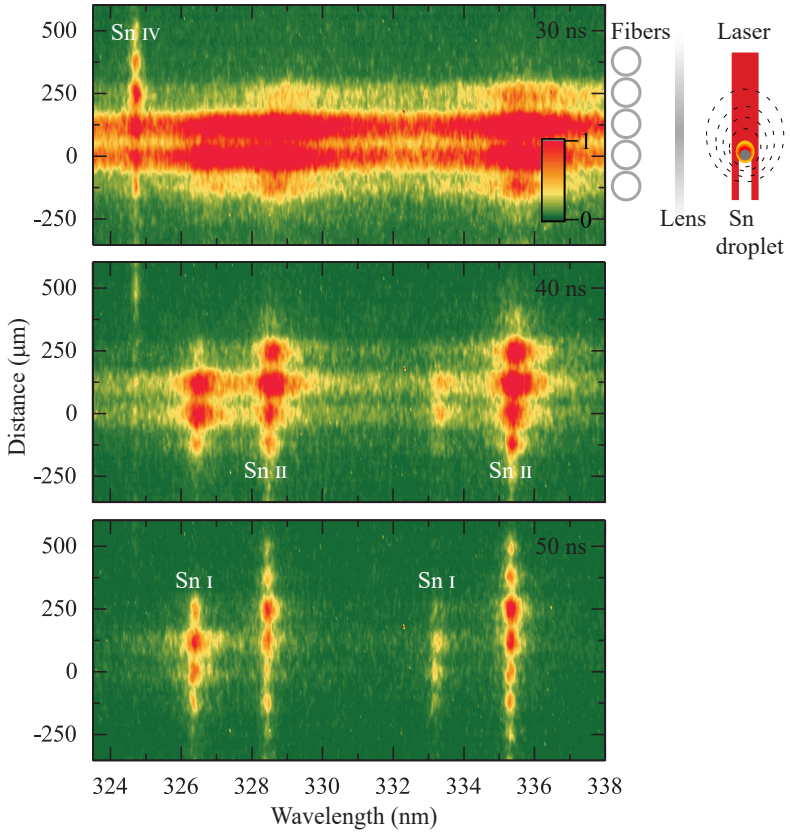

FIGURE I.4: Time- and space-resolved optical spectroscopy of a laser-produced Sn plasma. An impression of the optical system is displayed on the right-hand side of the top panel (see Chapter 4 for more information). Light captured by seven adjacent fibers are shown in each panel. Line broadening and shifting is observed for lines belonging to several Sn charge states indicated in the figure. The time indicated in the figures is with respect to the first time-frame in which emission from a 15 ns-long Nd:YAG laser pulse hitting the droplet is observed.

A study on the ultraviolet and optical spectra from a droplet-based laser-produced plasma is presented in Chapter 3. The analysis of the spectra, obtained at ARCNL, is a result of a collaborative effort with spectroscopists from ISAN and theorists from UNSW and the University of Groningen. An artistic impression of the experimental setup is given in Fig. I.3. Here, a tin microdroplet is illuminated with a high-intensity laser pulse driving the plasma. The radiation from the droplet is captured by a lens and focused onto a fiber array. The fiber array is connected to a spectrograph in order to capture the ultraviolet and optical spectrum of the light emitted from the plasma. In this spectral range, lines from neutral tin (Sn I) to Sn^{4+} (Sn V) were found, whereof a major fraction were previously unidentified. We focus on spectral features of Sn^{3+}, where we identify 33 new lines with guidance from Cowan code calculations and quantum defect scaling. Using the newly identified lines, 13 previously unknown level energies are determined. The level structure is found to be in good agreement with relativistic Fock-space coupled cluster (FSCC) calculations, but these calculations fail to reproduce the anomalous behavior of the $5d\ ^2D$ and $nf\ ^2F$ terms. By combining the strengths of the FSCC, Cowan code, and configuration interaction many-body perturbation theory calculations, this behavior is shown to arise from interactions with doubly-excited configurations. The newly-found Sn IV lines advance plasma diagnostic opportunities in the optical range.

The investigation of the diagnostic potential of optical spectroscopy is continued in Chapter 4, where we focus on unveiling the afterglow of the laser-produced plasma. The experimental setup is modified to enable time- and space-resolved spectroscopy of Sn plasmas. The laser-produced plasma is imaged onto a fiber array that is connected to an imaging spectrometer. A fast-gated camera is used in order to achieve a 10 ns shutter time. Several frames obtained at various time steps after the laser impact are displayed in Fig. I.4. An impression of the experimental setup is displayed on the right-hand side of the top panel. Several Sn charge states, as indicated in the figure, emit brightly in this wavelength range. Severely broadened and shifted lines are observed for transitions in Sn I to Sn IV. The Stark effect is found to be responsible for these observed features. Stark shift-to-width ratios serve as the basis for unambiguous experimental tests of theory predictions, which are found to be in poor agreement with each other for the studied cases. Temperature estimates are obtained by a Saha-Boltzmann analysis of line intensities of Sn I and Sn II. Time-dependent electron densities are obtained from Sn I to Sn IV line shapes by comparison against literature values. Further studies using time- and space-resolved spectroscopy, such as on the anisotropy of the plasma, can lead to a better understanding of the local environment of droplet-based plasma sources of EUV light.

In summary, charge-state-resolved spectroscopy studies enable diagnosing laser-produced tin plasmas and are indispensable for understanding the atomic origins of EUV light in such plasmas. Such studies, in particular those performed in the easily accessible optical regime, may lead to novel monitoring and optimization methods of industrial plasma sources of EUV light.

1

EUV spectroscopy of highly charged Sn^{13+}–Sn^{15+} ions in an electron-beam ion trap

J. Scheers, C. Shah, A. Ryabtsev, H. Bekker, F. Torretti, J. Sheil, D. A. Czapski, J. C. Berengut, W. Ubachs, J. R. Crespo López-Urrutia, R. Hoekstra, and O. O. Versolato

Physical Review A **101**, 062511 (2020)

Extreme ultraviolet (EUV) spectra of Sn^{13+}–Sn^{15+} ions have been measured in an electron-beam ion trap (EBIT). A matrix inversion method is employed to unravel convoluted spectra from a mixture of charge states typically present in an EBIT. The method is benchmarked against the spectral features of resonance transitions in Sn^{13+} and Sn^{14+} ions. Three new EUV lines in Sn^{14+} confirm its previously established level structure. This ion is relevant for EUV nanolithography plasma but no detailed experimental data currently exist. We used the Cowan code for first line identifications and assignments in Sn^{15+}. The collisional-radiative modeling capabilities of the Flexible Atomic Code were used to include line intensities in the identification process. Using the 20 lines identified, we have established 17 level energies of the $4p^4 4d$ configuration as well as the fine-structure splitting of the $4p^5$ ground-state configuration. Moreover, we provide state-of-the-art *ab initio* level structure calculations of Sn^{15+} using the configuration-interaction many-body perturbation code AMBiT. We find that the here-dominant emission features from the Sn^{15+} ion lie in the narrow 2% bandwidth around 13.5 nm that is relevant for plasma light sources for state-of-the-art nanolithography.

1.1 Introduction

Extreme ultraviolet (EUV) light emission near 13.5 nm wavelength from highly charged tin ions, primarily from $4p$–$4d$ and $4d$–$4f$ transitions in Sn^{8+}–Sn^{14+}, is the source of light for state-of-the-art nanolithography [12–14, 24, 35]. Accurate knowledge of the open $4d$-subshell atomic structure of these ions provides insight for further optimization of EUV light emission of industrial laser-driven plasma sources. The electronic structure of the involved tin ions is extremely complicated, in part due to the existence of strong configuration interaction effects. Spectroscopic accuracy remains inaccessible to even the most advanced atomic codes. Given their importance, the spectra of these charge states have been widely investigated [16–21, 37, 45, 46]. Recently, however, evidence was found calling for a revision of earlier identifications of transitions in Sn^{8+}–Sn^{14+} ions [38, 39]. Furthermore, no experimental atomic structure data are available on the neighboring charge state Sn^{15+}, with its open $4p$-subshell $4p^5$ ground-state configuration. Emission from tin ions in charge state 15+ is however readily observed from the relatively weak $4p$–$5s$ transitions near 7 nm in EUV-generating laser-produced tin plasmas [22, 23]. Understanding the contribution of the stronger $4p$–$4d$ transitions of Sn^{15+} (as compared to its $4p$–$5s$ transitions) to the industrially relevant emission feature at 13.5 nm should therefore be particularly relevant for simulations of such plasmas. New experimental tin data are thus required.

Experimental investigations are hampered by the fact that plasmas, including plasma in electron-beam ion traps (EBITs) [47–52], that are typically required to produce ions in intermediate charge states, contain a mixture of ions of different charge states with overlapping spectral features. Charge-state-resolved spectra can be obtained using suitable subtractions of spectra acquired under various plasma conditions [53–56] or by employing genetic algorithms [57]. In this work, we employ a matrix inversion method to obtain charge-state-resolved spectra using matrix inversion techniques on convoluted, mixed-charge-state EUV spectra experimentally obtained from an electron-beam ion trap.

We focus here on the EUV spectra of Sn^{13+}–Sn^{15+}. Their strongest line features are particularly closely spaced and offer a rather tractable atomic structure with a relatively limited number of strong transitions. First, as a benchmark, we use the matrix inversion method to reevaluate the $4p^6 4d$–$(4p^5 4d^2 + 4p^6 4f + 4p^6 5p)$ type EUV transitions in Sn^{13+}. Subsequently, we apply the method to obtain unique information on the atomic structure of the excited configurations $4p^5 4d$ in Sn^{14+} and $4p^4 4d$ in Sn^{15+}. Line identifications in Sn^{15+} are enabled using the semiempirical Cowan code [58], which allows for adjusting scaling factors applied to radial integrals in order to fit observed spectra using initial preliminary assignments. Identifications of lines in both Sn^{14+} and Sn^{15+} are further strengthened by line intensity calculations using the collisional-radiative modeling capabilities of the Flexible Atomic Code (FAC) [59]. We compare our obtained level energies with calculations performed with the Fock-space coupled cluster (FSCC) approach for

Sn^{14+} [39] and General-purpose Relativistic Atomic Structure Package (GRASP) calculations for Sn^{15+} [60]. In this work, we also provide state-of-the-art calculations of Sn^{15+} using the configuration-interaction many-body perturbation code AMBiT [61]. Its performance is gauged against published calculations as well as experimental observations.

1.2 Experiment

We performed spectroscopic measurements in the EUV region on tin ions over the range of charge states Sn^{9+}–Sn^{20+} at the FLASH-EBIT facility [62] at the Max Planck Institute for Nuclear Physics in Heidelberg, Germany. FLASH-EBIT employs a pair of superconducting Helmholtz coils to generate a 6-T magnetic field in order to guide and compress the electron beam, with a density of approximately $10^{11}\,e^-\,\mathrm{cm}^{-3}$ (see below), down to a diameter of about 50 μm. A molecular beam of tetra-i-propyltin ($C_{12}H_{18}Sn$) was injected into the trap through a two-stage differential pumping system. The tetra-i-propyltin molecules are dissociated while crossing the electron beam. The electron beam rapidly ionizes and traps the Sn ions, while the lighter elements leave the trap. By adjusting the acceleration voltage, the electron-beam energy can be set to achieve preferential production of a specific charge state. Subsequently, the electron beam collisionally populates excited states from which the emission is collected.

Extreme ultraviolet radiation emitted by the highly charged ions in the trap is diffracted by a 1 200-lines/mm flat-field, grazing-incidence grating [63] and recorded on a Peltier-cooled charge-coupled device (CCD) sensor. The wavelength range covered by the spectrometer encompasses the 13.5 nm region most relevant to nanolithographic applications. A wavelength range from 12.6–20.8 nm is captured in the observation of light diffraction in first order of the grating, with lines having a full width at half maximum (FWHM) of about 0.03 nm. To achieve the best possible resolution, the camera position was alternatively set such that the 12–17 nm spectral range can be observed in second order where typically a FWHM resolution of about 0.02 nm was achieved. The spectra are corrected for small optical aberrations and background signal before projection onto the dispersive axis of the full CCD image. Corrections for camera sensitivity and grating efficiency are subsequently applied. Wavelength calibration of the spectrometer is performed by injecting oxygen into the trap and observing a set of known O^{2+}–O^{4+} lines [64]. The calibration uncertainty of 0.003 nm (one standard deviation of the residuals) is the dominant contributor to the overall uncertainty budget for determining line centers. Calibration runs were performed on several days during the experimental campaign to combat any potential significant drift. Line positions found in the first- and second-order-diffraction measurements (see below), performed on different days and under different EBIT settings, agree well within the uncertainty estimates.

Two measurement series are performed, utilizing either the first- or second-order diffraction of the grating. Fluorescence emission from Sn^{12+}–Sn^{20+} is observed by increasing the electron-beam energy in 5-eV steps from 320 to 695 eV while keeping the electron-beam current constant at 20 mA. The light captured on the CCD is integrated for 480 s per electron-beam energy step. In the second-order measurement series, EUV emission from tin ions in charge states 9+ up to 18+ is observed by increasing the energy of the electron beam in 10-eV steps from 210 to 560 eV. The electron-beam current in the second-order measurement series was kept steady at 10 mA. In each of the 36 steps of the electron-beam energy, an EUV spectrum was accumulated with a camera integration time of 1 800 s to ensure a sufficient signal-to-noise ratio. In the following, results from the second-order measurement series are described in detail. First-order measurement results are employed for further line identifications in the wavelength range not captured in second order.

1.3 General features of the EUV emission maps

A 2D map (wavelength, electron-beam energy) of EUV light intensities is presented in Fig. 1.1. An initial charge-state identification was performed by locating known lines in the 2D map. The very bright emission feature near 13.34 nm is the resonant $4p^6\ {}^1S_0$–$4p^5 4d\ {}^1P_1$ transition in Sn^{14+} [19, 65]. At slightly shorter wavelength, lines from Sn^{13+} can be identified [16, 19, 66]. From Fig. 1.1, it can be seen that the strong emission manifolds belonging to $4p^6 4d^m$–$(4p^5 4d^{m+1}+4p^6 4d^{m-1} 4f)$ transitions in Sn^{9+} ($m = 5$) to Sn^{13+} ($m = 1$) shift toward shorter wavelength with increasing charge state. EUV emission from these open $4d$-subshell ions have been extensively studied in the literature; see, e.g., Refs. [16–19]. Intriguingly, after emptying the $4d$ subshell at 14-fold charged tin, the strongest transitions for tin ions in charge state 14+ and higher shift back to longer wavelengths.

The emergence and submergence of spectral features at certain electron-beam energies can be understood from considerations of the ionization potentials of tin ions. This procedure allows for the assessment of ranges of electron-beam energies in which tin ions in a specific charge state are the dominant contributors to the EUV spectra. In each of the charge-state bands, the measured spectrum with the highest fluorescence is chosen as the representative spectrum for that charge state. In Fig. 1.1, the overlaid line spectra (white solid lines) are the corresponding spectra for Sn^{13+}, Sn^{14+}, and Sn^{15+}. From the figure it is clear that representative spectra are not free of spectral admixtures from Sn ions in adjacent charge states. Fluorescence curves are a way to assess potential admixtures of different charge states. A fluorescence curve represents the intensity of a specific line as a function of electron-beam energy. We project vertical regions of interest from the data as shown in Fig. 1.1. Several lines per charge state are identified in order to construct a

generic fluorescence curve. We choose in the spectral map lines that are preferably isolated, mostly outside of dense spectral regions, and compare them critically. It is found that commonly the observed energy dependencies of the line strengths are very similar for all lines associated with a particular charge state. Lines with expected blends of other charge states, showing miscellaneous energy-dependent behavior, were excluded or corrected for contributions from line blending. Individual fluorescence curves are normalized and subsequently averaged such that a generic fluorescence curve per charge is obtained.

The normalized fluorescence curves of Sn^{9+} to Sn^{18+} ions are shown in Fig. 1.2. In general, the fluorescence from a certain ionic state q increases rapidly once the electron-beam energy exceeds the ionization potential of the previous charge state $q-1$. Once the ionization potential of the charge state q is reached, the fluorescent curve belonging to q is observed to decline. The electron beam produces a strong space charge region in the trap, lowering the actual electron-beam energy in the interaction region in the center of the trap by a current-dependent value [39, 67]. This effect however is partially compensated by the trapped positive ions. The net result is typically a lowering of the electron-beam energy by a few eV per mA current [39, 67]. Space charge effects have a negligible influence on the onset of the fluorescence curves (cf. Fig 1.2). The fluorescence curve of Sn^{15+} is different from the other charge states as it shows two peaks instead of one. This can be explained by early production of Sn^{15+} out of metastable Sn^{14+} levels, similar to the case presented in Ref. [39]. Although weaker, a similarly early onset is also visible for Sn^{16+}. The relevance of early ionization via metastable levels as intermediate steps depends on a delicate balance between the lifetimes of said metastable levels and the electron-beam density [68]. These features are well captured by our method below and therefore do not negatively impact it.

The fluorescence curves indicate that a tin spectrum, taken at any single electron-beam energy, contains emission features from a mixture of tin charge states. In the following, we will employ a method to retrieve charge-state-resolved spectra.

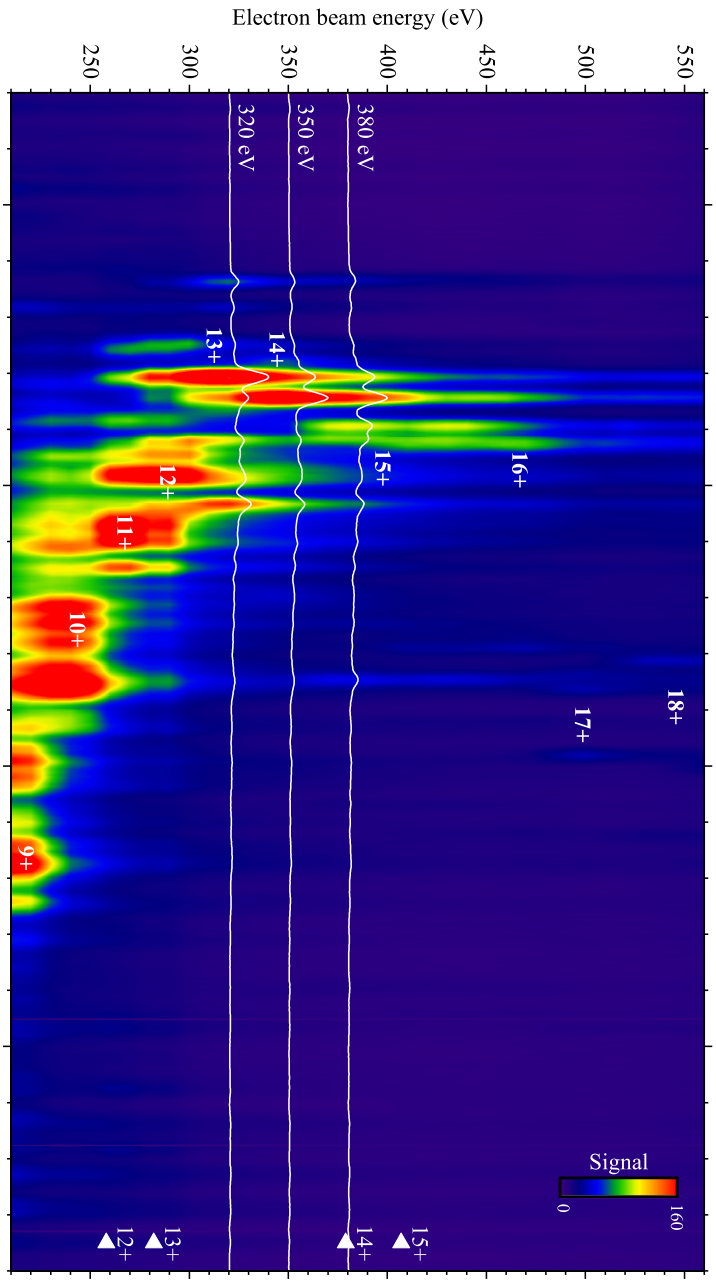

FIGURE 1.1: (Caption on the following page).

FIGURE 1.1: (Figure on the previous page) Spectral intensity map of Sn ions constructed from measurements at the FLASH-EBIT, obtained in second-order diffraction from a 1200-lines/mm grating. The 2D map is produced by interpolating between discrete spectra that are taken at 10 eV electron-beam energy steps. The main features belonging to Sn^{9+} to Sn^{18+} ions are labeled. The overlaid spectra (white solid lines) at 320, 350, and 380 eV show representative EUV spectra of Sn^{13+}, Sn^{14+}, and Sn^{15+} ions, respectively, at the peak of their fluorescence curves. The white triangles denote the location of the ionization potential belonging to Sn^{q+}.

1.4 Matrix inversion

For unraveling blended spectra, such as those of Sn^{q+} ions, we employ a matrix inversion method for charge-state-resolved EBIT spectral reconstruction. The principle of the method is analogous to that of the subtraction scheme introduced by Lepson *et al.* [55]. In the matrix inversion method it is hypothesized that each row in the 2D map (wavelength, electron-beam energy) of light intensities shown in Fig. 1.1 in fact represents a linear combination of unique spectra per charge state weighted by their respective fluorescence curve. These spectral maps can thus be represented by a matrix $\boldsymbol{E}$ of dimension $m \times w$, where m is the number of spectral scans (electron-beam energy steps) and w is the number of wavelength bins. The matrix elements contain spectral intensities directly obtained from measurements. Fluorescence curves, such as the ones shown in Fig. 1.2, span a fluorescence matrix $\boldsymbol{F}$ of dimension $m \times c$, where c is the number of distinct charge states in the EBIT spectrum. This overdetermined linear system can be described as

$$\boldsymbol{F}\boldsymbol{S} = \boldsymbol{E}, \tag{1.1}$$

with $\boldsymbol{S}$ containing the charge-state-resolved spectra to be determined. The least-squares solution for this problem is found by utilizing the generalized inverse method [69]. The solution yields the minimum norm of the system and is found by first multiplying Eq. (1.1) with the transpose of the fluorescence matrix $\boldsymbol{F}$:

$$\boldsymbol{F}^T\boldsymbol{F}\boldsymbol{S} = \boldsymbol{F}^T\boldsymbol{E}. \tag{1.2}$$

The matrix product $\boldsymbol{F}^T\boldsymbol{F}$ is a square matrix and allows for the determination of an inverse, in the case of full column rank of $\boldsymbol{F}$ (i.e., when each column is linearly independent). The present experimental data fulfill this requirement. Subsequently, when Eq. (1.2) is multiplied by this inverse, the solution of matrix $\boldsymbol{S}$ is given by

$$\boldsymbol{S} = (\boldsymbol{F}^T\boldsymbol{F})^{-1}\boldsymbol{F}^T\boldsymbol{E} \tag{1.3}$$

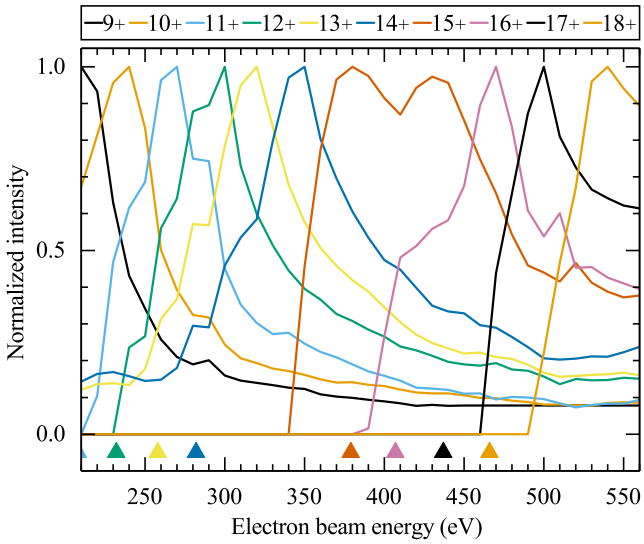

FIGURE 1.2: Normalized intensity of spectral lines belonging to Sn^{q+} (q = 9–18) along the variation of the set electron-beam energy. The triangles mark the threshold for producing the Sn^{q+} ion at the ionization potential of charge state $q-1$ [71].

This solution is also referred to as the *left inverse* of this linear system. The resulting matrix $\boldsymbol{S}$ has dimensions $c \times w$.

The non-negative matrix factorization (NNMF) method [70] provides an alternative route for obtaining matrices $\boldsymbol{F}$ and $\boldsymbol{S}$. NNMF enables obtaining the (positive-definite) matrices without any prior knowledge of the system, such as the fluorescence curves. Test fits to our EBIT spectra with the NNMF method were made for comparison with the spectra obtained from matrix inversion. For Sn^{13+}, the NNMF spectrum looked very similar; however, a few spurious spectral features emerged when retrieving Sn^{14+} and Sn^{15+} spectra. Therefore, we do not consider NNMF in the following and accept a few small spurious features in the spectra reconstructed through matrix inversion, cf. Fig. 1.3, stemming from imperfections in the fluorescence curves. However, such artifacts can easily be identified and excluded.

1.5 Results and line identifications

Charge-state-resolved spectra reconstructed by means of the matrix inversion method are presented in Fig. 1.3. The direct EBIT spectra at electron-beam energies at which Sn charge states Sn^{13+}, Sn^{14+}, and Sn^{15+} show maximum fluorescence are included in Fig. 1.3. From comparison of the results of the matrix inversion with the untreated direct data, it is evident that there exists large admixtures of charge states in the untreated spectra. A detailed analysis of the line identifications of Sn^{13+} to Sn^{15+} ions is presented, using the case of Sn^{13+} ions as a reference as its atomic structure is well known [16, 19, 66]. An analysis per charge state is laid out after a short introduction to the various atomic structure codes used to perform the line identifications.

The Hartree-Fock method with relativistic corrections incorporated in the RCN-RCN2-RCG chain of the Cowan code [58, 72] is used for the calculation of wavelengths of $4p^6$–$4p^5 4d$ and $4p^5$–$4p^4 4d$ transitions in Sn^{14+} and Sn^{15+} ions, respectively. In addition to the wavelength of a transition, the line intensity is also an important identification tool. For experiments on EBITs, the electron beam may strongly affect specific line intensities, making them deviate strongly from calculated gA values (multiplicity times the Einstein coefficient); see, e.g., Ref. [67]. Inclusion of such effects requires collisional-radiative modeling (CRm). We used the CRm capabilities available in FAC [59]. CRm calculates the relative population of levels within the atomic structure. The "line emissivity," presented as luminosity in photons/s, is obtained from the multiplication of the relative population times the Einstein A coefficient as calculated by FAC [59].

FAC calculations here tend to overestimate level energies in comparison with experiment. Therefore, we have shifted level energies calculated by FAC to match the level energies obtained from the Cowan code. Following the conclusions in Ref. [67], in which electron-beam densities in FLASH-EBIT were investigated under similar conditions, we used a $10^{11}\, e^-\,\mathrm{cm}^{-3}$ electron-beam density in our CRm calculations. This density is shown to accurately predict the relative intensities of magnetic-dipole to electric-dipole transitions in Sn^{14+}. Slight differences in the choice of density and possible polarization-induced emission anisotropies (such as observed, e.g., in recombination measurements in Refs. [73, 74]) were investigated and are not expected to affect the final identifications. Cowan and FAC-CRm details specific to Sn^{14+} and Sn^{15+} ions are discussed in the following subsections. The resulting spectra are individually normalized per charge state. Area-under-the-curve line intensities are normalized to the strongest line for each charge state in order to allow for a straightforward comparison with the normalized line spectra.

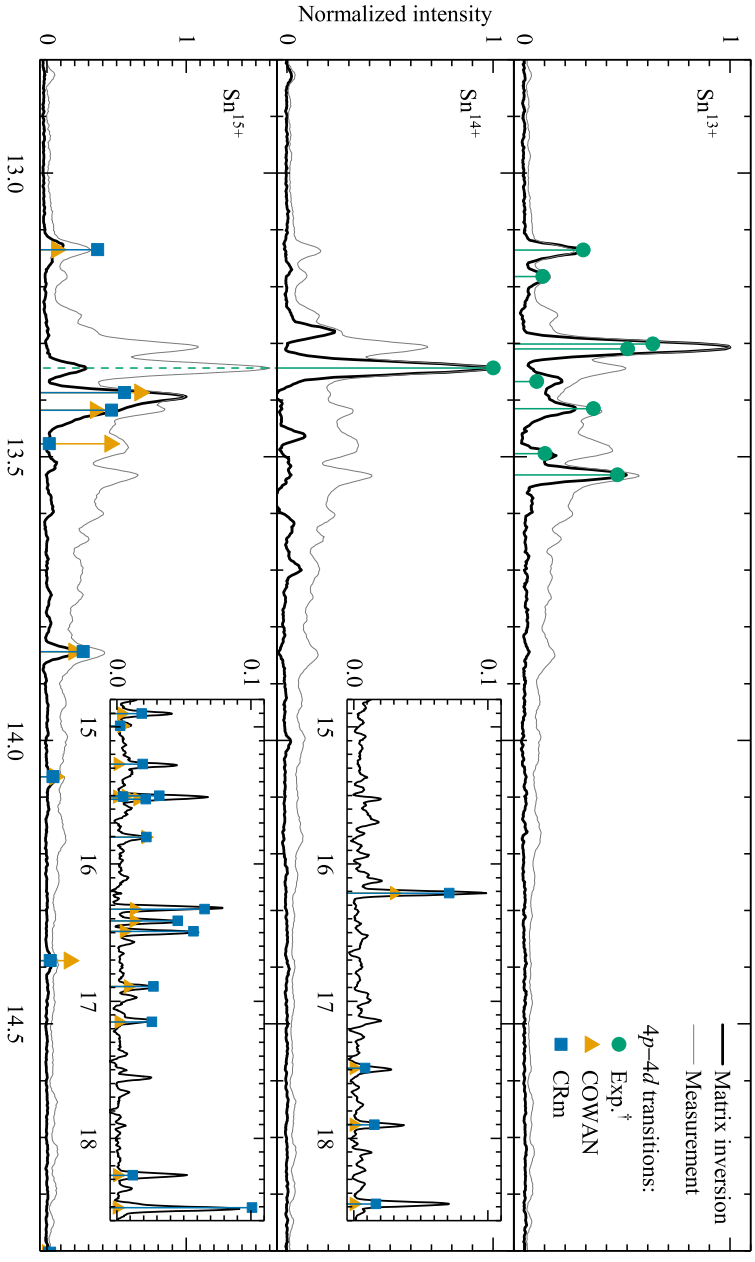

FIGURE 1.3: (Caption on the following page)

FIGURE 1.3: (Figure on the previous page) Charge-state-resolved spectra for Sn charge states Sn^{13+}–Sn^{15+}. Spectra determined with the matrix inversion method (described in Sec. 1.4) are shown in black. The untreated EBIT spectra are represented by thin gray lines and are identical to the line-out projections in Fig. 1.1, here normalized to the strongest line feature associated with the respective charge state. †The green circular data points represent normalized *gA* factors for transitions previously identified in the literature [16, 19], $4p^6 4d$–$4p^5 4d^2$ transitions in Sn^{13+} and $4p^6$–$4p^5 4d$ transitions in Sn^{14+}. A vertical dashed line at 13.34 nm indicates an artifact; see Sec. 1.5.3. The insets in the center and bottom panels show part of the Sn^{14+} and Sn^{15+} spectra measured in the first-order measurement series. Yellow triangles indicate normalized *gA* factors resulting from Cowan code calculations. Normalized emissivity values, calculated by FAC's CRm module, are shown as blue squares.

1.5.1 Spectrum of Sn^{13+}

The EUV spectrum of Sn^{13+} has been studied previously in plasma discharge sources [16, 19, 66]. Strong lines between 13.1 and 13.6 nm have been identified as belonging to resonant transitions between levels of the first excited configuration $4p^5 4d^2$ and the $4p^6 4d$ ground configuration. The top panel of Fig. 1.3 shows our untreated (gray line) and matrix-inverted (black) EUV spectrum of Sn^{13+}. The matrix-inverted result is in excellent agreement with previous identifications, as shown in Fig. 1.3 and in Table 1.1. Comparing the matrix-inverted and untreated spectra of Sn^{13+} makes clear that spectral analysis solely based on a measurement taken at peak fluorescence for this ion would not provide sufficient detail. This demonstrates and validates the applicability of the method to the measured EBIT spectra. One of the four possible transitions within the ^2D–$4d^2$ $(^3F)^2D$ multiplet is not observed (cf. Table 1.1). The transition $^2D_{3/2}$–$(^3F)^2D_{5/2}$ may be expected at a wavelength of 13.08 nm. However, according to the Cowan code calculations, it has a too low *gA* value to be detected. Also, the $^2D_{5/2}$–$4d^2$ $(^1G)^2F_{5/2}$ transition predicted at 13.78 nm is not detected as may be expected because this $\Delta J = 0$ transition is further suppressed by configuration interaction.

1.5.2 Spectrum of Sn^{14+}

The EUV spectrum of Sn^{14+} consists of a few resonance lines. Two lines at approximately 13.34 and 16.21 nm have been observed previously [16, 19, 65], and are observed in our spectra as well. Additionally, three new lines in the 17–19 nm range are identified. Line positions and assignments of these five Sn^{14+} transitions are presented in Table 1.2. The assigned transitions stem from levels 2, 3, and 6 (see Table 1.3), which are mainly of character $^3P_1$, $^3P_2$, and $^1D_2$, respectively. Excellent agreement is obtained with the fine structure determined in Ref. [39], where the fine structure of the $4p^5 4d$ configuration was studied by the observation of magnetic dipole transitions in the optical regime. The level energy differences between levels 2–3 and 2–6 have been measured directly. They form Ritz combinations with transitions found in the EUV. Two of the newly assigned EUV

TABLE 1.1: Comparison of observed wavelengths of EUV lines in Sn^{13+} with literature values. Transitions stem from strongly mixed upper levels associated with the $4p^5 4d^2$ configuration (denoted by $4d^2$), $4p^6 4f$, and $4p^6 5p$ decaying to the ground configuration $4p^6 4d\ ^2D_J$. Wave-function compositions of these mixed levels can be found in Ref. [19]; only the leading term is shown. Wavelength and normalized intensities (Int.) obtained in this work originate from fits to the spectrum. Superscripts on wavelengths indicate blended (bl) lines.

	Wavelength (nm)		
Transition	Literature	Experiment	Int.
$^2D_{3/2}$–$5p\ ^2P_{3/2}$	12.1339 [16]		
$^2D_{5/2}$–$5p\ ^2P_{3/2}$	12.3316 [16]	12.334	41
$^2D_{3/2}$–$5p\ ^2P_{1/2}$	12.5065 [16]	12.519	51
$^2D_{3/2}$–$4d^2\ (^3F)^2D_{3/2}$	13.1358 [16]	13.137	389
	13.1361 [66]		
$^2D_{3/2}$–$4d^2\ (^3P)^2P_{3/2}$	13.1821 [19]	13.184	116
$^2D_{5/2}$–$4d^2\ (^1G)^2F_{7/2}$	13.3014 [16]	13.301[bl]	586
	13.3020 [66]		
$^2D_{5/2}$–$4d^2\ (^3F)^2D_{5/2}$	13.3102 [16]	13.304[bl]	1000
	13.3105 [66]		
$^2D_{5/2}$–$4d^2\ (^3F)^2D_{3/2}$	13.3675 [16]	13.367	275
$^2D_{5/2}$–$4d^2\ (^3P)^2P_{3/2}$	13.4154 [19]	13.415	441
$^2D_{3/2}$–$4d^2\ (^3P)^2P_{1/2}$	13.4943 [19][a]	13.498	170
$^2D_{3/2}$–$4d^2\ (^1G)^2F_{5/2}$[b]	13.5318 [16]	13.532	711
	13.5315 [66]		

[a] Tentative assignments from Ref. [19].
[b] The dominant term is indicated to be $4f\ ^2F_{5/2}$ [19].

lines in the 17–19 nm range (originating from upper levels 3 and 6) have very small gA values (on the order of 1000 s^{-1}) as is to be expected for $\Delta J = 2$ transitions. Notwithstanding that, these lines are observed in the EBIT spectrum because of the strongly enhanced population of their upper levels as indicated by our CRm calculations.

Fock-space coupled cluster (FSCC) predictions for the structure of Sn^{14+} [39], shown in Table 1.3, are in excellent agreement with our identifications with a root-mean-square difference with experiment below 0.1%.

Through a semiempirical adjusting of scaling factors, the Cowan code enables evaluating level energies of Sn^{14+} to a high accuracy. The level energies of the $4s^2 4p^5 4d$ configuration of Sn^{14+} are optimized using configuration interaction between the following configurations: $4s^2 4p^5 5d$, $4s^2 4p^5 5s$, $4s 4p^5 4d^2$, $4s 4p^6 4f$, $4s^2 4p^3 4d^3$, $4s^2 4p^4 4d 4f$, $4s^2 4p^5 5g$, $4p^5 4d^3$, $4p^6 4d 4f$, and $4s 4p^5 4f^2$. The final Cowan scaling factors are presented in Table 1.4, with level energies provided in Table 1.3.

There are several other lines observed in the vicinity of the main peak at 13.34 nm in the Sn^{14+} spectrum. These transitions do not belong to the $4p$–$4d$ transition array.

In particular, the line at 13.28 nm stands out. These additional lines may originate from transitions into the excited $4p^5 4d$ configuration out of the strongly mixing $4p^5 4f$ and $4p^4 4d^2$ configurations. There exist many transitions connecting these excited configurations, which prohibits a unique assignment since both expected position and line strength are strongly affected by the effects of configuration interaction. A qualitative study of the emission intensities stemming from FAC-CRm calculations tentatively suggests that the two stronger lines observed at 13.28 and 13.46 nm may be due to, respectively, $J = 4$–5 and $J = 3$–4 transitions in the $4p^5 4d$–$4p^4 4d^2$ manifold. Similar transitions in the same wavelength range have been observed in charge-exchange spectroscopy studies of Sn^{15+} ions colliding with He [75].

The influence of the redistribution of level populations by the EBIT beam on the observed line intensity has also been observed in transitions between fine-structure levels of the $4p^5 4d$ configuration [39]. In Ref. [39], the strongest line at 297.7 nm ($^3P_2$–$^3D_3$, intensity of 211) has a gA factor of 981, while a neighboring line at 302.9 nm ($^3D_1$–$^3D_2$) with a three times higher gA factor of 2597, is detected with a more than tenfold lower intensity of 15. CRm calculations show that population of the $^3D_3$ level is strongly preferred. This leads to an inverted emissivity ratio of almost 10 to 1 instead of 1 to 10 for these transitions, in agreement with the measurements.

1.5.3 Spectrum of Sn^{15+}

Sn^{15+}, with a bromine-like ground-state configuration ($[Ar]3d^{10}4s^2 4p^5$), has received little attention thus far. Its EUV spectrum in the wavelength range near 13.5 nm consists of one strong emission feature along with several weaker lines (cf. Fig. 1.3). These features are expected to stem from $4p^5$–$4p^4 4d$ transitions. The peak at 13.344 nm belongs to Sn^{14+} and is the strongest line in the EBIT measurements. Its contribution is seen to be incompletely removed by the method. It is the only such artifact apparent in the current spectra. The untreated spectra taken at peak fluorescence for Sn^{14+}–Sn^{16+} are shown in the inset in the bottom panel of Fig. 1.3. This inset highlights the difficulty of identifying the (unresolved) lines belonging to Sn^{15+} from observing line intensity changes in the untreated spectra alone. The matrix inversion method is shown to resolve the line features of the Sn^{15+} ion.

To enable the identification of Sn^{15+} lines (see Table 1.2), the Hartree-Fock method with relativistic corrections (HFR) incorporated in the RCN-RCN2-RCG chain of the Cowan code was used for *ab initio* calculations of wavelengths arising from $4s^2 4p^5$–$4s^2 4p^4 4d$ transitions. The following set of odd-symmetry configurations is considered: $4s4p^5 4d$, $4s4p^4 4d4f$, $4s^2 4p^4 4f$, $4s^2 4p^3 4d^2$, $4s^2 4p^3 4f^2$, $4p^5 4d^2$, $4p^5 4f^2$, and $4p^6 4f$. For the even symmetry, the excited $4s^2 4p^4 4d$, $4s^2 4p^3 4d4f$, $4s^2 4p^2 4d^3$, $4s^2 4p^2 4d4f^2$, $4s4p^6$, $4s4p^5 4f$, $4s4p^3 4d^2 4f$, $4s4p^4 4d^2$, $4s4p^4 4f^2$, $4p^6 4d$, $4p^4 4d^3$, and $4p^5 4d4f$ configurations are included. The HFR values are improved on the basis of known data for Br-like Mo^{7+} [76]. This is the heaviest system in the Br-like isoelectronic sequence for

TABLE 1.2: Line transitions in Sn^{14+} and Sn^{15+} determined from fits to the spectra. Superscripts on line wavelengths indicate blended (bl), broad (br), or weak (w) lines. Starred (*) lines feature in the construction of the fluorescence curves. Line positions beyond 17 nm stem from measurements in first-order diffraction. Below 17 nm, line positions are established from second-order diffraction. Normalized intensities stem from the area-under-the-curve of fits to lines observed in the first-order diffraction. Normalized emissivities from FAC's CRm module are also presented. Transitions are of type $4p^m$–$4p^{m-1}4d$ (m = 6, 5 for respectively Sn^{14+} and Sn^{15+}); listed numbers refer to levels described in Table 1.3. *gA* factors stem from Cowan code calculations, except for transitions 0–3 and 0–6 in Sn^{14+}, which are calculated by FAC.

	Wavelength (nm)						
Ion	Experiment	Cowan	Intensity	*gA* (1/s)	Emissivity	Transition	Terms
14+	13.344*	13.343	1 000	1.8×10^{12}	1 000	0–12	$^1S_0$–$^1P_1$
	13.3431 [19]						
	13.3435 [65]						
	16.212	16.214	137	5.5×10^{10}	71	0–8	$^1S_0$–$^3D_1$
	16.2103 [65]						
	17.497		54	1.2×10^{3}	8	0–6	$^1S_0$–$^1D_2$
	17.905		63	1.6×10^{3}	15	0–3	$^1S_0$–$^3P_2$
	18.478	18.480	130	1.3×10^{8}	16	0–2	$^1S_0$–$^3P_1$
15+	13.129	13.135	159	3.0×10^{11}	654[1]	0–20	$^2P_{3/2}$–$^2D_{5/2}$
	13.393	13.387	1 000	2.9×10^{12}	1 000	0–19	$^2P_{3/2}$–$^2D_{5/2}$
	13.416	13.418	502	1.5×10^{12}	834	0–18	$^2P_{3/2}$–$^2P_{3/2}$
		13.477	-	2.0×10^{12}	31	1–22	$^2P_{1/2}$–$^2D_{3/2}$
	13.844*	13.844	334	8.4×10^{11}	469	0–17	$^2P_{3/2}$–$^2S_{1/2}$
	14.068	14.064	89	2.4×10^{11}	77	0–16	$^2P_{3/2}$–$^2D_{3/2}$
	14.384br	14.388	13	7.0×10^{11}	42	1–21	$^2P_{1/2}$–$^2P_{1/2}$
	14.903	14.904	59	1.5×10^{10}	33	0–15	$^2P_{3/2}$–$^2D_{5/2}$
	14.989w	14.993	16	1.7×10^{10}	4	1–18	$^2P_{1/2}$–$^2P_{3/2}$
	15.278	15.272	53	3.6×10^{9}	34	0–14	$^2P_{3/2}$–$^2F_{5/2}$
	15.510bl	15.503	119	2.9×10^{10}	57	0–13	$^2P_{3/2}$–$^2D_{5/2}$
	15.510bl	15.510	119	1.1×10^{9}	9	0–12	$^2P_{3/2}$–$^4P_{3/2}$
	15.528bl	15.527	120	6.7×10^{10}	39	1–17	$^2P_{1/2}$–$^2S_{1/2}$
	15.811	15.805	42	9.3×10^{10}	40	1–16	$^2P_{1/2}$–$^2D_{3/2}$
	16.320	16.330	140	5.6×10^{10}	118	0–10	$^2P_{3/2}$–$^4P_{5/2}$
	16.421	16.414	81	5.5×10^{10}	82	0–9	$^2P_{3/2}$–$^4F_{3/2}$
	16.498	16.492	103	2.4×10^{10}	103	0–8	$^2P_{3/2}$–$^4F_{5/2}$
	16.897	16.894	56	3.6×10^{10}	49	0–6	$^2P_{3/2}$–$^4P_{1/2}$
	17.143	17.152	61	5.9×10^{9}	47	0–5	$^2P_{3/2}$–$^2D_{3/2}$
	18.269	18.271	121	1.5×10^{9}	21	0–4	$^2P_{3/2}$–$^4D_{1/2}$
	18.513*	18.507	225	4.3×10^{8}	182	0–3	$^2P_{3/2}$–$^4D_{5/2}$

[1] High emissivity resulting from a larger *gA* factor calculated by FAC relative to that calculated with the Cowan code; see Sec. 1.5.3.

which the $4s^2 4p^4 4d$ level energies were found from an analysis of $4s^2 4p^5$–$4s^2 4p^4 4d$ transitions [76].

The ^2P term splitting of the ground-state configuration $4s^2 4p^5$ of Sn^{15+} was predicted to be $78\,358\,cm^{-1}$ [77, 78] on the basis of a larger set of isoelectronic data including Pd^{11+} [79], Ag^{12+} [80], and Cd^{13+} [81].

Starting out from this initial set of parameters, iterative refinement of the parameters allows for identification of 20 lines belonging to Sn^{15+} as $4s^2 4p^5$–$4s^2 4p^4 4d$ transitions and 17 level energies of the $4s^2 4p^4 4d$ configuration along with the $4s^2 4p^5\ ^2P$ ground term splitting. Our value of $78\,300(60)\,cm^{-1}$ for the ^2P term splitting is in excellent agreement with predictions.

A Cowan code fit to the available level energies to obtain optimal energy parameters leads to a root-mean-square deviation from experimental level energies of $302\,cm^{-1}$. The wavelength calibration uncertainty is approximately $150\,cm^{-1}$. The final results of the optimization procedure are listed in Table 1.3. The electrostatic energy parameters for the excited configurations were scaled by a factor 0.85 relative to their *ab initio* values while the spin-orbit parameters were not scaled. All configuration-interaction parameters in both parity systems were scaled by 0.85 except for the interaction between $4s^2 4p^4 4d$ and $4s 4p^6$ configurations which was varied as shown in Table 1.4. The scaling factors for the $4s^2 4p^4 4d$ configuration are in agreement with the isoelectronic trends for the sequence Y^{4+} [82], Zr^{5+} [83], Nb^{6+} [84], and Mo^{7+} [76], once these previous spectra are fitted with the same set of interacting configurations as used for Sn^{15+}. Several key Cowan scaling factors are presented along the Br-like isoelectronic sequence in Fig. 1.4. Only levels with $J \leq 5/2$ are included because of the unavailability of level energies for levels with $J > 5/2$ in Nb^{6+}, Mo^{7+}, and Sn^{15+}.

The Cowan fit to the experimental data yields *gA* factors that can be compared to experimental line intensities. Four transitions with high *gA* factors are expected around 13.4 nm. This quartet includes three lines to the ground state from upper levels 18, 19, and 20; cf. Table 1.3. The fourth transition originates from level 22, the highest excited level of the $4p^5 4d$ configuration, which decays to the $^2P_{1/2}$ ground level. Despite its large *gA* factor, this transition is not observed in the EBIT spectrum. CRm calculations show that the population of this upper level 22 is significantly smaller than that of neighboring levels, resulting in a low emissivity for this transition which is in line with our observations.

Typically, we find *gA* values obtained from Cowan and FAC to be consistent within a factor of two. One exception is the *gA* factor for the transition from level 20 ($^2D_{5/2}$) to the ground state. To understand this further, the transition is compared to the transition to the ground state from $^2D_{5/2}$ level 19 which is rather similar in wave function composition and shows no large differences in *gA* value between the two codes. The corresponding lines have a measured intensity ratio of 0.16 (transition 20–0/19–0), which is well explained by a *gA* factor ratio of 0.10 ($3.0 \times 10^{11}\,s^{-1} / 2.9 \times 10^{12}\,s^{-1}$) obtained from Cowan's code after a semiempirical fitting of the experimental line positions. The *gA* ratio using HFR

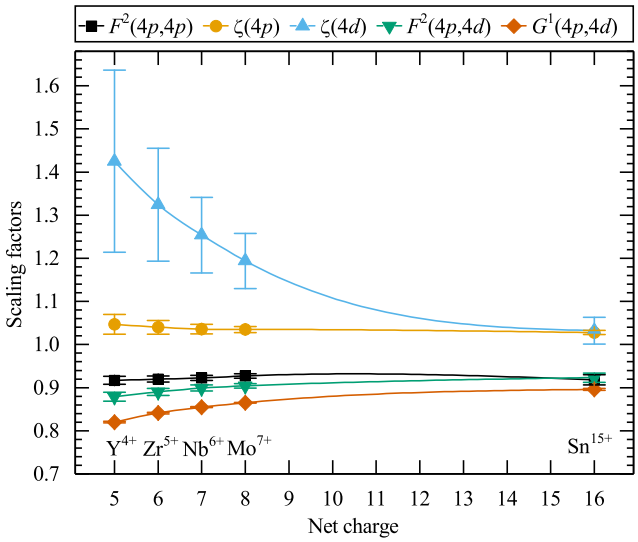

FIGURE 1.4: Empirical adjustments of scaling factors in the Cowan code calculations along the Br-like isoelectronic sequence (for details see text). Spline fits are drawn to guide the eye.

standard scaling, before any fitting, is however 1.8 ($2.2 \times 10^{12}\,\mathrm{s}^{-1}/1.2 \times 10^{12}\,\mathrm{s}^{-1}$), not too distinct from a value of 0.7 obtained from FAC calculations. It is also similar to a GRASP calculation indicating a ratio of 1.2 [60, 85].

The here-established quenching of oscillator strength of the 20–0 transition demonstrates the sensitivity of gA values to the exact wave-function composition.

The quality of the obtained complete set of Cowan code level energies is further illustrated by the identification of a particularly bright optical line observed in Ref. [39] at EBIT settings compatible with the production of Sn^{15+}. This line, predicted and observed at 538 nm, can be straightforwardly assigned to the yrast-type $(^3P)^4D_{7/2}$–$(^3P)^4F_{9/2}$ transition within the $4p^5 4d$ configuration.

AMBiT

We have calculated the energies of the $4p$–$4d$ transitions of Sn^{15+} using the particle-hole CI+MBPT (combination of configuration interaction and many-body perturbation theory [86]) method implemented in AMBiT [61]. Detailed explanations of the method, including formulae, can be found in Ref. [87], while the particle-hole formalism is introduced in Ref. [88]. Below, we present specific details of relevance to the current calculation.

We begin by generating the single-electron wavefunctions $|i\rangle$ by solving the self-consistent Dirac-Hartree-Fock (DHF) equations

$$\hat{h}_{\rm DHF}|i\rangle = \varepsilon_i|i\rangle,$$

where $\hat{h}_{\rm DHF}$ is the Dirac-Hartree-Fock operator (in atomic units):

$$\hat{h}_{\rm DHF} = c\boldsymbol{\alpha}\cdot\mathbf{p} + (\beta - 1)\,c^2 + V_{\rm DHF}(r),$$

where $V_{\rm DHF}(r)$ is the mean potential generated by the electrons included in the Hartree-Fock procedure plus the nuclear potential with finite-size corrections. This calculation is started from the V^{N-1} approximation, including the partially occupied $4p^4$ shell by scaling the filled shell. We also include additional terms to account for the Breit interaction and the Lamb shift, including the Uehling potential vacuum energy corrections and electron self-energy corrections [89–91].

Multi-electron wave functions are produced by taking Slater determinants of these $|i\rangle$. For each electronic configuration, we take all Slater determinants with a given total angular momentum projection M and diagonalize them over $\hat{\mathbf{J}}^2$ to form a basis of configuration state functions (CSFs) with definite total angular momentum J and projection M to be used in CI.

We now set the Fermi level above the $4s$ orbital, so there are effectively five valence electrons in Sn^{15+}. The $4s$ level is considered as a hole state, and we allow hole-particle excitations including this orbital. Note that at CI level this is exactly equivalent to having seven valence electrons (including the $4s^2$ shell in the valence set), provided that the same configurations are included in the CI. However, from a MBPT perspective it reduces the overall size of subtraction diagrams [88]. The CI space consists of configurations generated by single and double electron excitations up to $8spdf$ orbitals from the reference configurations $4p^5$, $4p^4 4d$, $4p^3 4d^2$, $4p^2 4d^3$, $4p^4 5s$, and $4s^{-1}4p^6$. Additional configurations consisting of a particle-hole excitation from the reference set along with a valence electron excitation were also included. In order to reduce the size of the CI calculation, without sacrificing accuracy, the "emu CI" technique described in Ref. [92] is used. To summarize, of the N CSFs in the CI basis, only a much smaller number N_s of usually lower energy CSFs will dominate the expansion of the states of interest. For those important configurations, all interactions are accounted for. However, interactions between configurations outside of this smaller set are neglected. To achieve this, we place the N_s important CSFs in the top of the CI matrix and set off-diagonal elements that correspond to interactions between higher energy states to 0. As an example, for the even-parity $J = 7/2$ configurations we had $N = 407\,271$ and $N_s = 40\,704$, reducing the number of calculated elements of the CI matrix by a factor of five.

TABLE 1.3: Energy levels of Sn^{14+} and Sn^{15+}. Energy levels under Experiment are determined from wavelengths shown in Table 1.2, and in addition the Cowan results from the fit to experimental data are listed. Furthermore, theoretical level energies of Sn^{14+} are calculated by FSCC (reproduced from Ref. [39]), and by GRASP in the case of Sn^{15+} (reproduced from Ref. [60]) as well as by AMBiT. Sn^{15+} levels with $J > 5/2$ are not listed as transitions from these levels are not observed in our spectra. Up to three components of the eigenvector composition are listed for each configuration.

			Level energy (cm^{-1})							
Ion	Config.	Level	Experiment	Cowan	FSCC [39]		J	Percentage eigenvector composition		
14+	$4p^6$	0	0	0	0		0	^1S		
	$4p^5 4d$	1		532 121	531 833		0	98% $(^2P)^3P$		
		2	541 212	541 118	540 795		1	89% $(^2P)^3P$	9% $(^2P)^3D$	
		3	558 523	558 571	558 339		2	63% $(^2P)^3P$	30% $(^2P)^3D$	5% $(^2P)^3F$
		4	560 487[a]	560 438	560 042		3	69% $(^2P)^3F$	21% $(^2P)^1F$	9% $(^2P)^3D$
		5		563 501	561 822		4	98% $(^2P)^3F$		
		6	571 490	571 828	571 047		2	44% $(^2P)^1D$	33% $(^2P)^3F$	11% $(^2P)^3P$
		7	592 103[a]	591 945	592 565		3	63% $(^2P)^3D$	35% $(^2P)^1F$	
		8	616 892	616 753	617 525		1	84% $(^2P)^3D$	8% $(^2P)^3P$	5% $(^2P)^1P$
		9		632 893	632 338		2	58% $(^2P)^3F$	32% $(^2P)^1D$	7% $(^2P)^3D$
		10		649 941	649 997		2	50% $(^2P)^3D$	24% $(^2P)^3P$	21% $(^2P)^1D$
		11		658 062	658 463		3	43% $(^2P)^1F$	29% $(^2P)^3F$	26% $(^2P)^3D$
		12	749 429	749 449	750 368		1	92% $(^2P)^1P$	5% $(^2P)^3D$	1% $(^2P)^3P$
Ion	Config.	Level	Experiment	Cowan	GRASP [60]	AMBiT	J	Percentage eigenvector composition[b]		
15+	$4p^5$	0	0	0	0	0	3/2	^2P		
		1	78 300	78 300	77 573	78 391	1/2	98% ^2P		
	$4p^4 4d$	2	540 160	539 988	552 900	540 618	3/2	56% $(^3P)^4D$	13% $(^3P)^4P$	12% $(^1D)^2D$
		3		540 344	552 374	540 799	5/2	68% $(^3P)^4D$	8% $(^1D)^2D$	7% $(^3P)^4F$
		4	547 380	547 330	561 866	547 849	1/2	38% $(^3P)^4D$	25% $(^1D)^2P$	20% $(^3P)^2P$
		5	583 330	583 015	595 347	585 107	3/2	31% $(^1S)^2D$	23% $(^3P)^4P$	18% $(^3P)^4F$
		6	591 820	591 934	610 436	593 334	1/2	64% $(^3P)^4P$	18% $(^3P)^2P$	10% $(^1D)^2P$
		7		604 177	616 910	604 006	1/2	60% $(^3P)^4D$	14% $(^1D)^2P$	12% $(^3P)^4P$
		8	606 130	606 367	616 888	607 902	5/2	49% $(^3P)^4F$	28% $(^1S)^2D$	11% $(^3P)^4P$
		9	608 980	609 246	623 121	610 977	3/2	41% $(^3P)^4F$	23% $(^3P)^4P$	16% $(^1D)^2D$
		10	612 750	612 365	628 411	615 164	5/2	34% $(^3P)^4P$	21% $(^3P)^2F$	19% $(^3P)^4F$
		11		620 095	634 622	620 638	3/2	31% $(^3P)^4D$	16% $(^1D)^2D$	15% $(^1D)^2P$
		12	644 750	644 728	660 531	645 662	3/2	29% $(^3P)^4P$	24% $(^1D)^2P$	22% $(^3P)^2P$
		13	644 750	645 021	661 069	646 848	5/2	29% $(^1D)^2D$	28% $(^1D)^2F$	15% $(^3P)^2D$
		14	654 540	654 802	670 067	656 739	5/2	50% $(^3P)^2F$	22% $(^3P)^4P$	17% $(^1D)^2F$
		15	671 010	670 948	690 149	673 929	5/2	36% $(^1D)^2D$	34% $(^1D)^2F$	11% $(^3P)^4P$
		16	710 810	711 019	723 750	713 461	3/2	34% $(^1S)^2D$	22% $(^1D)^2P$	20% $(^3P)^4F$
		17	722 330	722 341	760 578	724 932	1/2	67% $(^1D)^2S$	15% $(^2S)^2S$	7% $(^1D)^2P$
		18	745 420	745 278	765 637	748 655	3/2	39% $(^3P)^2P$	21% $(^1D)^2P$	21% $(^1D)^2D$
		19	746 660	746 998	763 991	750 125	5/2	50% $(^3P)^2D$	25% $(^1S)^2D$	13% $(^1D)^2D$
		20	761 670	761 325	780 364	764 672	5/2	36% $(^1S)^2D$	17% $(^3P)^2D$	16% $(^3P)^2F$
		21	773 520	773 307	793 949	775 883	1/2	45% $(^3P)^2P$	42% $(^1D)^2P$	8% $(^1D)^2S$
		22		820 293	840 862	823 384	3/2	50% $(^3P)^2D$	22% $(^1S)^2D$	9% $(^3P)^2P$

[a] Level energies were determined in Ref. [39] relative to level 2 by measuring transitions 3–7, 4–7, and 6–7.
[b] All components belong to the $4p^4 4d$ configuration except for level 17, where the second component belongs to $4s4p^6$.

TABLE 1.4: Cowan code Hartree-Fock with relativistic corrections (HFR) and least-squares-fitted (LSF) parameter values of the $4s^2 4p^5 4d$ and $4s^2 4p^4 4d$ configurations respectively in Sn^{14+} and Sn^{15+}. All parameters are given in units of cm^{-1}. One-standard-deviation uncertainties are given in brackets.

Parameter	Sn^{14+}			Sn^{15+}		
	HFR[a]	LSF	LSF/HFR[b]	HFR[a]	LSF	LSF/HFR[b]
E_{average}	632 080	629 400(327)	-2 680	671 287	669 270(98)	-2 017
$F^2(4p,4p)$	-	-	-	133 798	123 714(1 216)	0.925(9)
$\zeta(4p)$	50 300	51 428(751)	1.022(15)	51 881	53 251(187)	1.026(4)
$\zeta(4d)$	5 348	5 823(228)	1.089(43)	5 602	5 788(150)	1.033(27)
$F^2(4p,4d)$	125 410	115 494(1 707)	0.921(14)	127 338	117 332(1 054)	0.921(8)
$G^1(4p,4d)$[c]	158 897	142 206(674)	0.895(4)	161 200	144 568(273)	0.897(2)
$G^3(4p,4d)$[c]	100 630	90 060(427)	0.895(4)	102 264	91 712(173)	0.897(2)
$^1D(4s4d,4p4p)$[d]				167 595	147 825(787)	0.882(5)
σ		279			302	

[a] Average energies are adjusted so that the energy of the ground level is zero in calculations with 0.85 scaling of all electrostatic parameters.
[b] The value given for E_{average} represents the difference between LSF and HFR value.
[c] Parameters are tied at their HFR ratio at the fitting.
[d] Interaction between $4s^2 4p^4 4d$ and $4s^1 4p^6$ configurations in Sn^{15+}.

Core-valence interactions involving the other core levels (up to $3spd$) are small since the core and valence electrons are well separated in energy. In the CI+MBPT method these are treated perturbatively up to second order by modifying the Slater integrals [86]. In the diagrammatic expansion we included virtual orbitals up to $30spdfg$ and all orbitals that were frozen at CI level.

The AMBiT calculations are done at a level similar to previous work on Sn^{7+} [39]. This case also has five valence electrons; however, we are now interested in high-energy transitions between configurations, rather than levels within a multiplet ($4d^5$ in the case of Sn^{7+}). The results are shown in Table 1.3. We find a systematic offset in the AMBiT $4p^4 4d$ energy levels compared to experiment of 2 100(900) cm^{-1}, which originates from the relaxation of the $4p$ orbitals in the different configurations and is not completely accounted for by the CI and MBPT approach. Our overall relative accuracy is $\sim$0.3%, which compares favorably with the previous theory 2.6% [60]; cf. Table 1.3. The accuracy of AMBiT very nearly enables the direct identification of the observed lines without the need of semiempirical scaling parameters as in the case of the Cowan code, particularly so when correcting for the observed systematic shifts in level energies.

1.6 Conclusion

We study the extreme ultraviolet spectra near 13.5 nm wavelength of Sn^{13+}–Sn^{15+} ions as measured in an electron-beam ion trap. A matrix inversion method enables the reevaluation of resonance transitions in Sn^{13+} and Sn^{14+} ions. In the latter ion, three additional EUV lines confirm its previously established level structure.

For Sn^{15+} we present the first line spectrum and use the Cowan code for line identification and assignments. These assignments are furthermore strengthened by the collisional-radiative modelling capabilities of the Flexible Atomic Code, thus including line emissivities in the identification process by modeling the EBIT plasma. Using the 20 lines identified, we establish 17 level energies of the $4p^4 4d$ configuration as well as the fine-structure splitting of the $4p^5$ ground state. We find that strong $4p$–$4d$ transitions lie in the small 2% bandwidth around 13.5 nm that is so relevant for plasma light sources for state-of-the-art nanolithography. Furthermore, we provide state-of-the-art *ab initio* calculations of Sn^{15+} using the configuration-interaction many-body perturbation code AMBiT and find it to be in excellent agreement with the experimental data at a 0.3% average deviation. These AMBiT calculations outperform other theory work by almost an order of magnitude.

1.7 Acknowledgments

Part of this work was carried out at the Advanced Research Center for Nanolithography, a public-private partnership between the University of Amsterdam, the Vrije Universiteit Amsterdam, the Netherlands Organization for Scientific Research (NWO), and the semiconductor equipment manufacturer ASML. This project has received funding from European Research Council (ERC) Starting Grant No. 802648 and is part of the VIDI research program with Project No. 15697, which is financed by NWO. J.S and O.O.V. thank the MPIK in Heidelberg for the hospitality during the measurement campaign.

2

EUV spectroscopy of Sn^{5+}–Sn^{10+} ions in an electron-beam ion trap and laser-produced plasmas

Z. Bouza[‡], J. Scheers[‡], A. Ryabtsev, R. Schupp, L. Behnke, C. Shah, J. Sheil, M. Bayraktar, J. R. Crespo López-Urrutia, W. Ubachs, R. Hoekstra, and O. O. Versolato

Journal of Physics B: Atomic, Molecular and Optical Physics **53**, 195001 (2020)

Emission spectra from multiply-charged Sn^{5+}–Sn^{10+} ions are recorded from an electron-beam ion trap (EBIT) and from laser-produced plasma (LPP) in the extreme ultraviolet range relevant for nanolithographic applications. Features in the wavelength regime between 12.6 and 20.8 nm are studied. Using the Cowan code, emission line features of the charge-state-resolved Sn ion spectra obtained from the EBIT are identified. Emission features from tin LPP either from a liquid microdroplet or planar solid target are subsequently identified and assigned to specific charge states using the EBIT data. For the planar solid tin target, the $4d$–$5p$ transitions of Sn^{8+}–Sn^{10+} ions are shown to dominate the long-wavelength part of the measured spectrum and transitions of type $4d$–$4f$ + $4p$–$4d$ are visible in absorption. For the droplet target case, a clear increase in the charge-state distribution with increasing laser intensity is observed. This qualitatively demonstrates the potential of using long-wavelength out-of-band emission features to probe the charge states contributing to the strong unresolved transition array at 13.5 nm relevant for nanolithography.

[‡]These authors contributed equally to this work.

2.1 Introduction

Highly charged Sn ions in laser-driven transient and dense plasmas are the emitters of extreme ultraviolet (EUV) light near 13.5 nm that is used in nanolithographic applications [12–14, 24]. In such applications, hot plasma is produced when molten Sn microdroplets are illuminated by energetic laser pulses. The responsible ions for emitting EUV photons near 13.5 nm are Sn^{8+}–Sn^{14+} with their resonance transitions $4p^6 4d^m$–$4p^5 4d^{m+1}$ and $4d^m$–$4d^{m-1}4f$ (m = 6–0) [8, 12, 24]. Spectroscopic investigation of these plasmas is challenging due to the many, densely-packed transitions in these open-4d-subshell Sn ions. Furthermore, spectral lines belonging to adjacent ionic charge states may blend in wavelength. Charge-state–resolved measurements would facilitate line identifications in these complex systems. Such measurements can, e.g., be obtained from single-charge-state beam experiments of which the charge-exchange spectroscopy (CXS) of tin ions by Ohashi *et al.* [37] is a notable example. Charge-state-resolved tin spectra can also be obtained from an electron-beam ion trap (EBIT), using, e.g., matrix inversion techniques to deconvolve the mixed-charge-state EBIT spectra [40].

In EUV nanolithography machines, molybdenum-silicon multi-layer mirrors are used as projection optics. These optics are characterized by a 2% reflectivity bandwidth centered at 13.5 nm wavelength [25, 93]. The EUV radiation generated from the Sn laser-produced plasma (LPP) overlaps with the peak reflectivity of these mirrors. Most of the detailed spectroscopic studies in the literature focus on emission near 13.5 nm [9–12, 16–19, 35, 40, 45]. However the majority of the EUV emission occurs out-of-band, i.e., outside of the 2% reflectivity bandwidth [24]. From the application perspective, this out-of-band radiation reduces the efficiency of converting drive laser light into useful EUV photons. Moreover, such radiation can influence the optics lifetime or introduce unwanted thermal loads in the scanner [94, 95]. It is thus of particular interest and importance to quantify tin spectra over the full spectral band. Recent studies have shed light on the short-wavelength side of the out-of-band emission from LPP in the 7–12 nm range [22], complementing earlier work [9]. These insights regarding short-wavelength EUV radiation were subsequently used to obtain the relative contributions of charge states Sn^{9+}–Sn^{15+} to the main unresolved emission feature at 13.5 nm, and to successfully diagnose the plasma [15], obtaining, for instance, the temperature of an industrial EUV light source.

In this work, emission features of the multiply-charged Sn^{5+}–Sn^{10+} ions in the long-wavelength, 12.6–20.8 nm region are studied. Spectra are obtained from an EBIT and from LPP. Understanding the emission features enables quantifying the contributions in LPP from the lower charge states that could not be assessed from the previous short-wavelength studies [15, 22]. First, following the procedure outlined in Ref. [40], mixed-charge-state EBIT spectra are deconvolved to obtain single-charge-state spectra. Next, the line features from Sn^{5+}–Sn^{10+} ions are assigned using the semi-empirical Cowan code [58, 96], which allows for adjusting scaling factors in the calculation in order to fit observed

spectra using initial preliminary assignments. These identifications are compared to literature where available. Finally, spectral features in the emission from Sn LPP, generated from liquid droplets as well as from planar solid tin targets over a wide range of laser intensities (and thus, plasma temperatures), are identified using the EBIT spectra. These investigations extend the set of diagnostic tools for monitoring EUV-producing tin LPP in an industrial setting.

2.2 Experiment

Two types of experiments are introduced in the following. First, the experimental setup used to record emission spectra of trapped Sn ions at the FLASH-EBIT facility [62] at the Max Planck Institute for Nuclear Physics in Heidelberg, Germany, is discussed. Second, experiments on laser-produced tin plasma that are carried out at the Advanced Research Center for Nanolithography (ARCNL) in Amsterdam, The Netherlands, are presented.

2.2.1 Electron-beam ion trap (EBIT)

Spectroscopic measurements of Sn ions in the EUV regime have been performed using the FLASH-EBIT facility [62]. In an EBIT, an electron beam is used to trap, ionize, and excite ions for spectroscopic measurements. It enables the investigation of a wide range of Sn ion charge states. The FLASH-EBIT can deliver an electron beam with well-defined kinetic energies. A 6 T magnetic field is applied to guide and compress the electron beam down to a diameter of about 50 µm at the center of the trap. This magnetic field is generated by a pair of superconducting Helmholtz-coils. A molecular beam of tera-i-propyltin ($C_{12}H_{18}Sn$) is injected into the trap center region. Molecules are dissociated while crossing the electron beam. The electron beam rapidly excites, ionizes, and traps the Sn ions up to the desired charge state, while the lighter elements overcome the trapping potential and leave the EBIT. Trapping of a specific charge state can be achieved by adjusting the acceleration potentials that define the kinetic energy of the electron beam.

Radiation by the Sn ions is dispersed by a 1 200-lines/mm flat-field, grazing-incidence grating with a variable line spacing [63] and is recorded on a Peltier-cooled charge-coupled device (CCD) camera. Background frames are recorded for the same exposure time as in the measurements with Sn present in the trap, and these images were then subtracted from the recorded plasma emission to eliminate the dark counts as well as read-out counts. The resulting CCD images are cropped and corrected for spectrometer aberrations. Subsequently, the images are integrated along the non-dispersive axis. The resulting spectra are then corrected for diffraction efficiency, as well as the quantum efficiency of the camera following Ref. [97] (also see, e.g., Ref. [98]). The wavelength

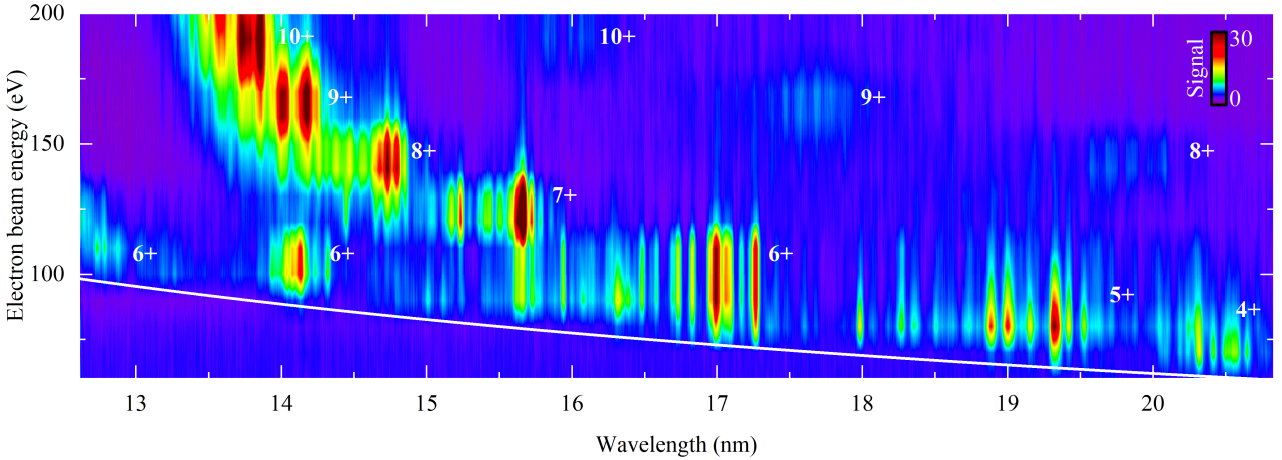

FIGURE 2.1: Two-dimensional spectral intensity map of Sn^{4+}–Sn^{10+} emission constructed from EBIT measurements (1.5 mA series). The map is produced by interpolating along the electron-beam energy between discrete spectra which are taken at 10-eV steps. The color bar indicates the signal or the emission intensity. The white line indicates where the electron-beam energy equals the photon energy (see main text). Charge-state-specific emission islands are labeled by the charge state of the emitting Sn ion.

calibration of the spectrometer is performed by injecting oxygen into the trap, using well-known O^{2+}–O^{4+} lines in the EUV range [64]. A wavelength range spanning 12.6–20.8 nm is captured with a resolution of about 0.03 nm at full width at half maximum (FWHM). A more detailed description of the EBIT experiments is given in Refs. [38–40].

Two measurement series are conducted. In the first series, the electron-beam energy is increased from 60 to 200 eV in steps of 10 eV. The electron-beam current is set to a constant 1.5 mA. Sn charge states 4+ to 10+ are observed using these EBIT settings. A two-dimensional map (wavelength, electron-beam energy), composed by interpolating between discrete EBIT spectra, is presented in Fig. 2.1. In the second series, the electron-beam energy is increased from 180 to 610 eV in steps of 5 eV, and the electron-beam current is set to a constant 13 mA. The Sn charge states that can be observed in this series range from 8+ to 20+.

2.2.2 Laser-produced plasma (LPP)

Two different experimental setups are used to produce Sn plasmas with a laser: (i) a droplet tin target and (ii) a planar solid tin target. Both experimental setups are detailed below. The targets are irradiated by a Nd:YAG laser operating at a wavelength of 1064 nm, with a Gaussian pulse length of 10 ns FWHM.

In both setups, spectral emission from the Sn-produced plasma is measured under an angle of 60° with respect to the propagation direction of the laser light, using a broad-band transmission grating spectrometer [99, 100]. The spectrometer is operated with an entrance slit width of 25 μm and a 10 000 lines/mm transmission grating achieving a FWHM instrument resolution of 0.1 nm at 13 nm [23, 99]. The recorded wavelength regime is 5–25 nm. The diffracted light is recorded on a back-illuminated CCD from Greateyes (GE2048 512BI UV1), cooled to −30°C to reduce thermal noise. Background frames are recorded for the same exposure time as in the measurements with Sn plasma present, and these images were then subtracted from the recorded plasma emission to eliminate the dark counts as well as read-out noise. The exposure time is varied from 1–5 s to collect sufficient signal-to-noise ratio. The resulting CCD images are cropped and corrected for shear and tilt introduced by a slight misalignment of the slit and grating with respect to the CCD pixel array. Subsequently, the images are integrated along the non-dispersive axis. The resulting spectra are then corrected for first- and second-order diffraction efficiency, as well as the quantum efficiency of the camera.

The dispersion of the grating is obtained by observing well-documented Al^{3+} and Al^{4+} lines [64] from a laser-produced Al plasma [23]. Based on the position of the zeroth diffraction order, and known tin lines, an accurate wavelength calibration is obtained.

TABLE 2.1: Average wavelength of various transition arrays in Sn^{q+} (q = 5–10), see also Fig. 2.4. Results obtained from the Cowan code are presented as gA-weighted average wavelength of the transition array (first moment of the distribution according to UTA formalism [101, 102]), and the width represents the standard deviation of the distribution (square root of the variance). CXS results (center of the distribution of emission lines) are obtained from collisions of $Sn^{(q+1)+}$ with Xe, reproduced from Ref. [37]. We note that the Table entries from Ref. [37] may refer to the average position of the $4d$–$4f$ and $4p$–$4d$ transitions arrays combined.

		Average wavelength (nm)		
Ion	Transition	CXS [37]	COWAN	Width (nm)
Sn^{5+}	$4d$–$4f$	19.0	19.4	0.6
	$4p$–$4d$	–	18.0	0.1
Sn^{6+}	$4d$–$4f$	16.0	17.1	0.5
	$4p$–$4d$	–	15.9	1.2
	$4d$–$5f$	–	14.2	0.4
	$4d$–$6f$	–	13.0	0.3
Sn^{7+}	$4d$–$4f$	15.6	15.8	0.7
	$4p$–$4d$	–	15.1	0.6
	$4d$–$5f$	12.5	12.6	0.3
Sn^{8+}	$4d$–$4f$	14.2	15.0	0.7
	$4p$–$4d$	–	14.3	0.7
	$4d$–$5p$	19.5	19.8	0.6
Sn^{9+}	$4d$–$4f$	14.0	14.4	0.7
	$4p$–$4d$	–	13.9	0.6
	$4d$–$5p$	17.7	17.7	0.5
Sn^{10+}	$4d$–$4f$	13.8	13.9	0.4
	$4p$–$4d$	–	13.6	0.5
	$4d$–$5p$	16.0	16.0	0.5

Droplet tin target

Molten Sn microdroplets of 99.995% purity with a diameter of 18 μm are dispensed from a droplet generator inside a vacuum vessel of 5×10^{-7} mbar pressure. The droplets travel at a speed of approximately 10 m/s in the vacuum vessel and pass through a horizontal light sheet produced by a He-Ne laser. The light scattered by the droplets is detected using a photomultiplier tube which subsequently triggers the Nd:YAG laser system. The droplets are irradiated by a laser pulse with an 80 μm (FWHM) Gaussian spot size. Additional details regarding the droplet-based experimental setup can be found in Ref. [28].

Planar solid tin target

A 1 mm thick Sn planar solid polycrystalline target of 99.995% purity is mounted onto a 2D-translation stage in a vacuum vessel which is kept at a pressure of 10^{-6} mbar. The solid target is irradiated by the same Nd:YAG laser system as is used for the droplet targets. The FWHM spot size at the planar target surface is 130 μm. Only two consecutive pulses are recorded on the same spot of the Sn target to prevent any influence of target deformation on the recorded spectra. The translation stage enables a stepwise motion of the target to guarantee a fresh target spot after each series of two pulses. Additional details regarding the planar solid-based experimental setup can be found in Ref. [103].

2.3 Measurements

In the following, we first discuss the results of the EBIT measurements. Spectra from individual charge states are presented (see Fig. 2.2), as obtained from EBIT measurements by using the matrix inversion introduced in Ref. [40]. Identifications of the observed line features are made using the Cowan code (Figs. 2.2 and 2.3). An overview of the wavelength positions of relevant configurations is presented in Fig. 2.4 as well as in Table 2.1. Next, the EBIT data is employed to qualitatively study the contribution of individual charge states to the emission from laser-produced plasmas created from both droplet or planar solid tin targets (see Fig. 2.5).

2.3.1 EBIT spectra

In Fig. 2.1, a two-dimensional (wavelength, electron-beam energy) spectral intensity colormap of Sn ions constructed from EBIT measurements is presented (1.5-mA series). Emission features from Sn^{4+} to Sn^{10+} ions can be observed. The white line indicates the threshold at which the photon energy equals the electron-beam energy, above which a particular transition can energetically be excited directly by single-electron impact.

The individual EBIT spectra contain a mixture of charge states, dependent on EBIT conditions such as electron-beam energy and current. Following the procedure outlined

in Ref. [40], spectra of the individual charge states are obtained using a matrix inversion method. This method enables unraveling blended spectra by assuming that every spectrum contains a linear combination of contributions from individual charge states. The contributions from these charge states are weighted by their respective fluorescence curve (a curve defined as the emission intensity of the various spectral lines as function of the electron-beam energy). Following the work of Scheers *et al.* [40], to obtain fluorescence curves, we project vertical regions of interest from the data as shown in Fig. 2.1. Several lines per charge states are used to construct a generic fluorescence curve. Chosen lines are preferably isolated, mostly outside of dense spectral regions. The observed energy dependencies of the line strengths are typically very similar for all lines associated with a particular charge state. Individual fluorescence curves are normalized and subsequently averaged such that a generic fluorescence curve per charge is constructed. A matrix inversion technique is subsequently invoked. In it, the colormaps are represented by a matrix E. The matrix elements of $\boldsymbol{E}$ contain spectral intensities directly obtained from measurements. Fluorescence curves span a fluorescence matrix $\boldsymbol{F}$ in $\boldsymbol{FS} = \boldsymbol{E}$, where $\boldsymbol{S}$ contains the individual, charge-state-resolved spectra. The solution of matrix $\boldsymbol{S}$ is given by $\boldsymbol{S} = (\boldsymbol{F}^T\boldsymbol{F})^{-1}\boldsymbol{F}^T\boldsymbol{E}$.

The charge-state-resolved spectra obtained from both the lower- and higher-current measurement series are nearly identical. An improved signal-to-noise ratio is obtained in the higher-current case. A consequence of using a different electron-beam current might be variations in level population within the respective tin ions and therefore line intensities may change [67], but such an effect was not observed in our spectra. Because of the higher signal-to-noise ratio, the higher-current series is used in the following for the spectra of Sn^{8+}–Sn^{10+}. The lower-current series is used for Sn^{5+}–Sn^{7+} as these ions could not be observed in the higher-current series. Sn^{4+} is not included because its dominant line features largely fall outside the spectrometer range [37, 104].

In the following, the spectral fingerprints of the EBIT spectra from individual charge states are discussed. For convenience, the transitions of type of $4d^m$–$4d^{m-1}4f$, $4p^64d^m$–$4p^54d^{m+1}$, $4d^m$–$4d^{m-1}5f$, $4d^m$–$4d^{m-1}6p$, $4d^m$–$4d^{m-1}6f$ and $4d^m$–$4d^{m-1}5p$, where m = 9–4 in the case of Sn^{5+} to Sn^{10+}, will be written as $4d$–$4f$, $4p$–$4d$, $4d$–$5f$, $4d$–$6p$, $4d$–$6f$ and $4d$–$5p$, respectively.

The Hartree-Fock method with relativistic corrections incorporated in the RCN-RCN2-RCG chain of the Cowan code [58, 96] is used for the calculation of energy levels, transition wavelengths, and gA values (multiplicity g times the Einstein coefficient A). Spectral line intensities recorded from an EBIT may deviate from calculated gA values (see, e.g., Ref. [67]) as excited-state populations, which together with these gA values determine the line intensities, depend on the specifics of electron impact excitation. Inclusion of such effects in our calculations would require detailed collisional-radiative modeling [105] which is beyond the scope of the current paper. In this work, we find that emission features can here be reliably identified using gA values.

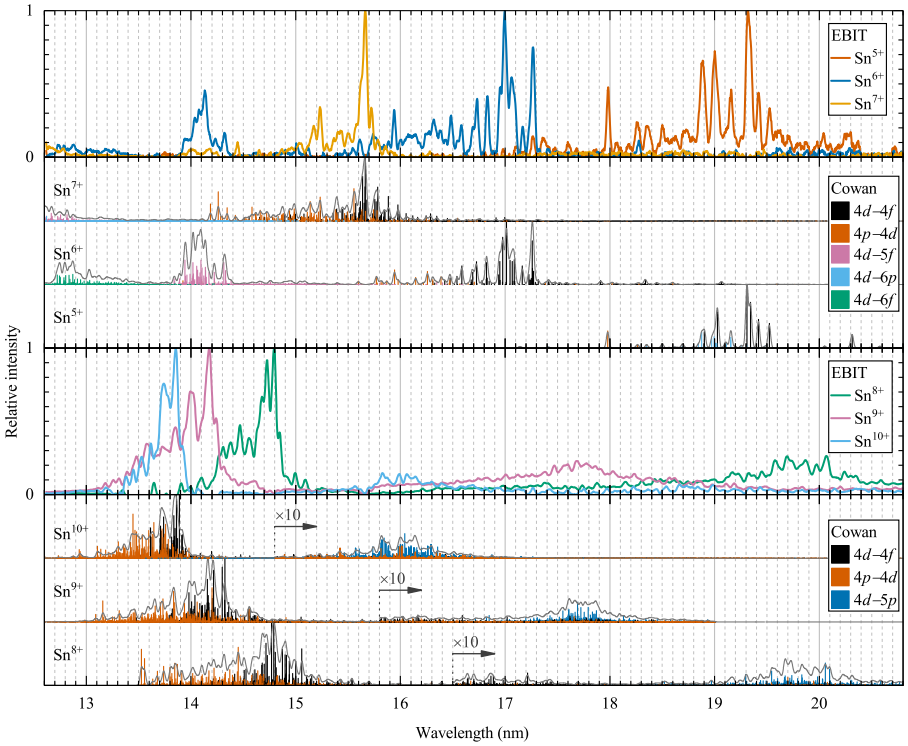

FIGURE 2.2: Normalized charge-state-resolved spectra from Sn^{5+}–Sn^{10+} ions obtained from the EBIT measurements using the matrix inversion method (see main text). The results for Sn^{5+}–Sn^{7+} originate from the 1.5 mA electron-beam current measurements, and the Sn^{8+}–Sn^{10+} results derive from the 13 mA current measurements (see main text). Results from Cowan code calculations are presented with *gA* factors normalized to maximum *gA* value for the corresponding charge state (shown as sticks in the plot). The envelopes (shown in gray) represent a convolution of the *gA* factors with a Gaussian function accounting for the spectrometer resolution (0.03 nm FWHM). These envelopes are separately normalized to a maximum value of one at their respective maximum.

Spectrum of Sn^{5+}

Strong emission line features of Sn^{5+} are observed between 18–20 nm in the EBIT spectrum (Fig. 2.2). These line features are related to transitions of type $4d$–$4f$ and $4d$–$6p$. They were identified in Ref. [10], where the Cowan code was used to analyze measurements performed using a spark source. A comparison between our spectrum with *gA* factors calculated by Cowan code using scaling parameters based on the line identifications from Ref. [10], convoluted with the spectrometer resolution (0.03 nm FWHM), is presented in Fig. 2.2. Calculations and experiment are in good agreement. Further, we observe a strong and isolated line at 17.98 nm wavelength. Cowan code calculations indicate that this feature can be identified as the $4p^6\ 4d^9\ {}^2D_{5/2}$–$4p^5\ 4d^{10}\ {}^2P_{3/2}$ transition.

Spectrum of Sn^{6+}

In the case of Sn^{6+}, prominent emission line features can be observed in Fig. 2.1 in three separate wavelength regions: 12.6–13.6 nm, 14–14.5 nm, and 16–17.5 nm. For the identification of the emission line features between 12.6–14.5 nm, we use the Cowan atomic structure code. The level energies of the $4d^7 5f$ and $4d^7 6f$ configurations of Sn^{6+} are optimized using configuration-interaction between the following configurations: $4p^6(4d^8 + 4d^7 5s + 4d^6 5s^2)$ in the even set and $4p^6 4d^7(5p + 6p + nf\ (n = 4\text{–}7)) + 4p^5(4d^9 + 4d^8 5s)$ in the odd set. The fitting of the levels of the $4p^6 4d^8$, $4p^6 4d^7(5p + 4f)$ and $4p^5 4d^9$ configurations was performed using known data [11, 106]. The electrostatic energy parameters of the unknown configurations $4d^7 6p$, $4d^7 7f$ and $4p^5 4d^8 5s$ were scaled by a rather standard factor 0.85 with respect to their *ab initio* Hartree-Fock with relativistic corrections (HFR) values. The interaction integrals were scaled by 0.8. The *ab initio* HFR values for the $4d^7 5f$ and $4d^7 6f$ configurations were improved using the same scaling factors and effective parameters as were obtained previously for $4d^7 4f$. The final fitted and adopted energy parameters as well as scaling factors for configurations $4d^7 nf$ ($n = 4$–6) and $4p^5 4d^9$ responsible for most of the features in our EBIT spectrum, including those in the 16–17.5 nm region, are presented in Table 2.2.

The results of the Cowan code calculations for both $4d$–$5f$ and $4d$–$6f$ transitions are presented in Fig. 2.3, along with the spectrum of Sn^{6+} obtained from the matrix inversion technique. The heights of the vertical lines represent the calculated *gA* values for individual lines within the transition arrays $4d$–$(5f + 6f)$. They are normalized to the strongest transition in the here-presented wavelength range. The gray envelope is a convolution of these *gA* factors with a Gaussian function representing the spectrometer resolution (0.03 nm FWHM). This envelope is separately normalized to a value of one for better visibility. The EBIT spectrum of Sn^{6+} presents a smaller relative emission amplitude, by a factor of approximately two, in the 12.6–13.2 nm range as would be expected from a direct comparison of the calculated *gA* values of the $4d$–$5f$ to the $4d$–$6f$ transitions. This relatively small amplitude may in part be explained by the fact that the

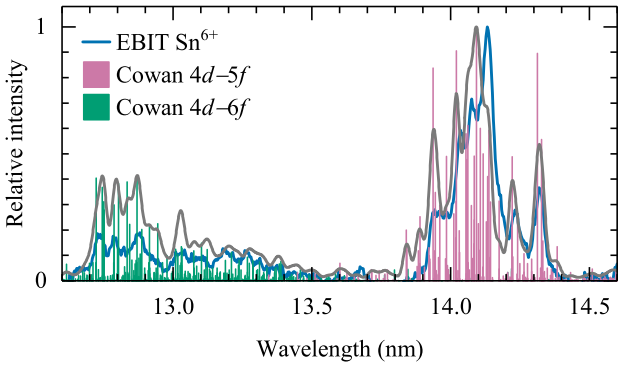

FIGURE 2.3: Identification of spectral features in Sn^{6+} obtained from the EBIT measurements using the matrix inversion method (see text). Vertical lines indicate calculated *gA* factors of $4d–(5f+6f)$ transitions normalized to the strongest transition in this range. The gray envelope is a convolution of the presented *gA* values with a Gaussian function accounting for the spectrometer resolution of 0.03 nm (FWHM). The envelope is separately normalized for better visibility.

electron-beam energy is barely sufficient to excite to the levels giving rise to the $4d–6f$ transitions. Collisional-radiative modeling, left for future work, would enable assessing the dependence of the observed line strengths on electron-beam energy and its density. In general, our calculations, including those for the $4d–4f$ and $4p–4d$ transitions, are in good agreement with the spectra (see Fig. 2.2).

Spectrum of Sn^{7+}

Emission line features of Sn^{7+} lie between 15–16 nm, as seen from Fig. 2.2. These line features correspond to the $4d–4f$, $4p–4d$ transitions identified by Churilov and Ryabtsev [17] employing a vacuum spark setup. Fig. 2.2 also shows transition probabilities for the Sn^{7+} ion spectrum calculated with the Cowan code using scaling parameters from Ref. [17]. A convolution of these transitions with Gaussian function accounting for the spectrometer resolution is in agreement with the experimental spectrum. The $4d–6p$ transitions are not visible in our EBIT spectra. However, we note that our calculations of the $4d–6p$ transitions are in excellent agreement with unidentified spectral features around 14 nm observed in charge-exchange spectroscopy, whereby spectra resulting from collisions of Sn^{8+} with He and Xe were observed [37]. The small feature at the edge of our detection region (near 12.8 nm) may be tentatively associated with the $4d–5f$ transition array as was previously noted in Ref. [9].

Spectrum of Sn^{8+}

Strong emission features of Sn^{8+} are found between 14 and 15 nm, as shown in Fig. 2.2. Identified lines stem from $4p$–$4d$ and $4d$–$4f$ transitions [18]. Although more recent studies [38] have found that the level energies of the ground manifold from Ref. [18] in Sn^{8+}–Sn^{10+} may not be fully correct, the accuracy of the line determination in the EUV is sufficient for the current investigations. Configurations used in those [18] and the current Cowan calculations for the charge states Sn^{8+}–Sn^{10+} are of type $4d^{m-1}(5p+6p)+4d^{m-1}(4f+5f+6f)+4p^5(4d^{m+1}+4d^m5s)$. Scaling factors were estimated by extrapolation from Sn^{6+}, Sn^{7+}, and isoelectronic Ag ion spectra [107]. The results, shown in Fig. 2.2, are in agreement with our measurements. Emission features located near 20 nm belong to the $4d$–$5p$ transition array in Sn^{8+}–Sn^{10+} ions, as previously identified by Ohashi and coworkers [37] in their CXS work. No individual line assignments were made in that work. There are thousands of lines contributing to these features, thus making line identifications of specific transitions inaccessible, which is also true in the current work. However, the origin of the emission features can be well understood from Cowan code calculations.

Spectrum of Sn^{9+}

The $4p$–$4d$ and $4p$–$4f$ transitions of Sn^{9+} are located around 14 nm, as shown in Fig. 2.2, and line identifications are described in Ref. [18]. A comparison of the spectrum, as obtained by the matrix inversion technique, with the listed transitions of Ref. [18] show that the strongest peak at 14.17 nm cannot be satisfactorily explained. However, using instead Cowan calculations based on an extrapolation of scaling factors, similar to the case of Sn^{8+} (see above), enables obtaining a reasonable match with the experimental spectrum (see Fig. 2.2) including the $4d$–$5p$ transitions located between 16 and 19 nm.

Spectrum of Sn^{10+}

The $4p$–$4d$ and $4d$–$4f$ transitions in Sn^{10+} are found between 13 and 14 nm (Fig. 2.2) according to line identifications performed on this transition array in Ref. [18]. Transitions of the type $4d$–$5p$ are observed between 15 and 17 nm. The Cowan calculations (for details, see above) for the aforementioned transition arrays are in excellent agreement with the experimental data, as shown in Fig. 2.2.

Summary of EBIT spectra

Fig. 2.4 summarizes our findings of the emission characteristics of the $4d$–$4f$, $4p$–$4d$, $4d$–$5f$, $4d$–$6f$, and $4d$–$5p$ transitions of the charge states Sn^{5+}–Sn^{10+}. We note that the positions found for the $4d$–$4f$ and $4p$–$4d$, smoothly scaling with charge state, are in accordance with literature values. These configurations become more and more intertwined

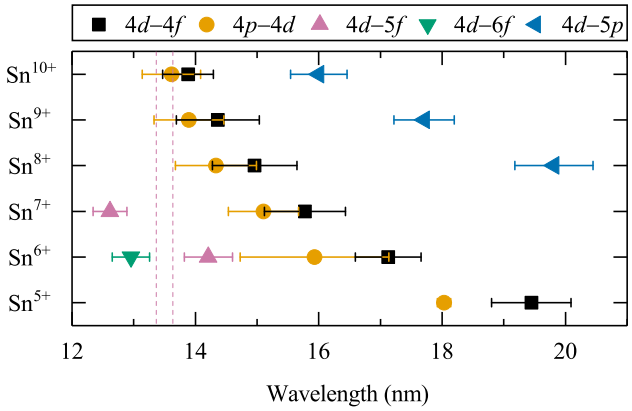

FIGURE 2.4: Wavelengths of spectral features of various transition arrays in Sn^{q+} (q = 5–10) as obtained from our Cowan code calculations. Symbol location represents the gA-weighted average wavelength of the transition array (first moment of the distribution according to UTA formalism [101, 102]), while the indicated width represents the standard deviation of the distribution (square root of the variance). Dashed vertical lines indicate a 2% bandwidth around 13.5 nm. Wavelengths and distribution widths shown in this figure are presented in Table 2.1.

with increasing charge state. We note that the $4d$–$5p$ transitions in Sn^{8+}–Sn^{10+} may be easily confused with $4d$–$4f$ or $4p$–$4d$ transitions of the lower charge states when diagnosing a tin plasma.

2.3.2 Diagnosing LPP spectra

Fig. 2.5 presents EUV emission spectra for various laser intensities from laser-produced plasmas using two target geometries: droplet and planar-solid. Plasma is produced from a Sn droplet target (top panel) and from a planar solid target (middle panel). Charge-state-resolved EBIT spectra of Sn^{5+}–Sn^{10+} ions are shown also (bottom panel).

In the top panel of Fig. 2.5, emission spectra from illumination of a Sn droplet target using laser intensities of 0.2, 0.6, 0.8, and 2.6×10^{11} W cm^{-2} are presented. The laser intensity was calculated as described in Ref. [23]. The dependence of the main feature near 13.5 nm wavelength on laser intensity has been discussed in detail elsewhere (see, e.g., Ref. [23, 32]) and the current discussion focuses on the wavelengths above 13.5 nm. For the lowest laser intensity, line features associated with the $4d$–$4f$ transition arrays in Sn^{5+}–Sn^{7+} particularly stand out. Their visibility strongly decreases with increasing laser intensity. Instead, line features associated with $4d$–$5p$ transitions of the more highly charged Sn^{8+} and Sn^{9+} ions become more prominent in this wavelength range with increasing laser intensity. The reduction of observed intensities of lines associated with the

lower charge states is most pronounced for Sn^{5+} and Sn^{6+}; lines of Sn^{7+} also reduce in relative amplitude but remain visible for all laser intensities shown. The expected evolution of the apparent charge state distribution with laser intensity is thus observed: higher laser intensity produce a hotter plasma with a higher average charge state. A more quantitative study would yield important insights regarding the population of charge states relevant for in-band emission at 13.5 nm wavelength, analogous and complementary to the work of Torretti *et al.* [15] for the shorter-wavelength emission features.

In the middle panel of Fig. 2.5, emission spectra are shown from a planar solid tin target for laser intensities of 0.3, 0.4, 0.8, and 3.0×10^{11} W cm^{-2}. This series of intensities is similar to those used in the droplet target case. The spectral differences between planar solid and droplet targets for wavelengths larger than 14 nm are striking. Generally, much more emission occurs at these longer wavelengths than in to the droplet target case. No emission line features of the low charge states Sn^{5+}–Sn^{7+} stand out. Instead, for all laser intensities, the $4d$–$5p$ transitions of the more highly charged Sn^{8+}–Sn^{10+} ions dominate this part of the spectrum. These emission features slowly decrease in relative amplitude as the laser intensity increases. Noteworthy are dips in the spectra observed at wavelengths where emission peaks appear for the droplet target.
More specifically, the strong dip around 15.6 nm seems to coincide with the expected location of the $4d$–$4f$ + $4p$–$4d$ transition array of Sn^{7+}. Similarly, two other particularly visible dips, located around 14.8 nm and 14.2 nm, line up with $4d$–$4f$ + $4p$–$4d$ transitions of Sn^{8+} and Sn^{9+}, respectively. The latter dip position also overlaps with the $4d$–$5f$ transition in Sn^{6+}. These dips can thus be explained by absorption by the plasma constituents.

Briefly, the spectral differences between the two target cases can be traced to geometrical arguments. The particular initial phase (liquid vs planar solid tin) has little bearing on the ensuing plasma given the energies involved. The geometry of the target affects the plasma emission in two aspects. First, size: the small, 18 μm-diameter droplet interacts mainly with the most intense part of the 80 μm laser pulse spot. In contrast, the large solid target interacts with the full beam spot. Second, dimensionality: the plasma expands and rarefies. The dimensionality of the rarefaction can be related to that of the target: a one-dimensional, linear expansion for the planar target and a quasi-three-dimensional expansion for the small droplet [30]. The rarefaction is much more rapid in the droplet case leading to less (self-)absorption of light [23]. Thus, the absorption features of the solid target spectra may be attributed to absorption in a rather dense but colder part of the plasma, which contains the relevant charge states that exhibit significant opacity [35], surrounding the main, hot and dense emission zone [34, 108]. For near-infrared drive lasers such as those operating at 1-μm wavelength, a spherical target appears to be better suited for obtaining a large fraction of the emitted EUV radiation in-band.

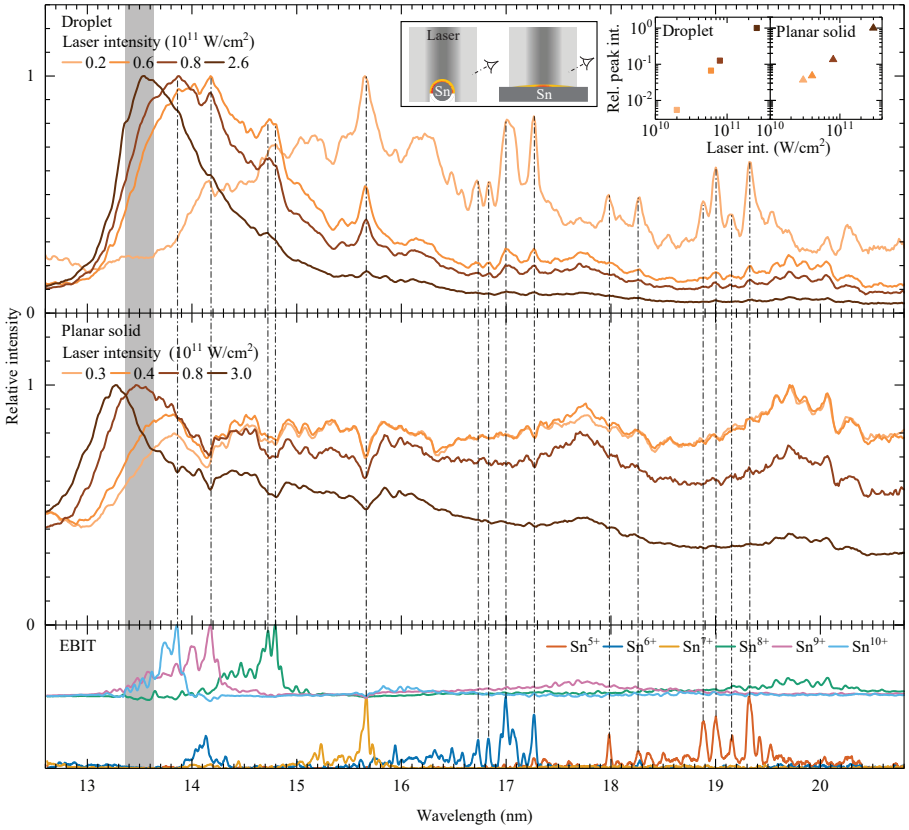

FIGURE 2.5: Top: normalized experimental LPP emission spectra in the extreme ultraviolet range for various Nd:YAG laser intensities, using a liquid droplet-based tin target with a droplet diameter of 18 µm and a FWHM laser beam spot of 80 µm. Middle: normalized experimental LPP emission spectra in the extreme ultraviolet region for various Nd:YAG laser intensities, using a planar solid tin target with a laser beam spot of 130 µm FWHM. Bottom: normalized charge-state-resolved spectra of Sn^{5+}–Sn^{10+} obtained from the EBIT measurements using the matrix inversion method (see text); the spectra of the three highest charge states are vertically offset for better visibility. The gray-shaded area shows the 2% bandwidth around 13.5 nm relevant for nanolithographic applications. The vertical dashed-dotted lines trace particular features from the EBIT in the LPP spectra. A schematic layout of both LPP experiments is presented as an inset in the top panel. The additional inset graph shows relative peak intensities as a function of laser intensity for both target cases.

TABLE 2.2: Cowan code Hartree-Fock with relativistic corrections (HFR) and least-squares-fitted (LSF) parameter values of the $4d^7nf$ (n = 4–6), and $4p^54d^9$ configurations in Sn^{6+}. All parameters are given in units of cm^{-1}. One-standard-deviation uncertainties are given in brackets. Fixed parameters are indicated with a superscripted "f". Parameters superscripted with r1, r2, and r3 are also fixed in the fitting procedure.

	$4d^74f$			$4d^75f$		$4d^76f$	
Parameter	HFR	FIT	FIT/HFR	HFR	Adopted	HFR	Adopted
E_{average} $(4d^7nf)$	535000	533917 (271)		694284	693283	779714	779714
$F^2(4d,4d)$	102377	85801 (200)	0.838	103411	86649	103642	86843
$F^4(4d,4d)$	68285	59966 (468)	0.878	69065	60650	69238	60802
$\alpha(4d)$		50^{f}		50			50
$\beta(4d)$		-540^{f}		-540			-540
$T^1(4d)$		-2^{f}		-2			-2
$\zeta(4d)$	3681	3799^{f}	1.032	3740	3861	3757	3877
$\zeta(nf)$	110	110^{f}	1	52	52	28	28
$F^2(4d,nf)$	65286	54159 (1254)	0.829^{r1}	22023	18257	10343	8574
$F^4(4d,nf)$	40129	33290 (771)	0.829^{r1}	12342	10232	5631	4669
$G^1(4d,nf)$	75280	60314 (331)	0.801^{r2}	20272	16238	8371	6705
$G^3(4d,nf)$	45662	36584 (201)	0.801^{r2}	13362	10703	5781	4630
$G^5(4d,nf)$	31866	25530 (140)	0.801^{r2}	9627	7711	4241	3397

	$4p^54d^9$		
Parameter	HFR	FIT	FIT/HFR
E_{average} $(4p^54d^9)$	616908	597881 (506)	0.969
$\zeta(4p)$	40711	44357 (539)	1.09
$\zeta(4d)$	3599	3714^{f}	1.032
$F^2(4d,4d)$	108221	102669 (3811)	0.949
$G^1(4p,4d)$	137494	107607 (1666)	0.783^{r3}
$G^3(4p,4d)$	85454	66898 (1035)	0.783^{r3}

2.4 Conclusion

Emission spectra from multiply-charged Sn^{5+}–Sn^{10+} ions are recorded from an EBIT and from LPP in the EUV range. In particular, features in the wavelength range between 12.6 and 20.8 nm are studied. A matrix inversion method is employed to produce charge-state-resolved spectra from the EBIT measurements. The Cowan code is used to identify the emission line features. Particular attention is given to the newly identified $4d$–$5f$ and $4d$–$6f$ transitions in Sn^{6+}. We have also identified a previously unreported $4p$–$4d$ transition in Sn^{5+}. The obtained spectroscopic information is employed to diagnose the Sn LPP produced from a liquid droplet and a planar solid Sn target. Emission features are identified and assigned to specific charge states using the EBIT data. For the planar solid Sn target, the $4d$–$5p$ transitions of Sn^{8+}–Sn^{10+} ions dominate the long-wavelength part of the EUV spectrum. Transitions of type $4d$–$4f$ + $4p$–$4d$ appear as self-absorption dips in the spectra. For the droplet target relevant for nanolithography, a more clear evolution of the charge-state distribution with laser intensity is observed: higher laser intensities produce a hotter plasma with a higher average charge state. Transitions of type $4d$–$4f$ + $4p$–$4d$ in Sn^{5+}–Sn^{7+} smoothly give way to $4d$–$5p$ type transitions in Sn^{8+}–Sn^{10+}. This study demonstrates the inherent potential of out-of-band emission to individually monitor several Sn charge states that strongly contribute to the unresolved transition array at 13.5 nm.

2.5 Acknowledgments

Part of this work has been carried out within the Advanced Research Center for Nanolithography, a public-private partnership of the University of Amsterdam, the Vrije Universiteit Amsterdam, the Netherlands Organisation for Scientific Research (NWO) and the semiconductor equipment manufacturer ASML and was financed by Toeslag voor Topconsortia voor Kennis en Innovatie from the Dutch Ministry of Economic Affairs. The transmission grating spectrometer was developed in the Industrial Focus Group XUV Optics at the University of Twente and supported by the FOM Valorisation Prize 2011 awarded to F. Bijkerk and NanoNextNL Valorization Grant awarded to M.B. in 2015. This project received funding from the European Research Council Starting Grant No. 802648 and is part of the VIDI research program with Project No. 15697, which is financed by NWO. Work by C.S. was supported by the Max-Planck-Gesellschaft and by the Deutsche Forschungsgemeinschaft Project No. 266229290. J.S. and O.O.V. thank the MPIK in Heidelberg for the hospitality during the measurement campaign.

3

Energy-level structure of Sn^{3+} ions

J. Scheers, A. Ryabtsev, A. Borschevsky, J. C. Berengut, K. Haris, R. Schupp, D. Kurilovich, F. Torretti, A. Bayerle, E. Eliav, W. Ubachs, O. O. Versolato, and R. Hoekstra

Physical Review A **98**, 062503 (2018)

Laser-produced Sn plasma sources are used to generate extreme ultraviolet light in state-of-the-art nanolithography. An ultraviolet and optical spectrum is measured from a droplet-based laser-produced Sn plasma, with a spectrograph covering the range 200–800 nm. This spectrum contains hundreds of spectral lines from lowly charged tin ions Sn^{1+}–Sn^{4+} of which a major fraction was hitherto unidentified. We present and identify a selected class of lines belonging to the quasi-one-electron, Ag-like ([Kr]$4d^{10}nl$ electronic configuration), Sn^{3+} ion, linking the optical lines to a specific charge state by means of a masking technique. These line identifications are made with iterative guidance from Cowan code calculations. Of the 53 lines attributed to Sn^{3+}, some 20 were identified from previously known energy levels, and 33 lines are used to determine previously unknown level energies of 13 electronic configurations, i.e., $7p$, $(7,8)d$, $(5,6)f$, (6–8)g, (6–8)h, $(7,8)i$. The consistency of the level energy determination is verified by the quantum-defect scaling procedure. The ionization limit of Sn^{3+} is confirmed and refined to 328 908.4 cm^{-1} with an uncertainty of 2.1 cm^{-1}. The relativistic Fock-space coupled cluster (FSCC) calculations of the measured level energies are generally in good agreement with experiment but fail to reproduce the anomalous behavior of the $5d\ ^2D$ and $nf\ ^2F$ terms. By combining the strengths of the FSCC calculations, Cowan code calculations, and configuration interaction many-body perturbation theory, this behavior is shown to arise from interactions with doubly excited configurations.

3.1 Introduction

Emission of light by neutral tin atoms and lowly charged tin ions, Sn I–Sn V, is abundant in a wide variety of plasmas, ranging from laser-produced extreme ultraviolet (EUV) light generating Sn plasma for nanolithography [9, 14], divertor plasma when using tin-containing materials in future thermonuclear fusion reactors [109–111], discharge plasma between tin whiskers causing short circuits [112], to astrophysical environments [113–121]. Spectroscopic investigations of these kinds of plasmas can help characterize plasma parameters [41–43, 122–125] such as ion and electron densities and temperatures by study of the observed line strengths and their shapes. However, spectroscopic information on the relevant charge states Sn^{3+} and Sn^{4+}, i.e., Sn IV and Sn V, is rather scarce, because of the poorly known electronic structure of these ions.

Sn^{3+}, with its ground electronic configuration [Kr]$4d^{10}\,5s$, belongs to the Ag-like isoelectronic sequence. Remarkably, only the lowest eight singly excited $4d^{10}\,nl$, the doubly excited $4d^9\,5s^2$ and three $4d^9\,5s\,5p$ levels in Sn^{3+} are tabulated in the National Institute of Standards and Technology (NIST) Atomic Spectra Database (ASD) [64]. Level energies originate from unpublished work by Shenstone [126], while wavelengths are given in another compilation by the National Bureau of Standards [127]. The assessment of energy levels by Shenstone is based on extended and revised work by Lang and others [128–131]. Since the early compilation [126] of almost 60 years ago, the only extension of the electronic energy-level structure of Sn IV stems from EUV spectroscopy by Ryabtsev and coworkers [132] in which they extend the ns series from $n = 8$ up to $n = 10$ and add the $7d\ ^2D$ term. A more extensive list of Sn IV lines is given in an otherwise unpublished master's thesis [133]. In other works, beam-foil techniques have been used to determine lifetimes [134–136]. Besides the singly excited levels, some doubly excited energy levels belonging to the $4d^9\,5s\,5p$ configuration are identified in laser- and vacuum-spark-produced tin plasmas [33, 36, 108, 132, 137, 138]. Theoretical level energies and transition probabilities [139, 140] have been calculated for Ag-like ions. The narrow, inverted fine structure of the $4f\ ^2F$ term in Ag-like Sn^{3+} has been addressed in detail by theory [139–143]. In spite of all these efforts, knowledge of the electronic structure of Sn IV is mostly limited to its lowest energy levels.

To obtain the electronic structure of Sn^{3+}, we have studied its line emission in the wavelength range of 200–800 nm. The optical lines belonging to Sn IV are identified among the hundreds of optical lines stemming from a laser-produced droplet-based Sn plasma, by taking spectra as a function of the laser intensity. The method to single out transitions belonging to ions in a specific charge state relies on the strongly changing ratio between line intensity and background emission from the plasma as a function of the laser intensity.

In the following we first introduce and detail a convenient method to obtain charge-state-resolved optical spectra from a laser-produced plasma. Of the more than 350 lines observed in the visible spectral range, 53 are identified as stemming from Sn^{3+}. Of these,

33 lines are new determinations. Thereafter, line identification is discussed. On the basis of these line identifications an extended level diagram for Sn^{3+} is constructed. The consistency of the highly excited levels is checked by quantum-defect scalings. In the final section, Fock-space coupled cluster (FSCC) and configuration interaction many-body perturbation theory (CI+MBPT) calculations are employed to explain the anomalous behavior of the $5d\ ^2D$ and $nf\ ^2F$ terms.

3.2 Experimental setup

An overview of the experimental setup is depicted in Fig. 3.1. A more detailed explanation is provided in Ref. [28]. The experimental laser-produced plasma source consists of a vacuum vessel (about 10^{-7} mbar) equipped with a droplet generator from which a 10-kHz stream of liquid tin microdroplets is ejected. The droplets have a diameter of about 45 μm. A 10-Hz pulsed Nd:YAG laser, operating at its fundamental wavelength of 1064 nm, is used to irradiate the droplets in order to generate a plasma. The laser energy is varied without changing the beam shape by using the combination of a half-wave plate ($\lambda/2$) and a thin-film polarizer (TFP), reflecting part of the light into a beamdump (BD). The laser beam is circularly polarized by a quarter-wave plate ($\lambda/4$); hereafter the beam is focused onto the droplet. This results in a Gaussian full width at half maximum (FWHM) beam size of 115 μm at the droplet position. The laser has a 10-ns FWHM pulse length. Light reflected by the droplet falling through a helium-neon (HeNe) laser sheet is detected by a photon-multiplier tube (PMT) used to trigger the laser.

The light emitted from the plasma is observed through a viewport perpendicular to the laser beam propagation and 30° above the horizontal plane. A biconvex lens images the plasma onto a quartz fiber that is used to guide the light to the spectrometer (Princeton Isoplane SCT 320). The entrance side of the fiber consists of 19 cores with a diameter of 200 μm in a hexagonal configuration, while at the exit side the cores are oriented in a linear configuration to efficiently guide light through the spectrometer slit. The spectrometer is laid out in a Czerny-Turner configuration with a focal length of 320 mm. The grating has 1200 lines per millimeter and is blazed at 500 nm, leading to a significantly reduced grating diffraction efficiency below 300 nm. A CCD camera (Princeton Pixis 2KBUV) optimized for the ultraviolet and visible regime recorded the diffracted light. By rotating the grating, thus changing the spectral detection range, the full spectral range from 200 to 800 nm is covered in steps of approximately 50 nm, overlapping by about 10 nm. From the shortest to the longest wavelength the linear dispersion decreases from 0.033 to 0.028 nm per pixel.

The wavelength axis is calibrated using neon-argon and mercury lamps. The FWHM line widths of the calibration lines are smaller than 0.1 nm. The total uncertainties of the mid positions of the Sn^{3+} lines are better than 0.01 nm over all observed laser energies and wavelengths. The emitted light is space- and time-integrated by summing the intensity

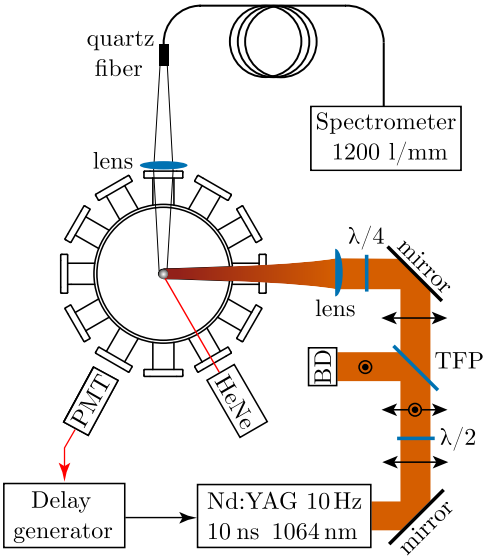

FIGURE 3.1: Schematic top view of the main components of the laser-produced plasma source from which the spectroscopic data were taken. For details see Section 3.2.

resulting from the various fiber cores and taking an integration time of 10 s, corresponding to 100 laser shots.

Measurements are performed with, and without, edge-pass filters to distinguish second-order lines from first-order ones. This enables filtering out the second-order lines appearing at wavelengths longer than 400 nm. Additionally, closely packed lines in the ultraviolet below 300 nm can be resolved in second order at a higher resolution. Weakly appearing lines at first order, due to the low grating response below 300 nm, are observed with a higher intensity at second order.

3.3 Charge state identification

We performed passive spectroscopy measurements on the laser-produced tin plasma for a series of laser energies ranging from 0.5 to 370 mJ. Fig. 3.2 shows example measurements over a selected wavelength range for three laser energies, where it is shown that the number of lines increases with laser energy. This is a signature of an increasing number of contributing charge states to the measured spectrum. A closer inspection indicates that indeed sets of lines appear with increasing laser energy that exhibit similar changes in intensity. As will be demonstrated below, each of these sets of lines can be singled

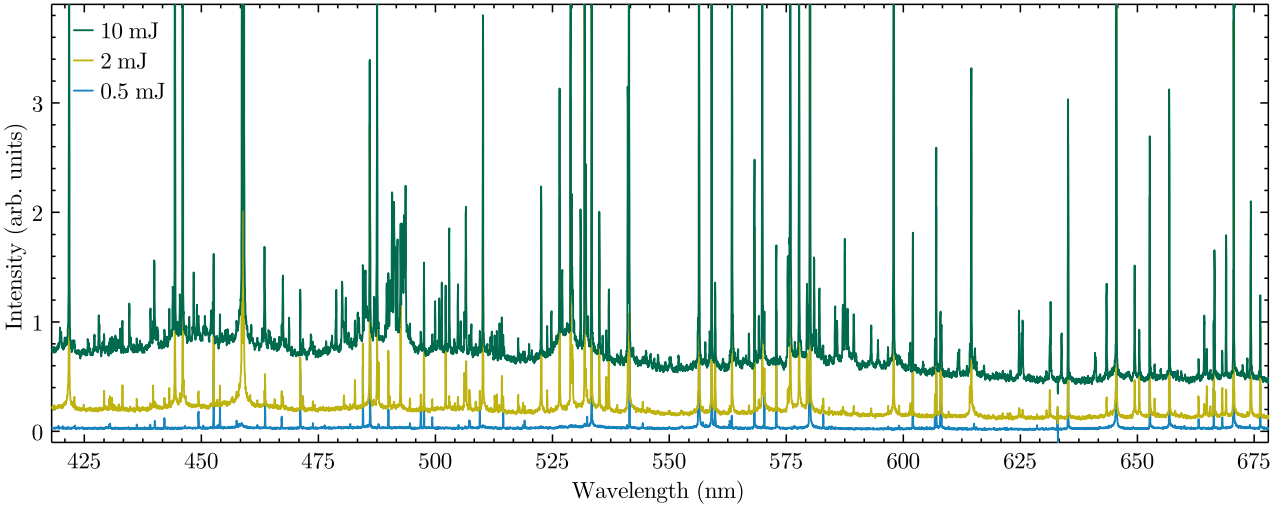

FIGURE 3.2: Experimentally obtained Sn^{q+} spectra for laser energies of 0.5 mJ (blue; lower), 2 mJ (yellow; middle), and 10 mJ (green; upper). The observable increase in the background level is due to increased continuum emission from the plasma at higher laser energies. Spectra shown are taken without spectral filters and, thus, include second-order contributions.

out by considering their intensities with respect to the continuum background, increasing strongly with the laser energy.

To illustrate the procedure we select a well-known line of each of the charge states Sn I–Sn V. These are the Sn I $5p^2\ {}^1S_0$–$5p6s\ {}^1P_1$ (λ=452.60 nm [144]), Sn II $5d\ {}^2D_{5/2}$–$4f\ {}^2F_{7/2}$ (λ=580.05 nm [145]) (the transition from the $4f\ {}^2F_{5/2}$ at 579.85 nm is also visible), Sn III $6s\ {}^1S_0$–$6p\ {}^1P_1$ (λ=522.64 nm [146]), Sn IV $6s\ {}^2S_{1/2}$–$6p\ {}^2P_{1/2}$ (λ=421.73 nm), and Sn V $6s\ {}^3D_3$–$6p\ {}^3F_4$ (λ=315.6 nm, based on level energies taken from Refs. [147, 148]). The scaled intensity is defined as $\frac{I_\lambda}{I_{\mathrm{bg}}} - 1$, with I_λ the line intensity and I_{bg} the (local value of the) continuum background level. For direct comparison, the scaled intensity of each individual line is normalized to its maximum value, as shown in Fig. 3.3.

In Fig. 3.3, it is shown that for the lowest charge states Sn I and Sn II the normalized, scaled intensity maximizes for the lowest laser energy of 0.5 mJ, while for the highest observed charge state Sn V a laser energy of 10 mJ is optimal. Sn IV, the ion of interest here, maximizes at 2 mJ. This demonstrates that the contributions of higher charge states to the spectrum increase with increasing laser energy. Preliminary nanosecond time-resolved spectroscopic measurements revealed that spectral line emission is mostly observed in the late-time evolution of the plasma. Traces of line broadening are observed in the time-integrated spectra presented in this work, e.g., the Sn IV line shape in the 2-mJ spectrum. Analysis of line-broadening mechanisms and the time evolution of these plasmas is left for future work, as they do not influence our line identifications and are outside the scope of this paper.

Fig. 3.4 quantifies the dependence of the scaled intensities for spectral lines belonging to tin ions in charge states 0, 1, 2, 3, and 4+ produced in the Sn LPP. This energy dependence of each charge state enables to make our assignments of unknown lines to specific charge states. In this way 53 lines are assigned to Sn IV.

For our present experiments on tin ions we checked carefully the dependence of the intensities of all well-known tin lines on laser energy. For each of the charge states the intensities of their well-known lines follow with some scatter the dependencies shown in Fig. 3.4. However, for adjacent charge states and weak lines with considerable scatter and which do not show up over the full laser energy range there is a risk of ascribing such a weak line to the incorrect charge state. Solely based on the laser-energy dependence there were about five weaker lines that could either be Sn IV or Sn V. Even those lines could be attributed to either Sn IV or Sn V using the spectral identification procedure described in the next section, Section 3.4.

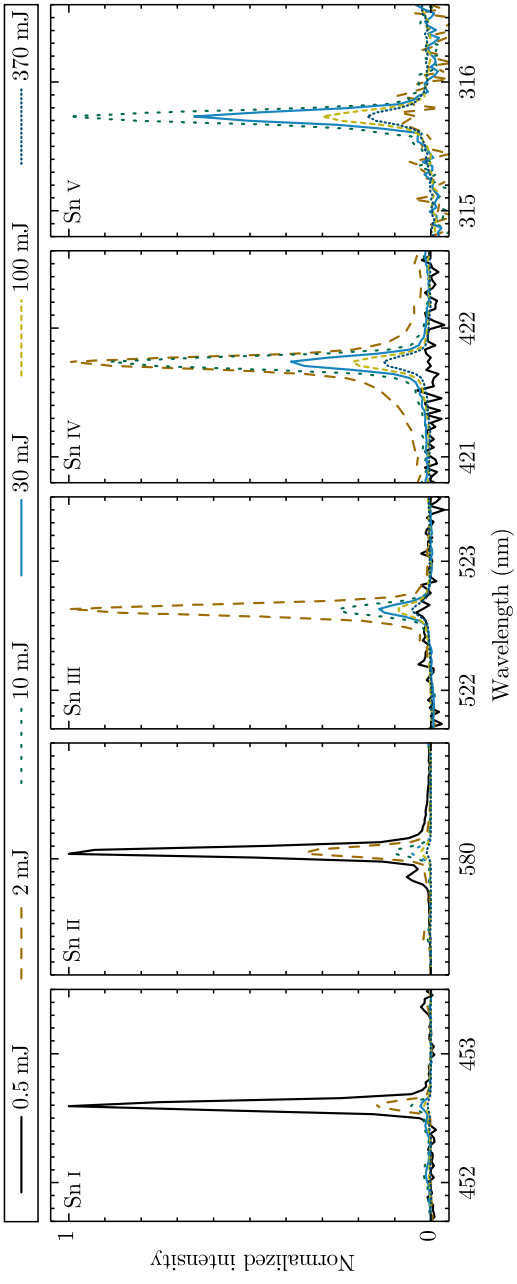

FIGURE 3.3: Spectral intensity scaling as a function of wavelength (vacuum; in nm) for varying laser energies. Here, the intensity is normalized to their (local) continuum background level, and unity is subsequently subtracted. The specific transitions shown are described in the text.

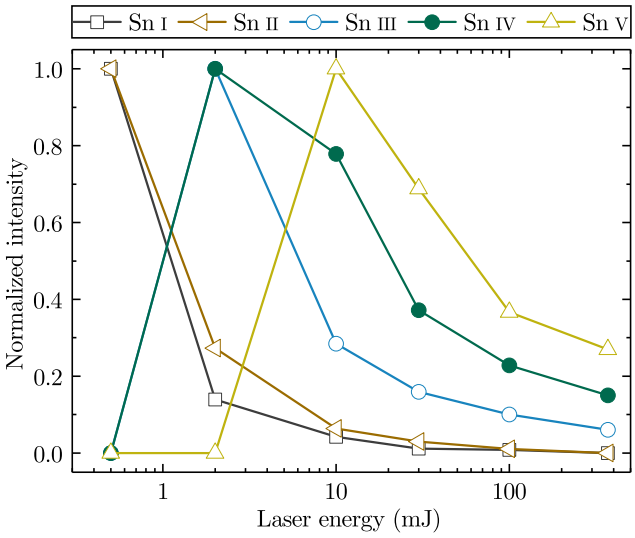

FIGURE 3.4: Normalized scaled intensities of Sn I–Sn V lines as a function of laser energy. The same lines as presented in Fig. 3.3 are used. Other Sn I–Sn V lines show a similar dependence on laser energy.

3.4 Line identification procedure

Of the 53 lines in the ultraviolet and optical spectral range attributed to Sn IV, 20 are readily identified as transitions between energy levels known from literature [126], and match well within mutual experimental uncertainties with the line positions given in Ref. [133]. These 20 lines are presented in Table 3.1 along with their connecting upper and lower energy levels.

Having identified 20 lines using known energy levels, we proceed with the identification of the other lines ascribed to Sn IV. Unique identification of the observed lines requires an accuracy of the level energies of better than 10^{-3}, which is challenging for atomic theories. Therefore, an iterative procedure is used to identify the unknown lines. We use the Cowan code to calculate the electronic structure and transitions, and adjust its parameters to match perfectly the known lines in the spectrum. In this way, energy levels just above the known ones can be obtained with sufficient accuracy to identify the next set of lines. This procedure can be repeated to identify all lines. Furthermore, quantum defect theory [149] is used to check the consistency of level energies for each l series.

3.4.1 Cowan procedure

The Cowan code [58], one of the most widely applied electronic structure codes, is used to calculate the energies of yet unestablished Sn IV levels. The Cowan code produces radial wave functions using a quasirelativistic Hartree-Fock method. The electrostatic single-configuration radial integrals F_k and G_k (Slater integrals), configuration interaction, Coulomb radial integrals, and spin-orbit parameters are calculated from the obtained wave functions. Subsequently, level energies and intermediate coupling eigenvectors are extracted. Furthermore, values for the transition probabilities and wavelengths are obtained.

The values of the electrostatic integrals are scaled by a factor between 0.7 and 0.85 as well as the scaling of spin-orbit parameters to optimally fit the thus far understood experimental spectrum. The outcome of this parameter scaling procedure yields a useful interpretation of the experimental spectrum. This enables predictions for lines between not yet experimentally established energy levels. These predictions include their relative strength expressed as the gA factor: the Einstein coefficient A multiplied with the statistical weight g of the upper state. Due to the one-electron nature of the system, the number of allowed transitions between two terms is only three (or two if a ^2S term is involved). However, we might observe only two lines since transitions between equal angular momenta typically have a small gA factor. Experimental lines that lie close to a predicted transition and have relative line strengths similar to those determined on basis of the aforementioned gA factors are thus assigned to a specific transition. This provides an enlarged set of levels that can be used to fine-tune the calculations in the next step.

TABLE 3.1: Vacuum wavelengths (in nm) of Sn IV lines between levels previously known. The wavelengths determined in this work are compared with literature values taken from an otherwise unpublished Master's thesis [133]. The upper and lower energy levels indicating the transition represent the nl one-electron orbital outside the [Kr]$4d^{10}$ core configuration. The $5s^2$ indicates the doubly excited $4d^9\,5s^2$ configuration. The wavelengths determined in this work are averaged centroid positions of Gaussian fits in spectra taken at different laser energies. The intensity I represents the area-under-the-curve of this line in the 30 mJ spectrum. gA factors from the upper level result from analysis with the Cowan code.

λ (nm)				lower		upper	
this work	literature	I (arb. units)	gA (10^8 s^{-1})	nl	J	nl	J
208.23	208.224	25	130.2	$4f$	7/2	$5g$	9/2
208.49	208.485	20	100.4	$4f$	5/2	$5g$	7/2
222.14	222.156	289	53.8	$5d$	3/2	$4f$	5/2
222.66	222.680	1	3.4	$5d$	5/2	$4f$	5/2
222.96	222.980	34	68.5	$5d$	5/2	$4f$	7/2
243.75	243.757	35	6.6	$5s^2$	5/2	$4f$	7/2
251.47	251.466	22	6.0	$6p$	1/2	$7s$	1/2
266.05	266.054	48	10.1	$6p$	3/2	$7s$	1/2
270.68	270.667	154	27.5	$6p$	1/2	$6d$	3/2
284.91	284.922	351	42.2	$6p$	3/2	$6d$	5/2
287.64	287.633	38	4.6	$6p$	3/2	$6d$	3/2
287.96	287.961	32	1.5	$5d$	3/2	$6p$	3/2
288.85	288.840	219	11.2	$5d$	5/2	$6p$	3/2
307.26	307.247	251	6.0	$5d$	3/2	$6p$	1/2
324.71	324.700	166	1.6	$5s^2$	5/2	$6p$	3/2
386.23	386.232	1 063	9.2	$6s$	1/2	$6p$	3/2
402.08	402.071	289	4.5	$4f$	7/2	$6d$	5/2
403.03	403.076	30	0.2	$4f$	5/2	$6d$	5/2
408.52	408.520	219	3.0	$4f$	5/2	$6d$	3/2
421.73	421.735	677	3.5	$6s$	1/2	$6p$	1/2

3.4.2 Quantum defect

The energy levels of quasi-one-electron systems approach a hydrogenlike level structure, especially for high principal and angular quantum numbers. For such systems the energy levels which are shifted towards slightly higher binding energies can be well described by introducing the so-called quantum defect δ_l as a correction to the Bohr formula. The position of the energy level E_{nl} (relative to the ionization limit) is defined by [149]

$$E_{nl} = -R\frac{Z_c^2}{(n-\delta_l)^2}, \tag{3.1}$$

with Z_c the net charge state of the core ($Z_c = 4$ for Sn^{3+}) and n the principal quantum number. R relates to the Rydberg constant R_∞ as $R = R_\infty(1+\frac{m_e}{M})^{-1}$, with m_e and M the electronic and nuclear mass, respectively. Following the review by Edlén [149], the quantum defect can be written as a Taylor expansion in $1/n^{*2}$ with n^* being the apparent principal quantum number $n^* = n - \delta_l$, with quantum defect δ_l,

$$\delta_l = a\left(\frac{1}{n^{*2}}\right) + b\left(\frac{1}{n^{*2}}\right)^2 + \ldots \tag{3.2}$$

The quantum defect becomes smaller with increasing angular momentum. For high-n values the first term dominates and the minute change of δ_l as a function of $1/n^{*2}$ becomes linear. Additionally, it is well-established that a is positive for $l \leq l_{\text{core}}$, while a is negative for $l > l_{\text{core}}$ [149]. For Sn^{3+} with its $4d^{10}$ core, $l_{\text{core}} = 2$.

3.5 Results and discussion

Using the iterative guidance from the Cowan code as described above, we assign the newly found lines. The new Sn IV line assignments are summarized in Table 3.2. The level energies of excited states are determined with respect to the 6*s*, which is used as an anchor level considering that transitions to the 5*s* ground state are outside our detection region. The optimization of level energies is performed using Kramida's code LOPT [150], and the final results are presented in Table 3.3.

The consistency of the energies of levels within a specific l series is verified by determining the respective quantum defects. Quantum defects are calculated using Eq. (3.1) with the level energies found relative to the ionization limit. Therefore an accurate value of this limit is needed.

The ionization limit of 328 550(300) cm^{-1}, tabulated in the NIST ASD [64], is based on the determination of the series limit of the *ns* levels (n = 5–7). Ryabtsev *et al.* [132] extended this *ns* series with 8*s*, 9*s*, and 10*s*. Using the extended *ns* series they were able to refine the ionization limit to 328 910(5) cm^{-1}. The ionization limit can be further improved by taking additional levels into account. Configurations which are prone

TABLE 3.2: Assignments and vacuum wavelengths (in nm) of UV and visible transitions of Sn IV identified in this work. The upper and lower energy levels indicating the transition represent the *nl* one-electron orbital outside the [Kr]$4d^{10}$ core configuration. Wavelengths determined in this work are averaged centroid positions of Gaussian fits in spectra taken at different laser energies. The intensity *I* represents the area under the curve of this line in the 30-mJ spectrum [in arbitrary (arb.) units]. *gA* factors from the upper level result from analysis with the Cowan code. The fine structure for several high-*l* states could not be resolved experimentally, therefore no individual angular momenta are listed and the reported *gA* is the summed value of the three possible transitions.

			lower		upper	
λ (nm)	*I* (arb. units)	*gA* (10^8 s^{-1})	*nl*	*J*	*nl*	*J*
202.08	1	10.5	5*f*	7/2	8*g*	9/2
203.36	2	8.6	5*f*	5/2	8*g*	7/2
231.72	2	14.4	5*g*		8*h*	
242.55	3	0.3	6*d*	3/2	6*f*	5/2
245.15	1	0.5	6*d*	5/2	6*f*	7/2
273.75	3	2.2	7*p*	1/2	8*d*	3/2
279.91	8	3.8	7*p*	3/2	8*d*	5/2
287.82	48	30.4	5*g*		7*h*	
357.01	204	24.6	5*f*	7/2	6*g*	9/2
360.99	233	20.2	5*f*	5/2	6*g*	7/2
393.41	27	5.7	6*f*	7/2	8*g*	9/2
395.08	35	4.4	6*f*	5/2	8*g*	7/2
459.04	2 518	93.7	5*g*		6*h*	
463.49	202	15.1	6*g*		8*h*	
467.41	107	14.7	6*h*		8*i*	
504.82	90	2.0	7*p*	1/2	8*s*	1/2
529.12	40	3.5	7*p*	3/2	8*s*	1/2
541.12	366	7.9	7*p*	1/2	7*d*	3/2
563.38	662	12.4	7*p*	3/2	7*d*	5/2
563.60	60	0.7	5*g*	7/2	6*f*	5/2
567.00	42	0.9	5*g*	9/2	6*f*	7/2
569.13	68	1.3	7*p*	3/2	7*d*	3/2
575.85	881	10.0	6*d*	3/2	5*f*	5/2
589.40	71	6.9	6*f*	7/2	7*g*	9/2
593.13	368	5.3	6*f*	5/2	7*g*	7/2
597.93	940	12.5	6*d*	5/2	5*f*	7/2
643.43	154	3.3	5*f*	7/2	7*d*	5/2
664.32	103	2.3	5*f*	5/2	7*d*	3/2
673.51	36	0.5	6*d*	3/2	7*p*	3/2
688.89	212	3.8	6*d*	5/2	7*p*	3/2
717.44	98	1.8	6*d*	3/2	7*p*	1/2
759.65	316	49.6	6*g*		7*h*	
769.75	388	49.6	6*h*		7*i*	

to shifting of the level energies by configuration interaction effects (np, nd, and nf, further described in Section 3.5.3) are however unsuitable for determining the series limit. Therefore we only use the ng, nh and ni configurations to refine the ionization limit. The results from analysis with the POLAR code [151] is 328 908.4 cm^{-1} with a statistical error of 0.3 cm^{-1}. Combining this in quadrature with the uncertainty of 6s anchor level, we arrive at a total uncertainty of 2.1 cm^{-1}. Fig. 3.5 presents the quantum defects of the Sn IV levels as a function of $1/n^{*2}$. Overall, a smooth dependence is found for all angular quantum numbers from $l = 0$ (s) up to $l = 6$ (i), underpinning the consistency of our identifications.

For the discussion of details of the line assignments and energy levels we consider separately levels for which the valence electron does or does not penetrate the electronic core, i.e., levels with $l \leq l_{\mathrm{core}}$ and $l > l_{\mathrm{core}}$, respectively. For Sn^{3+} with its $4d^{10}$ core, $l_{\mathrm{core}} = 2$. Anomalous effects on the fine structure splitting of the 5d and nf configurations are discussed and explained separately. Finally, Fig. 3.6 depicts the extended level diagram of Sn IV as a concise summary of our results.

3.5.1 $l \leq l_{\mathrm{core}}$ configurations

The 5s, 6s, and 7s levels are included in Moore's tables [126]. The excitation energies of the 8s, 9s, and, 10s levels were determined in EUV spectroscopy experiments by Ryabtsev *et al.* [132] in which transitions to the $5p\ ^2P_{1/2,3/2}$ terms were measured. The $5p\ ^2P_{1/2,3/2}$ terms can be populated from the nd series; this nd series is known up to $n = 7$. The highest known np configuration so far was 6p. All transitions in the optical spectral range (Table 3.2) between both ns and nd and 6p agree with the literature excitation energies of the respective levels.

The $7p\ ^2P_{1/2,3/2}$ levels are found by considering all possible transitions from the $7d\ ^2D_{3/2,5/2}$ and $8s\ ^2S_{1/2}$ to the $7p\ ^2P_{1/2,3/2}$ levels. These levels can decay via emission in the visible to $6d\ ^2D_{3/2,5/2}$. The excitation energies of the 7p configuration are established using seven transitions to three surrounding energy terms, providing a reliable assessment of the $7p\ ^2P_{1/2,3/2}$ level energies. For the $7d\ ^2D_{5/2}$ good agreement with Ref. [132] is found, while for the $7d\ ^2D_{3/2}$ level a difference of about 30 cm^{-1} is observed. The 8d is successively determined using two transitions to the 7p, where the transition between equal angular momenta is likely too weak to be observed in our spectra.

The quantum defects for $l \leq l_{\mathrm{core}}$ are shown in Fig. 3.5, calculated using the refined ionization limit. All data points exhibit a linear behavior, with only the lowest 5l configurations slightly deviating, reflecting a signature of the small quadratic term in Eq. (3.2). The most remarkable observation is the almost-equal quantum defects of the $5d\ ^2D_{3/2,5/2}$ levels, indicative of an anomalously small fine-structure interval of the $5d\ ^2D$ term. This anomaly is further discussed in section 3.5.3.

TABLE 3.3: (Caption on following page).

		$E_{\text{experiment}}$ (cm^{-1})		E_{theory} (cm^{-1})				
nl	*J*	this work	literature	FSCC	ΔE_{Breit}	ΔE_{QED}	Total	RMBPT [139]
$5p$	1/2		69 563.9 [126]	69 850	62	-171	69 741	69 265
	3/2		76 072.3 [126]	76 447	-26	-165	76 256	75 736
$5d$	3/2	165 304(1)	165 304.7 [126]	165 974	-123	-205	165 646	164 538
	5/2	165 409(1)	165 410.8 [126]	166 731	-145	-204	166 382	165 283
$4d^9\,5s^2$	5/2	169 233.6(8)	169 233.6 [126]					
	3/2		177 889.0 [126]					
$6s$	1/2	174 138.8(4)	174 138.8 [126]	174 478	-99	-143	174 236	
$6p$	1/2	197 850.6(6)	197 850.9 [126]	198 292	-74	-193	198 025	
	3/2	200 030.1(4)	200 030.8 [126]	200 512	-103	-193	200 216	
$4f$	7/2	210 258.2(6)	210 257.7 [126]	210 912	-158	-200	210 554	209 418
	5/2	210 317.9(7)	210 318.2 [126]	210 983	-156	-200	210 627	209 494
$6d$	3/2	234 797.0(1)	234 795.7 [126]	235 509	-134	-203	235 171	
	5/2	235 128.7(2)	235 127.7 [126]	235 842	-144	-201	235 497	
$7s$	1/2	237 617(1)	237 615.7 [126]	238 219	-123	-175	237 920	
$7p$	1/2	248 735.4(2)		249 402	-110	-197	249 094	
	3/2	249 644.8(1)		250 454	-124	-97	250 233	
$5f$	7/2	251 853.0(2)		252 984	-157	-201	252 626	250 981
	5/2	252 162.6(2)		253 023	-155	-202	252 666	251 025
$5g$	7/2	258 283.2(3)	258 282.3 [126]	258 782	-143	-201	258 439	256 868
	9/2	258 283.2(3)	258 282.7 [126]	258 782	-143	-201	258 439	256 872
$7d$	3/2	267 215.5(2)	267 247.6 [132]	267 815	-138	-202	267 475	
	5/2	267 394.7(2)	267 395.7 [132]	267 993	-143	-203	267 647	
$8s$	1/2	268 544.3(3)	268 544 [132]	269 193	-132	-166	268 895	
$6f$	7/2	275 919.8(3)		276 430	-153	-201	276 076	
	5/2	276 026.2(3)		276 450	-152	-201	276 097	
$6g$	9/2	279 863.6(2)		280 580	-143	-202	280 235	
	7/2	279 863.6(2)		280 581	-143	-201	280 237	
$6h$		280 067.8(7)						
$8d$	3/2	285 265(1)		285 834	-140	-197	285 497	
	5/2	285 370(1)		285 937	-143	-197	285 597	
$9s$	1/2		286 013 [132]					
$7g$		292 886.0(3)						
$7h$		293 027.6(3)						
$7i$		293 059.0(2)						
$10s$	1/2		296 844 [132]					
$8g$		301 338.2(6)						
$8h$		301 439.2(7)						
$8i$		301 462.3(7)						
IP		328 908.4(3)	328 550 [126]	329 343	-143	-201	328 999	327 453
			328 910 [132]					

TABLE 3.4: (Table on previous page) Energy levels of Sn^{3+}, with its ground state [Kr]$4d^{10}\,5s$. The experimental values obtained in this work are presented, next to the known values from the literature given in Refs. [126] and [132]. Experimental level energies of excited states are calculated with respect to the 6*s* anchor level and are the results of analysis with the LOPT code. The statistical uncertainty is presented in parentheses. The "Total" column lists the sums of FSCC calculations including Breit interaction and QED effects. As a comparison to theoretical values, relativistic many-body perturbation theory (RMBPT) calculations obtained from Ref. [139] are listed, while other known fine-structure splittings are reported in Table 3.5. The fine-structure splittings of several high-*nl* levels are smaller than $0.5\,\mathrm{cm}^{-1}$ and not resolved experimentally. In these cases, the value of the angular momentum is omitted. The ionization potential (IP) is presented at the bottom.

3.5.2 $l > l_{\mathrm{core}}$ configurations

Of the high-*l* configurations, i.e., nf, ng, nh, and ni, only the level energies of the $4f\ ^2F$ and $5g\ ^2G$ terms were known thus far. Our measurements confirm the small inverted fine-structure splitting of approximately $60\,\mathrm{cm}^{-1}$ of the $4f\ ^2F$ term and of about $0.5\,\mathrm{cm}^{-1}$ of the $5g\ ^2G$ by direct comparison of the $\Delta J = 0$ and $\Delta J = -1$ transitions. The $4f\ ^2F$ and $5g\ ^2G$ terms form the main basis on which the excitation energies of the high-*l* configurations are determined. Fine-structure splittings of the $ng\ ^2G$ ($n \geq 6$), $nh\ ^2H$, and $ni\ ^2I$ terms are too small to be determined, implying that their fine-structure splitting is less than $0.5\,\mathrm{cm}^{-1}$. The fine structure splittings of the nf terms are presented in Table 3.5 and will be discussed in detail in Sec 3.5.3.

The first level of the *nh* series, 6*h*, is found by assigning the strong transition from this level to 5*g*. The 6*h* is the lower level of the transitions determining the 7*i* and 8*i*. The 7*h* and 8*h* are found by transitions to the 6*g*, which is based on the transition to the $5f\ ^2$F. The $ng\ ^2$G ($n \geq 7$) are determined from their transitions to the $5f\ ^2F$ and $6f\ ^2F$ terms. The $5f$ and $6f$ terms are defined by transitions to their lower-lying $nd\ ^2D$ counterparts.

The relative values of the quantum defects for the *ng*, *nh*, and *ni* series are in good agreement with the *nl* scaling laws for $l > l_{\mathrm{core}}$ as presented by Edlén [149]. The quantum defects for the nf series are about a factor of 3 to 4 larger than expected from these scaling laws. In addition, relatively large fine-structure splittings are observed for the $5f\ ^2F$ and $6f\ ^2F$ terms. Both effects may be a signature of an enhanced interaction with core-electron configurations.

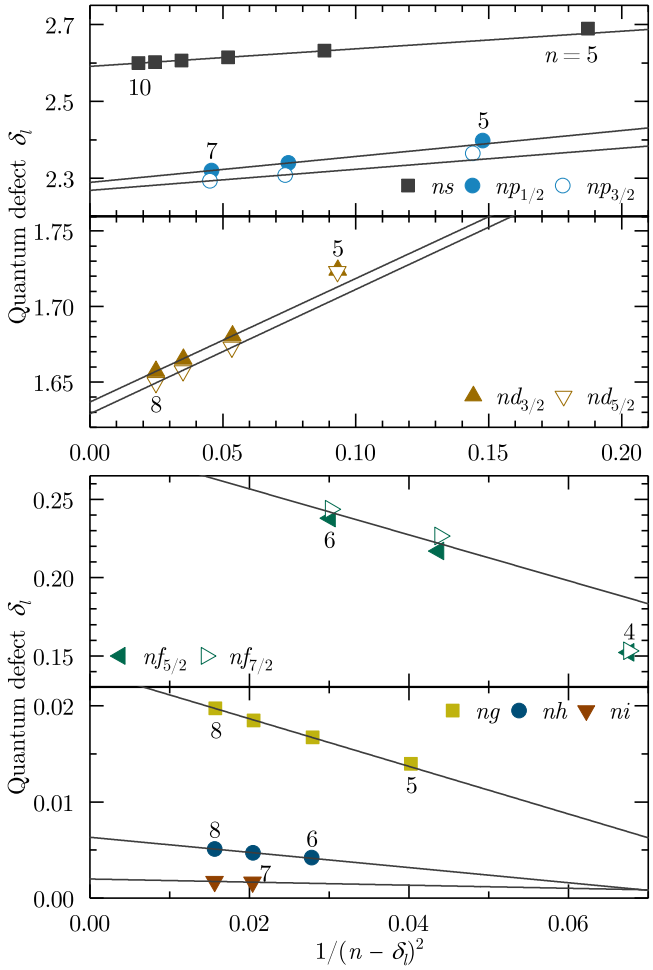

FIGURE 3.5: Quantum defect values as a function of $1/n^{*2}$ of the Sn IV energy levels, for $l \leq l_{\text{core}}$ (upper graph) and $l > l_{\text{core}}$ (lower graph). The quantum defects are calculated using Eq. (3.1) and the refined ionization limit of 328 908.4 cm^{-1}. The black lines are linear fits of the data points where the lowest level is excluded (except for the *ni* configuration).

3.5.3 Anomalous fine-structure effects in the $5d\,^2D$ and $nf\,^2F$ terms

Table 3.5 summarizes experimental and theoretical fine-structure intervals in Sn IV. We have performed Fock-space coupled cluster and configuration interaction many-body perturbation theory in order to address the aforementioned anomalous values of the fine-structure intervals in the $5d\,^2D$ and $nf\,^2F$ terms.

The FSCC calculations of the transition energies were performed within the framework of the projected Dirac-Coulomb-Breit (DCB) Hamiltonian [152],

$$H_{DCB} = \sum_i h_D(i) + \sum_{i<j} (1/r_{ij} + B_{ij}). \tag{3.3}$$

Here, h_D is the one electron Dirac Hamiltonian,

$$h_D(i) = c\boldsymbol{\alpha}_i \cdot \mathbf{p}_i + c^2\beta_i + V_{nuc}(i), \tag{3.4}$$

where $\boldsymbol{\alpha}$ and β are the four-dimensional Dirac matrices. The nuclear potential $V_{nuc}(i)$ takes into account the finite size of the nucleus, modeled by a uniformly charged sphere [153]. The two-electron term includes the nonrelativistic electron repulsion and the frequency-independent Breit operator,

$$B_{ij} = -\frac{1}{2r_{ij}}[\boldsymbol{\alpha}_i \cdot \boldsymbol{\alpha}_j + (\boldsymbol{\alpha}_i \cdot \mathbf{r}_{ij})(\boldsymbol{\alpha}_j \cdot \mathbf{r}_{ij})/r_{ij}^2], \tag{3.5}$$

and is correct to second order in the fine-structure constant α.

The calculations of the transition energies of Sn^{3+} start from the closed-shell reference $[Kr]4d^{10}$ configuration of Sn^{4+}. After the first stage of the calculation, consisting of solving the relativistic Hartree-Fock equations and correlating the closed-shell reference state, a single electron was added to reach the desired Sn^{3+} state. A large model space was used in this calculation, comprising $10\,s$, $8\,p$, $6\,d$, $6\,f$, $4\,g$, $3\,h$, and $2\,i$ orbitals in order to obtain a large number of excitation energies and to reach optimal accuracy. The intermediate Hamiltonian method was employed to facilitate convergence [154].

The uncontracted universal basis set [155] was used, consisting of even-tempered Gaussian-type orbitals, with exponents given by

$$\begin{aligned} \xi_n &= \gamma\delta^{(n-1)}, \quad \gamma = 106\,111\,395.371\,615, \\ \delta &= 0.486\,752\,256\,286. \end{aligned} \tag{3.6}$$

The basis set was composed of $37\,s$, $31\,p$, $26\,d$, $21\,f$, $16\,g$, $11\,h$, and $6\,i$ functions; the convergence of the obtained transition energies with respect to the size of the basis set was verified. All the electrons were correlated.

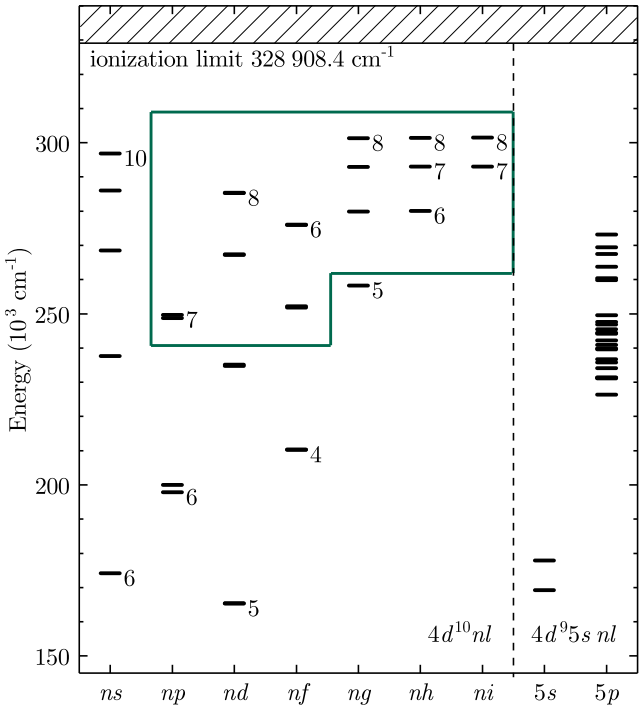

FIGURE 3.6: Level diagram of Sn^{3+}, drawn from 150 000 cm^{-1} to the ionization limit at 328 908.4 cm^{-1}. The ground state $5s$, the $5p\ ^2P$ term, and multiply-excited configurations lying near the ionization limit are omitted as transitions to these levels occur outside the detection range of this study. The levels determined by this study are shown in the boxed area. The other levels are based on Refs. [126, 132].

The FSCC calculations were performed using the Tel-Aviv Relativistic Atomic FSCC code (TRAFS-3C) [156]. To account for the QED corrections to the transition energies we applied the model Lamb shift operator (MLSO) of Shabaev and co-workers [157] to the atomic no-virtual-pair, many-body DCB Hamiltonian as implemented in the QEDMOD program. Our implementation of the MLSO formalism into the Tel Aviv atomic computational package allows us to obtain the vacuum polarization and self-energy contributions beyond the usual mean-field level, namely, at the DCB-FSCCSD level.

The FSCC results are compared to the experimental level energies and several results from previous theoretical work in Table 3.3 and are overall in good agreement. Typical differences from experiment are about 100 to 300 cm^{-1} which is on the 10^{-3} level of the calculated excitation energies. Concerning the measured anomalous fine-structure intervals of the $5d\ ^2D$ and $5f\ ^2F$ and $6f\ ^2F$ terms, presented in Table 3.5, the apparent narrowing of the fine-structure interval of the $5d\ ^2D$ term and the widening of the $5f, 6f\ ^2F$ term intervals are not reproduced by the FSCC calculations. The FSCC intervals are similar to those presented in earlier theoretical investigations [139–143].

For the $5d\ ^2D$ term the fine-structure interval is measured at 107 cm^{-1}, while all theoretical results are higher by a factor of approximately 7 (see Table 3.5). Upon inspecting the level diagram (Fig. 3.6) one notes that the $5d\ ^2D$ term might suffer from configuration interaction of the doubly excited $4d^9\,5s^2$ levels.

To quantify the strength of the configuration interaction we employ configuration interaction many-body perturbation theory (CI+MBPT) calculations using the AMBiT code. Details of the AMBiT code can be found in Refs. [61, 87, 88, 158]. To begin our discussion of the AMBiT treatment of the problem, first consider the $5d\ ^2D_{5/2}$ and $4d^9\,5s^2\ ^2D_{5/2}$ levels as a two-level system. In the absence of interaction between them, they have theoretical energies ε_1 and ε_2, respectively. ε_1 is, to a good approximation, the FSCC value of the $5d\ ^2D_{5/2}$ level, since in that calculation the one-hole two-particle $4d^9\,5s^2\ ^2D_{5/2}$ level is not explicitly included. If we now add an interaction V, then the states mix and the levels repel each other.

The Hamiltonian of this two-level system is

$$H = \begin{pmatrix} \varepsilon_1 & V \\ V & \varepsilon_2 \end{pmatrix}.$$

Writing $\Delta\varepsilon = \varepsilon_2 - \varepsilon_1 > 0$, the $5d\ ^2\mathrm{D}_{5/2}$ level shifts down by an amount

$$\delta = \frac{\Delta E - \Delta\varepsilon}{2} = \frac{\Delta\varepsilon}{2}\left(\sqrt{1+\frac{4V^2}{\Delta\varepsilon^2}} - 1\right) = b^2\Delta E, \tag{3.7}$$

where $\Delta E = E_2 - E_1$ is the difference between the eigenvalues of H and b is the smaller component of the normalized eigenvector $(a,b)^\intercal$.

Using AMBiT, we calculate theoretical values for the parameters ΔE_{th} and b, from which we can obtain the interaction $V = -ab\Delta E_{\mathrm{th}}$. However, the values of ΔE_{th} and b are

TABLE 3.5: Comparison of fine structure splittings in np, nd, and nf configurations of Sn IV. Experimental values stem from either a direct comparison of $\Delta J = 0$ and $\Delta J = -1$ transitions or indirectly from the optimized level structure. The latter are labeled by an asterisk. The upper part of the Table contains results published in this work, the lower part shows results obtained from Refs. [126, 139–143].

	fine structure splitting (cm^{-1})									
	$5p$	$6p$	$7p$	$5d$	$6d$	$7d$	$8d$	$4f$	$5f$	$6f$
experiment		2 179.5	909.1	107.0	331.1	179.3	105.4*	-60.4	-309.6*	-106.4*
Cowan	6 417	2 237	911	170	240	130	79	34	-228	-73
FSCC	6 515	2 191	1 139	736	326	172	100	-73	-40	-21
CI+MBPT				162					-620	
experiment [126]	6 508.4	2 179.9		106.1	332.0			-60.5		
RMBPT [139]	6 471			745				-76	-44	
RPTMP[a] [140]								-60	-22	
MCDHF [141]								-71		
FCV [142]								-85		
RHF[a] [143]	5 960			641				-108	-72	

[a] Fine structure splittings deduced from transition wavelengths.

sensitive to details of the calculations. In particular, it is challenging to match theoretical with experimental level energies at a good level of accuracy. On the other hand, the values of V that we obtain are highly stable since they are not sensitive to the separation. If we use the experimental separation $\Delta E_{\rm exp} = 3\,823\,{\rm cm}^{-1}$ and $|V| = 1\,523\,{\rm cm}^{-1}$ from AMBiT, we find the energy shift of the $5d\ ^2D_{5/2}$ level due to interaction with the hole state,

$$\delta = \frac{\Delta E_{\rm exp}}{2}\left(1 - \sqrt{1 - \frac{4V^2}{\Delta E_{\rm exp}^2}}\right), \tag{3.8}$$

yielding $-755\,{\rm cm}^{-1}$. The $5d\ ^2D_{3/2}$ level also shifts down due to interaction with the $4d^9\,5s^2\ ^2D_{3/2}$ hole level. However, the energy difference is three times larger, and since $b \sim 1/\Delta E$, the energy shift is smaller by approximately a factor of 3. We calculate $|V| = 1\,498\,{\rm cm}^{-1}$ for this pair of levels, so Eq. (3.8) gives a level shift of $-181\,{\rm cm}^{-1}$. The change in the $5d$ fine-structure splitting is therefore $-574\,{\rm cm}^{-1}$ which is close to the difference between experiment and the FSCC calculation of $-629\,{\rm cm}^{-1}$.

In support of the role of the configuration interaction on the $5d\ ^2D$ fine structure, FSCC calculations were performed for isoelectronic In^{2+} ions, in which there is a much larger energy difference between the $5d\ ^2D$ term and the doubly excited $4d^9\,5s^2\ ^2D_{5/2}$ level [126]. Thus a better agreement with FSCC calculations is expected. In comparison to Sn^{3+}, for In^{2+} the difference between experiment [126] and FSCC indeed reduces strongly, from a factor of 7 to only 30% (298 versus $398\,{\rm cm}^{-1}$).

Before discussing the impact of configuration interaction on the fine structure of the $5f\ ^2F$ and $6f\ ^2F$ terms we note that the $4f\ ^2F$ exhibits an inverted fine structure with the $J = 7/2$ level being more strongly bound than the $J = 5/2$ level by approximately $60\,{\rm cm}^{-1}$. The occurrence of this inversion of the fine structure and the actual value of the fine-structure interval results from an intricate balance between relativistic, spin-orbit and core polarization effects and has been the subject of a variety of theoretical approaches calculating the $4f\ ^2F$ fine structure along the isoelectronic sequence of Ag-like ions [139–143].

We confirm the fine structure of the $4f\ ^2F$ term by measuring the wavelengths of the transitions from the $5g\ ^2G$ levels and the transitions to the $5d\ ^2D$ levels. Weaker transitions from the $6d\ ^2D$ term to the doubly excited $4d^9\,5s^2\ ^2D_{5/2}$ level are observed additionally. A comparison of the fine-structure splitting of the observed $nf\ ^2F$ levels with theoretical calculations is given in Table 3.5. Both measurements and theoretical calculations agree on an inverted fine structure splitting for these $nf\ ^2F$ terms. However the magnitude of the fine structure splitting of the $5f$ and $6f$ terms are much smaller than our experimental ones.

In similar fashion to the $5d\ ^2D$ levels, the $5f\ ^2F$ fine-structure splitting is strongly affected by interaction with hole states. However, the $5f\ ^2F$ case is more complicated because the $4d^9\,5s\,5p$ configuration has seven configuration state functions (CSFs) with $J = 5/2$ and four CSFs with $J = 7/2$. The CSFs tend to be strongly mixed with each other

TABLE 3.6: Sn IV $4d^9\,5s\,5p$ level energies as candidates for possible configuration interaction with the nf levels. The level energies are obtained from Cowan code calculations published in Ref. [132]. The matrix elements $|V_{i,5f}|$ are calculated using the AMBiT code. The resulting shift of the $5f$ level by configuration interaction by the level is given by δ_{5f}. The $J = 5/2$ levels interacts with the $5f\,^2F_{5/2}$, similarly the $J = 7/2$ levels with $5f\,^2F_{7/2}$.

E_i (cm^{-1}) [132]	J	$\lvert V_{i,5f}\rvert$	δ_{5f}
226 363	5/2	3	0
231 318	5/2	484	11
239 582	5/2	765	47
242 203	5/2	622	39
249 541	5/2	41	1
263 718	5/2	111	-1
269 440	5/2	1341	-104
231 090	7/2	72	0
239 920	7/2	417	15
246 851	7/2	601	72
260 398	7/2	2404	-676

and, also, have small contributions of CSFs belonging to other configurations. Therefore, rather than treat the system as a few-level system, we use the approach of perturbation theory.

Using AMBiT we obtain energies for the $4d^9\,5s\,5p$ levels as well as a mixing coefficient. At first order in perturbation theory, the coefficient of ψ_{5f} in the level ψ_i is simply

$$b_{5f} = \frac{V_{i,5f}}{E_i - E_{5f}}.$$

From our AMBiT values of b_{5f} and E_i, we extract values for the matrix element $V_{i,5f}$. Again, these are relatively stable for different calculations, even though the energies and b coefficients can change dramatically.

The corresponding energy shift of the $5f$ level is $\delta_{5f} = V_{i,5f}^2/\Delta E_{\mathrm{exp}}$. Unfortunately we do not have precise experimental determinations of most of the interaction $4d^9\,5s\,5p$ levels. Instead we use the results of Cowan calculations (Ref. [132]) to obtain an approximation to the level shifts. The results are presented in Table 3.6.

We see that while each of the $5f$ levels are shifted by interactions with the hole levels, the change in the fine-structure splitting is dominated by the interaction of the $5f\,^2F_{7/2}$ level with a hole state at 260 398 cm^{-1}. The final expected shift is 580 cm^{-1}, overestimating the actual difference between experimental fine-structure and FSCC calculations of 270 cm^{-1}. Nevertheless, given the uncertainties in our estimation of V and the location of the doubly excited levels, we arrive at a plausible explanation for the observed anomaly.

A similar explanation can be given for the observed difference in fine structure splitting for the $6f\ ^2F$ term, interacting with the high-lying levels in the same series of hole states. Because the energy differences between these levels are larger, this effect may reasonably be expected to be smaller than for the $5f\ ^2F$ levels. Likewise, the $7p\ ^2P$ is expected to interact with several doubly excited levels.

We also performed Cowan calculations to investigate the terms described above. The number of fitted parameters in this case is reduced by tying the Hartree-Fock ratios to the spin-orbit parameters for the np, nd, and nf levels. The $4d^9\,5s5p$ levels are taken from Ref. [132] (included in Table 3.6). The two $4d^9\,5s^2\ ^2D$ levels were calculated with two adjustable parameters. All interaction parameters were fixed at 0.8 of their Hartree-Fock values. The number of levels determined was insufficient to more accurately fit the parameters. Results of the calculation are included in Table 3.5 and show good agreement with the experimental results, although the inversion of the $4f\ ^2F$ level is not reproduced. The agreement for all other nf and the np and nd levels underlines the significant role of configuration interaction in a quasi-one-electron system like Sn^{3+}.

3.6 Conclusion

Optical techniques are useful diagnostics in plasma sources of EUV light in nanolithography. We present the ultraviolet and optical spectra of a laser-produced tin plasma. The lines belonging to Sn^{3+} are identified using a convenient masking technique. The 33 newly found lines are used to determine 13 new configurations with iterative guidance from Cowan code calculations. The level energies are verified using a quantum-defect scaling procedure, leading to the refinement of the ionization limit to $328\,908.4\,cm^{-1}$ with an uncertainty of $2.1\,cm^{-1}$. FSCC calculations are generally in good agreement with present measurements. The anomalous behavior of the $5d\ ^2D$ and $nf\ ^2D$ terms is shown to arise from configuration interaction with doubly excited levels by joining the strengths of FSCC, Cowan and CI+MBPT approaches.

3.7 Acknowledgments

Part of this work has been carried out at the Advanced Research Center for Nanolithography, a public-private partnership between the University of Amsterdam, the Vrije Universiteit Amsterdam, the Netherlands Organization for Scientific Research (NWO), and the semiconductor equipment manufacturer ASML.

4

Time- and space-resolved optical Stark spectroscopy in the afterglow of laser-produced tin-droplet plasma

J. Scheers, R. Schupp, R. Meijer, W. Ubachs, R. Hoekstra, and O. O. Versolato

Physical Review E **102**, 013204 (2020)

The afterglow emission from Nd:YAG-laser-produced microdroplet-tin plasma is investigated, with a focus on analyzing Stark effect phenomena and the dynamical evolution of the plasma. Time- and space-resolved optical imaging spectroscopy is performed on 11 lines from Sn I–IV ions, in the 315–425 nm wavelength range. Stark shift-to-width ratios serve as the basis for unambiguous experimental tests of atomic physics theory predictions. Experiment and theory, where available, are found to be in poor agreement, and are in disagreement regarding the sign of the ratio in several cases. Spectroscopic measurements of the Stark widths in tandem with Saha-Boltzmann fits to Sn I and Sn II lines, establish the evolution of the local temperature and density of the plasma afterglow, 20–40 ns after the end of the 15-ns-long temporally box-shaped laser pulse. A clear cool-down from $\sim$2 to 1 eV is observed of the plasma in this time window, having started at $\sim$30 eV when emitting extreme ultraviolet (EUV) light. An exponential reduction of the density of the plasma from $\sim 10^{18}$–$10^{17}\ e^{-}\ \mathrm{cm}^{-3}$ is observed in this same time window. Our work is relevant for understanding the dynamics of the decaying, expanding plasma in state-of-the-art EUV nanolithography machines.

4.1 Introduction

Laser-produced tin plasma is used in state-of-the-art extreme ultraviolet (EUV) nanolithography machines where highly charged tin ions produce the required EUV light. Hot (10–100 eV) and dense (10^{19}–10^{21} e^- cm^{-3}) plasma is produced when molten Sn microdroplets are illuminated by high-energy laser pulses [24]. The responsible ions for emitting EUV photons near 13.5 nm are Sn XI–Sn XV with their resonance transitions $4p^6 4d^m$–$4p^5 4d^{m+1}$ and $4d^m$–$4d^{m-1}4f$ (m = 4–0) [12–15, 24]. Besides the lithographically applicable EUV radiation, the laser-matter interaction produces a violently expanding plasma with a broad range of charge states down to neutral Sn I.

Besides the measurement of kinetic energies of ions penetrating into the far field [103], optical spectroscopy is a convenient and versatile plasma diagnostic tool for understanding and monitoring the plasma in its expansion phase, where it has lower temperature and density. Line emission from the relatively low charge states Sn I–IV can readily be identified in the optical domain. Intensities, shapes, and shifts of the lines can provide information about the local plasma conditions, such as temperature and electron density. Light emission from lowly charged tin ions is found in a wide variety of plasma, ranging from the laser-produced Sn plasmas for generating EUV light considered here, to potential plasma heat shields for fusion reactors [109–111, 159], and astrophysical plasma [113–118, 121, 160–164]. Spectral lines of Sn in the optical range are found in various collections by the Atomic Spectra Database maintained by the National Institute of Standards and Technology [64]. Additional, extended lists of line positions are available for Sn II [145], Sn III [146], and Sn IV [165]. The Stark effect, the broadening and shifting of lines mostly due to the interaction of the tin ions with plasma electrons at the densities and temperatures relevant for this work, can be employed to gauge the plasma density using characteristic features of the plasma line emission [41–43, 122–125]. Methods based on the Stark effect require knowledge of the local plasma temperature as well as input on the Stark shift and width parameters (see, e.g., Refs. [44, 166]), typically stemming from theory. Stark broadening parameters for Sn can be found in various compilations [167–170]. Detailed spectroscopic work and theoretical calculations on Stark broadening are available for Sn I [171, 172], Sn II [173–178], Sn III [179, 180], Sn I and II [181–185], Sn II and III [41], Sn II, III, IV [186], and Sn IV [119, 120, 187, 188]. Relevant and typically studied electron temperatures are between 1 eV and 5 eV. Less information is available on Stark shifts. Calculation of the shift parameter is difficult due to possible cancellations of terms in the formulas [44, 189]. All in all, a large body of literature is available, enabling extraction of the physical conditions of plasma expansion. It provides the basic scaffolding for our studies of the afterglow emission from Nd:YAG-laser-produced microdroplet-tin plasma. Specifically, we present time- and space-resolved spectroscopy of 11 lines, in a 315–425 nm wavelength range, of Sn I–IV ions residing in the expanding plasma, several tens of nanoseconds (in the afterglow) after the end of the 15-ns-long,

temporally box-shaped laser pulse. The measured Stark shifts and widths enable obtaining the shift-over-width ratios, which are largely independent of temperature and density at the here relevant densities and ∼1-eV-level temperatures in this afterglow phase. These ratios serve as the basis for unambiguous experimental tests of the available theoretical predictions. Next, we use the literature data for the Stark widths parameters for eight lines of Sn I–IV ions in combination with our time- and space-resolved spectroscopic observations to diagnose the time evolution of the density and temperature of the plasma in this afterglow phase.

4.2 Experiment

The experimental setup consists of a vacuum vessel equipped with multiple viewports for diagnostics purposes. A droplet generator, attached to the top of the setup, dispenses molten tin droplets with a constant diameter of 46 μm. Droplets, ejected at a repetition rate of 10 kHz, fall through a laser sheet created by a HeNe-laser. Scattered laser light, observed on a photon multiplier tube, triggers the plasma illumination laser and acquisition systems. The tin droplets are irradiated with laser pulses from an in-house built Nd:YAG laser system [190]. The laser is operated at a wavelength of 1064 nm and is capable of generating arbitrary pulse shapes. In the experiments, temporally box-shaped pulses of 15 ns duration with a flat-top spatial beam profile (115 μm in diameter) and energies of 270 mJ/pulse are used at a 10-Hz repetition rate. The resulting laser intensity of 1.7×10^{11} W/cm^2 is relevant for the efficient production of EUV light [23]. Hydrogen is introduced in the vacuum vessel as a buffer gas, at a pressure of about 1 mbar, to prevent contamination of viewports. The presence of the buffer gas did not have any measurable influence on the optical spectral emission characteristics as compared to vacuum conditions on the time- and spatial-length scales studied in this work. More detailed descriptions of the experimental setup can be found in Refs. [23, 28].

Imaging spectroscopy is performed by analyzing light emitted from the generated plasma, observed perpendicularly to the laser propagation direction and at 30^o with respect to the horizontal plane. The plasma light first traverses through a quartz vacuum viewport after which it is collected by a bi-convex lens with a focal length of 100 mm. This lens is placed outside of the vacuum at a distance that enables creating a one-to-one projection image of the plasma onto a linear fiber array, with an imaging resolution of several tens of micrometers and an approximate depth-of-field of ∼1-mm at a representative 350-nm wavelength. The fiber array contains 35 quartz fibers with a 100 μm core diameter, in an ordered linear-to-linear configuration. Cladding around each fiber core adds up to an effective diameter of 125 μm, leading to a total size of the fiber array of 4.4 mm. The fiber size sets the effective field of view of the optical system and the spatial resolution is set by the 100 μm core diameter. The imaging system is realigned for each

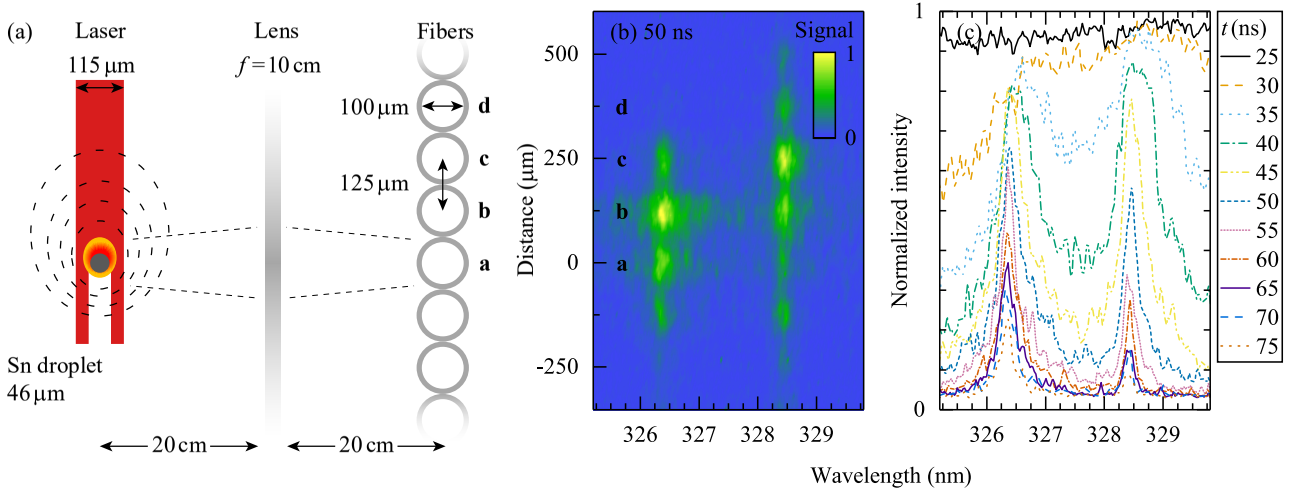

FIGURE 4.1: Schematic layout of the experimental setup. Left: Geometry of the optical system to project plasma emission onto the fiber array. The here relevant fiber cores are labeled **a–d**. Mid: ICCD image capturing emission of Sn I (at $\lambda = 326\,\text{nm}$) and Sn II (at $\lambda = 328\,\text{nm}$) lines from seven fiber cores, covering an approximately 0.9 mm spatial extent of the plasma as a function of wavelength, at time $t = 50\,\text{ns}$. Transitions are detailed in Table 4.1. Right: Time-resolved spectra from fiber core **b**, covering the temporal evolution from 25 to 75 ns.

grating position to correct for chromatic aberrations introduced by the lens, with a position accuracy of approximately ± 1 fiber core, or $\pm 125\mu$m. The fiber array is attached to an imaging spectrometer (Princeton Instruments SCT320) using a re-imaging adapter that images the fiber array onto the slit of the spectrometer.

A grating with a line spacing of 1 200 lines per millimeter, optimized for emission in the ultraviolet range, is employed. A total spectral range from 250 to 430 nm is covered, with a window of about 30 nm for a single frame. We focus our studies on the 315–425 nm wavelength range where bright Sn lines are observed, and well-resolved Sn lines (also when significantly Stark-broadened) are observed. For wavelengths longer than 400 nm a long-pass filter is used to block second-order diffraction from the grating. Wavelength calibration is performed using known Hg lines after exposure to a calibration light source, as well as known "*in vivo*" Sn lines. The instrumental, Gaussian, linewidth is determined from the Hg lines and ranges from 0.17 at 250 nm to 0.14 nm at 430 nm, at full width at half maximum (FWHM). The calibration uncertainty of absolute line positions is 0.02 nm, dominated by limitations set by the sparsity of available Hg lines, and by the complexity of using modestly broadened and in some cases overlapping Sn lines for calibration purposes. Furthermore, imaging artifacts such as finite tilts can influence wavelength calibration but these are below the 0.02 nm level.

The resulting image on the camera mounted to the spectrometer thus contains spectral information as dispersed by the grating in the spectrometer along the horizontal axis and the image of the fiber cores along the vertical axis. For a time-resolved spectral detection an intensified CCD camera (4Picos ICCD) is used. The temporal evolution of the transient plasma is captured by setting the width of a box-gated window at 10 ns. Plasma light is integrated for 1 000 laser shots before read-out in order to capture an adequate amount of light. The use of the ICCD's multichannel plate guarantees full suppression of light produced outside of the 10 ns gated time. Use of the time-resolved CCD camera thus leads to three-dimensional information on the plasma: space, time and wavelength.

In Fig. 4.1 the projection geometry is schematically depicted. In addition, the figure shows a two-dimensional image of space-resolved spectra of two adjacent Sn lines taken at $t = 50$ ns after the start of the laser pulse, extending over seven cores, therewith spanning a spatial image of the plasma of about 0.9 mm. The time evolution of this part of the spectrum is depicted also.

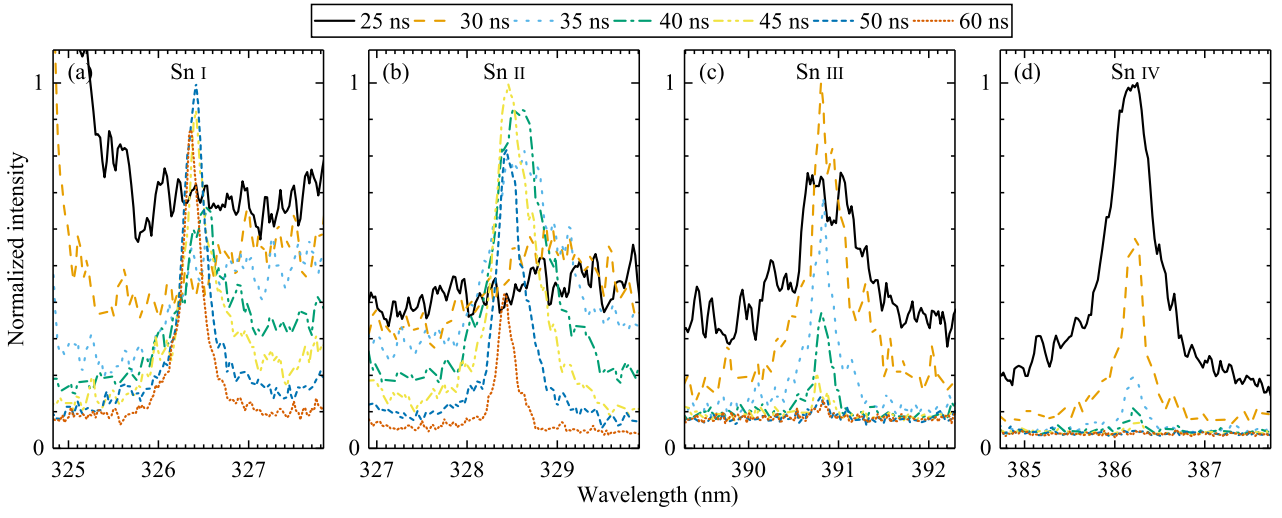

FIGURE 4.2: Time-resolved spectra of selected lines belonging to Sn I–IV. Transitions are detailed in Table 4.1. Lines are individually normalized to their respective maximum in time. Spectra shown are from plasma light captured by fiber core **c**, some +250 µm from the initial droplet position (see Fig. 4.1). Details of the individual transitions are given in Table 4.1. Time is relative to the first moment of the 15-ns-long laser pulse hitting the droplet.

4.3 Measurements

In the following, the Sn I–IV charge state evolution over time, as obtained from the time-resolved measurements, is discussed first. Next, the Stark broadening and shifts of individual and isolated lines of the four charge states are studied and used to obtain shift-to-width ratios. The results are compared to theory predictions where available. Subsequently, in Sec. 4.4, experimental results pertaining to Stark widths of lines from Sn I–IV are used in tandem with Saha-Boltzmann fits to line strengths, to obtain time-resolved temperature and density evolution of the plasma.

4.3.1 Charge-state evolution

Time-resolved spectral measurements are presented in Fig. 4.2. Spectra of plasma light captured by fiber core **c** are shown (see Fig. 4.1). Lines belonging to Sn I–IV are depicted separately to highlight the evolution of the charge state distribution with time. The time of the first measurement frame in which plasma radiation is observed defines $t = 0$, with a systematic uncertainty of approximately ± 5 ns. During the 15-ns-long laser pulse, and in a similarly long period thereafter, strong continuum emission is observed in fiber cores **a** and **b**. Continuum emission is typically first observed in fiber core **a** and soon after it also is strongly visible in fiber core **b**. After this period line emission emerges and starts to dominate the spectrum. Strongly broadened lines belonging to Sn III and IV are first observed at $t = 25$ ns. It takes about 10 ns longer before individual Sn I and II lines can be identified. The spectral width and intensity of all lines quickly reduces with time. Besides the strong broadening, the high plasma density is also apparent through the self-absorption feature observed in a broadened Sn III line at the earliest time (see Fig. 4.2). We note that the large depth of field of our experiment effectively entails an integration of the emission over a plasma column spanning a large density and temperature range. However, most of the emission can be expected to originate from the densest part of the plasma, singling out the dense plasma core [41]. In the following, we focus our studies mostly on spectra obtained from fibers **b**, **c**, and **d** that capture the outflow of plasma from the laser-matter interaction point; fiber core **b** probes the densest observable part of the plasma (see below).

4.3.2 The Stark effect

A widely used method for calculating Stark line widths and shifts is the semiempirical (SE) approach of Griem [191], which is based on the original formulation by Baranger [192]. This generalized impact-broadening theory gives a description of the influence of perturbing electrons on lines subject to the linear Stark effect, neglecting the perturbing plasma ions for the current low densities and, in particular, low temperatures (see, e.g., Ref. [170] and references therein). Following, e.g., the work of de Andrés-García *et al.*

[119] on the SE method, the half width at half maximum (in angular frequency units) linewidth $w_{\rm se}$ of the Lorentz profile resulting from the Stark effect is given by

$$w_{\rm se} \approx 8\left(\frac{\pi}{3}\right)^{3/2}\frac{\hbar}{ma_0}n_e\left(\frac{E_{\rm H}}{kT}\right)^{1/2} \times \sum_{i',f'}\left[|\langle i'|\boldsymbol{r}|i\rangle|^2 g_{\rm se}(\eta_i)+|\langle f'|\boldsymbol{r}|f\rangle|^2 g_{\rm se}(\eta_f)\right]. \tag{4.1}$$

The shift $d_{\rm se}$ from the zero-electron-density position of the line is given, in angular frequency units, by

$$d_{\rm se} \approx -8\left(\frac{\pi}{3}\right)^{3/2}\frac{\hbar}{ma_0}n_e\left(\frac{E_{\rm H}}{kT}\right)^{1/2} \times \sum_{i',f'}\left[\left(\frac{\Delta E_{i'i}}{|\Delta E_{i'i}|}\right)|\langle i'|\boldsymbol{r}|i\rangle|^2 g_{\rm sh}(\eta_i) - \left(\frac{\Delta E_{f'f}}{|\Delta E_{f'f}|}\right)|\langle f'|\boldsymbol{r}|f\rangle|^2 g_{\rm sh}(\eta_f)\right], \tag{4.2}$$

where h is the Planck constant, m is the electron mass, a_0 is the Bohr radius, $n_{\rm e}$ is the electron density, T is the electron temperature, k is the Boltzmann constant, $E_{\rm H}$ is the ionization energy of hydrogen, and $\Delta E_{i'i}$ is the energy difference between a perturbing level i' and the perturbed level i. The indices i and f respectively indicate the upper (initial) and lower (final) levels belonging to the transitions; $\langle i'|\boldsymbol{r}|i\rangle$ denotes the relevant dipole matrix element. The effective Gaunt factors $g_{\rm se}(\eta_i)$ and $g_{\rm sh}(\eta_i)$ are included as a quantum-mechanical correction factor [193, 194]. These factors, of order unity, are slowly varying functions of $\eta_i = E/|\Delta E_{i'i}|$ where E is the mean energy of the perturbing electron, taken to be $E = (3/2)\,kT$. Theoretical calculations of the Stark shift are particularly challenging due to possible cancellation of terms in Eq. (4.2). These cancellations are absent in Eq. (4.1) and all terms add to the overall Stark width.

The dimensionless shift-to-width ratio $d_{\rm se}/w_{\rm se}$,

$$\frac{d_{\rm se}}{w_{\rm se}} \approx \sum_{i',f'}\left[|\langle i'|\boldsymbol{r}|i\rangle|^2 g_{\rm se}(\eta_i)+|\langle f'|\boldsymbol{r}|f\rangle|^2 g_{\rm se}(\eta_f)\right]\Big/ \sum_{i',f'}\left[\left(\frac{\Delta E_{f'f}}{|\Delta E_{f'f}|}\right)|\langle f'|\boldsymbol{r}|f\rangle|^2 g_{\rm sh}(\eta_f) - \left(\frac{\Delta E_{i'i}}{|\Delta E_{i'i}|}\right)|\langle i'|\boldsymbol{r}|i\rangle|^2 g_{\rm sh}(\eta_i)\right], \tag{4.3}$$

is independent of plasma parameters, aside from a possible weak dependence of the Gaunt factors on plasma temperature and uncertainties therein. The FWHM line width w, in wavelength units, is determined from $w = w_{\mathrm{se}}\lambda^2/(\pi c)$, with λ the transition wavelength and c the speed of light. In this work the d/w ratio is used, based on the experimentally established FWHM width w and shift d in units of wavelength. This ratio serves as the basis for experimental tests of theory predictions.

In Fig. 4.3, Lorentzian widths and shifts are displayed for the same transitions as shown in Fig. 4.2. These quantities are obtained from fitting Voigt functions to the spectral lines, which are convolutions of a Gaussian component representing the spectrometer's instrumental width, and a Lorentzian component representing the Stark effect. Doppler broadening is negligible at the 10^{-5} level. The fitting of more complex line profiles that could account for further broadening or other line-shape effects (see, e.g., Refs. [195, 196]) are beyond the scope of this work. The respective Gaussian components are kept fixed at the value of the instrumental width obtained in the calibration procedure (nominally $\Delta\lambda = 0.2\,\mathrm{nm}$). The Lorentzian components obtained from Voigt fits to the spectra obtained from three fiber cores **b**, **c**, and **d** (see Fig. 4.1) are shown along with their respective shifts.

The data displayed in Fig. 4.3 demonstrate that width-to-shift ratios, and thus their inverse the shift-to-width ratios d/w are indeed constant. Solid straight lines represent linear fits to the concatenated data with free slope and intercepts. Self-absorption effects such as those observed at the densest, earliest times for a broadened Sn III line (see Fig. 4.2) may affect the interpretation of Stark line broadening. The potential impact of such opacity broadening may be assessed studying possible deviations from a straight line in the given shift-to-width ratios. Some deviations at the highest of densities may be tentatively identified but these do not significantly influence the fit. In all cases, the intercepts are consistent with the spectral line positions as listed in the available literature (see Table 4.1). The slopes represent the shift-to-width ratios d/w. A complete list of the current results pertaining to d/w ratios is given in Table 4.1 after careful selection of lines that are both sufficiently intense and sufficiently far separated from other lines. Values extracted from the available literature are normalized to an electron density of $10^{17}\,e^-\,\mathrm{cm}^{-3}$ and a temperature of 1 eV (assuming a $T^{-1/2}$ dependency).

Our results are in good agreement with the available experimental work on Stark parameters. For the following comparison to model predictions, we note that the shift-to-width ratios are predicted to change negligibly (e.g., $<1\%$ in the case of the here studied Sn IV lines [119]) over the here relevant temperature range.

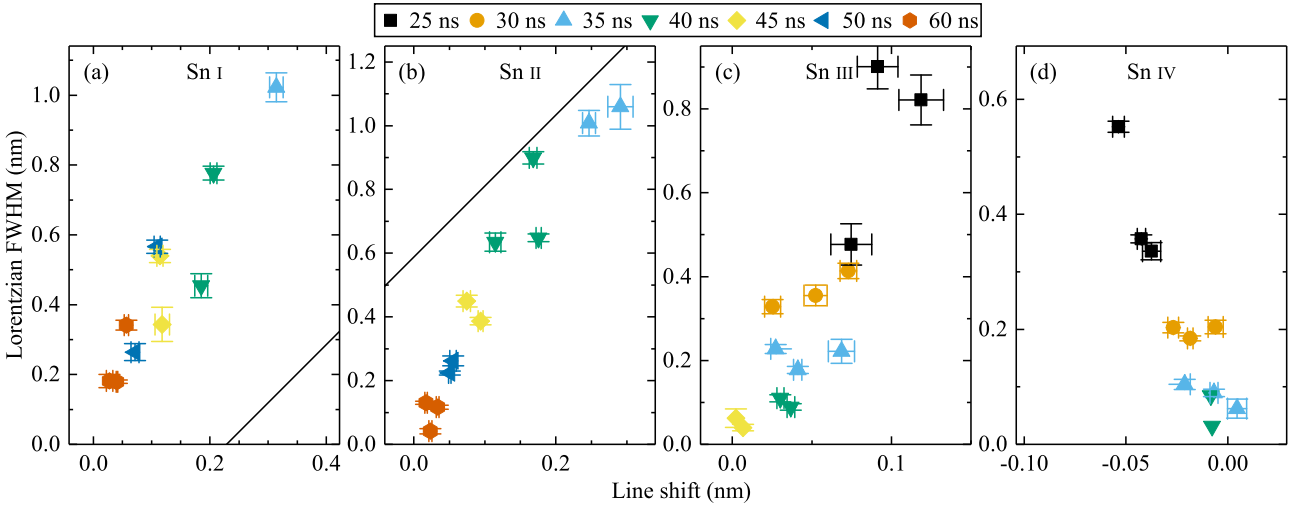

FIGURE 4.3: Lorentzian widths against line shifts as obtained from fitting Voigt functions (with the respective Gaussian component inferred from nearby calibration lines) of the lines shown in Fig. 4.2. The shift is given with respect to literature values for the line position, listed in Table 4.1. The results from the three fiber cores **b**, **c**, and **d** are shown (see Fig. 4.1). The error bars represent one-standard-deviation of the fit uncertainties. Solid straight lines represent linear fits to the data.

Sn I

Stark broadening of Sn I lines has been investigated in several experimental [172, 182–185] and theoretical [171, 181] studies. We observe three Sn I lines at wavelengths near 320 nm, all $5p^2$–$5p6s$ transitions. Experimental Stark widths for these lines are presented in Refs. [182–184]. The values reported by Ref. [184] are a factor of 2–4 lower than presented by the other authors [182, 183].

Experimental studies on the sign of the Stark shift of Sn I lines are presented in Ref. [197], as part of a systematic study on the neutral atoms in the carbon group. No quantitative data on the magnitude of the shift are available in the literature. Our findings agree with the findings in Ref. [197] that the $5p^2\ {}^3P_2$–$5p6s\ {}^3P_1$ transition shifts towards longer wavelength; as do the other $5p^2$–$5p6s$ transitions (see Table 4.1).

Sn II

Both experimental [177, 182, 184, 185] and theoretical [178] Stark effect data is available for the lines of Sn II studied here. Theory predictions are in good agreement with our findings for the $5s5p^2\ {}^2D_{5/2}$–$5s^24f\ {}^2F_{5/2}$ transition, whereas a discrepancy can be identified for the other line of the multiplet, the $5s5p^2\ {}^2D_{3/2}$–$5s^24f\ {}^2F_{5/2}$. In comparing our findings with previous experiments (see Table 4.1) excellent agreement is found for the d/w ratio.

Sn III

Several experimental studies on the Stark broadening of Sn III lines were previously conducted [41, 179, 186], albeit in a wavelength regime generally below 300 nm, outside the range of our studies. SE calculations for a more complete set of transitions are presented in Ref. [180]. These calculations are in good agreement with previously available experimental data. The two Sn III lines studied in this work both shift towards longer wavelength. The SE calculations, however, predict a negative shift for the $5s5d\ {}^1D_2$–$4f5s\ {}^1F_3$ transition and a positive shift for the $5s6p\ {}^1P_1$–$5s6d\ {}^1D_2$ transition (see Table 4.1).

Sn IV

In the case of Sn IV, various experimental results for a selection of lines are available [186–188]. Our experimental findings are in excellent agreement with these previous findings, where available. Theoretical calculations, using a modified-SE method, of a selection of lines can be found in Ref. [120]. SE calculations for a larger set of transitions are presented in Ref. [119] and these are used for the comparison of d/w ratios in Table 4.1. Our experimental findings are in disagreement with the calculations of the shift-over-width values. In two out of the four cases this disagreement extends to the sign of the Stark shift.

TABLE 4.1: Stark width and shift parameters for selected lines in Sn I–IV. The Stark widths (at FWHM) are given at an electron density of $10^{17}\,e^-\,\mathrm{cm}^{-3}$ and are scaled to a temperature of 1 eV (given a $T^{-1/2}$ dependence). Shift-over-width ratios d/w are the resulting slopes of fitted linear functions on concatenated data, shown for selected lines in Fig. 4.3. The uncertainty on the fitted slope is listed between brackets. A positive shift is towards longer wavelength.

				d/w		
Sn ion	Transition	Wavelength (nm)	Stark width (nm)	Exp.	Exp. (others)	Theory
I	$5p^2\ ^3P_2$–$5p6s\ ^3P_1$	317.60 [64]	0.093[a,b] [183], 0.025[a] [184]	0.32(5)	+* [197]	
I	$5p^2\ ^1D_2$–$5p6s\ ^1P_1$	326.33 [64]	0.074[a,b] [183], 0.036[a] [184], 0.080[a] [182]	0.34(6)		
I	$5p^2\ ^1D_2$–$5p6s\ ^3P_2$	333.16 [64]	0.045[a] [184]	0.6(1)		
II	$5s5p^2\ ^2D_{3/2}$–$5s^24f\ ^2F_{5/2}$	328.41 [64]	0.23[a,b] [185], 0.022[a] [177], 0.038[a] [184], 0.16[d] [178], 0.13[a] [182]	0.26(2)	0.22 [177]	0.38 [178]
II	$5s5p^2\ ^2D_{5/2}$–$5s^24f\ ^2F_{5/2}$	335.29 [64]	0.25[a,b] [185], 0.047[a] [177], 0.044[a] [184], 0.24[d] [178]	0.24(2)	0.20 [177]	0.21 [178]
III	$5s6p\ ^1P_1$–$5s6d\ ^1D_2$	370.87 [146]	0.11[b,d] [180]	0.28(4)		0.38 [180]
III	$5s5d\ ^1D_2$–$4f5s\ ^1F_3$	390.79 [146]	0.088[b,d] [180]	0.21(6)		-0.11 [180]
IV	$5d\ ^2D_{3/2}$–$6p\ ^2P_{1/2}$	307.25 [165]	0.052[d] [119]	0.05(2)	0.09 [187]	-0.39 [119]
IV	$4d^95s^2\ ^2D_{5/2}$–$6p\ ^2P_{3/2}$	324.71 [165]	0.094[d] [119]	0.19(5)		-0.49 [119]
IV	$6s\ ^2S_{1/2}$–$6p\ ^2P_{3/2}$	386.23 [165]	0.059[b,d] [120], 0.11[d] [119]	-0.12(1)	-0.1 [187]	-0.38 [119]
IV	$6s\ ^2S_{1/2}$–$6p\ ^2P_{1/2}$	421.73 [165]	0.064[b,d] [120], 0.087[d] [119]	-0.17(2)	-0.2 [187]	-0.48 [119]

[a] Experimental value.
[b] Parameter is used in Fig. 4.3.
[c] Only the sign of the shift was established in Ref. [197]
[d] Theoretical value.

4.4 Diagnostics of the afterglow of laser-produced plasma

The Nd:YAG-laser-produced tin plasma relevant for the production of extreme ultraviolet light is hot ($\sim$30 eV) and dense ($\sim 10^{21}\, e^-\,\mathrm{cm}^{-3}$) (see, e.g., Refs. [23, 32, 35]). At the laser intensity of $1.7 \times 10^{11}\,\mathrm{W/cm^2}$, used in our experiments, given the density set by the laser wavelength [24], the temperature of the plasma produces a charge-state distribution containing mostly Sn XII–Sn XV ions [35] that is optimal for emitting EUV light at 13.5 nm [23, 32]. After the laser pulse ends, the plasma quickly cools down while continuing its free, quasispherical expansion [30]. Optical emission is readily observed in this afterglow phase. Stark widths obtained from lines in this optical domain can assist in diagnosing plasma afterglow regarding its electron density and scaling thereof with time and position.

For the purpose of determining the electron density, the plasma electron temperature T should be known only to a reasonable accuracy, given the rather weak $\sqrt{T}$ dependence of w. The Saha-Boltzmann equation, following the procedure outlined in Ref. [198], can provide the required information based on a fit of observed emission line strengths, as a function of excitation and ionization energies. It assumes local thermodynamic equilibrium (LTE) conditions. Regarding the assumption of LTE, first, we note that the McWhirther criterion [199] for LTE is well met over the here relevant plasma densities and temperatures. Second, we performed FLYCHK [200] calculations of the average charge state $\bar{z}$ over a range of electron temperatures and densities, both under LTE and non-LTE conditions and found no significant differences over the here relevant densities and temperatures.

Figure 4.4 presents our FLYCHK calculations, under LTE conditions, of $\bar{z}$ over the relevant range of electron temperatures and densities. Overlaid on the interpolated FLYCHK output are the allowed solutions in (density, temperature) space resulting from fits of the Saha-Boltzmann equation to emission line strengths of Sn I and Sn II for selected time steps as observed in fiber core **b** (see Fig. 4.1). These allowed solutions are presented by solid lines in Fig. 4.4. These solutions are in broad agreement with estimates (not shown) of the average charge state based just on the ratios of emission line strengths of the various charge states. Uncertainties of up to several tens of percent in our temperature estimation should be taken into account. The dashed, near-vertical lines indicate the allowed solutions in (density, temperature) space resulting from the observed width of the Sn II 328-nm line from fiber core **b**, taking as input the experimentally determined width parameter from Ref. [185]. The intersections of solid and dashed lines, indicated by black dots, identify the unique solutions for electron density and temperature in a time- (and, in principle; space-) resolved manner. A clear reduction of plasma temperature, and a much faster reduction of electron density, is thus observed in the time window from 35 to 55 ns. Given the observed modest change in plasma temperature, and weak dependence of the Stark width on temperatures of $\sim$1 eV, its time evolution is not explicitly considered in the following.

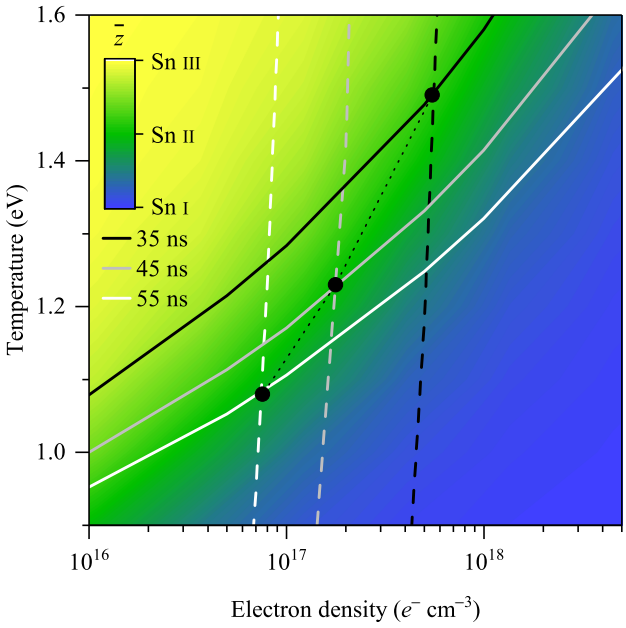

FIGURE 4.4: Color-map of the average charge state $\bar{z}$ as a function of electron density and temperature from FLYCHK calculations [200] in LTE. The solid (near diagonal) lines indicate the solutions allowed by a Saha-Boltzmann fit to Sn I and Sn II lines, performed for each time step for fiber core **b** (see Fig. 4.1). The dashed (near vertical) lines indicate allowed solutions for the electron densities (as a weak function of T) as inferred from the width of the Sn II $5s5p^2\ ^2D_{3/2}$–$5s^24f\ ^2F_{5/2}$ transition at 328 nm line using the experimental input from Ref. [185], see main text. The intersections of solid and dashed lines identify unique solutions for electron density and temperature. Time is relative to the first moment of the 15 ns-long laser pulse hitting the droplet.

Figure 4.5(a) shows the evolution of plasma electron density with time as obtained from fiber core **b** (see Fig. 4.1) from our studies of the two lines (see Table 4.1) from Sn II, taking a constant $T = 1$ eV and using the experimentally determined width parameters from Miller *et al.* [185] who provide values for both here observed Sn II lines. These values agree with those from other experiments [182] and calculations [178] within roughly a factor of 2 that is typical for these complicated experiments and calculations. Experimental values from Ref. [184] are somewhat further removed from the other works. Using the width parameters of Miller *et al.*, both Sn II lines show consistent results regarding electron densities [cf. Fig. 4.5(a)]. An exponential decay of electron density with time is observed, with approximately a decade drop in density every 20 ns. The black solid line shows the result of an exponential fit to the data of the 328-nm line. No significant change in density is observed when shifting the location of our observations $+250\,\mu$m in the direction of the laser origin (fiber core **d**), or $-125\,\mu$m away from it towards the original droplet location (fiber core **a**), as shown in the inset, indicating a spatially rather flat plasma density profile with the highest density observed through fiber core **b**.

Also shown are the plasma densities as derived from linewidths in Sn I, Sn III, and Sn IV ions in panels (b), (c), and (d), respectively. The required theoretical input values for the width parameters at $T = 1$ eV are obtained from Ref. [183] for Sn I, Ref. [182] for Sn III, and Ref. [120] for Sn IV. Note that the various literature values for the broadening parameters may differ again up to a factor of 5 (see Table 4.1). The black solid lines are identical to the one shown in panel (a). Given the uncertainties on the required input values, the agreement between the results obtained from the various charge states at early times is reasonable.

While being aware of the sizable uncertainties involved in the Stark broadening parameters, a charge-state-dependent trend can tentatively be identified in the data. This trend would indicate that the lower charge states appear to probe a higher plasma density, while the higher charge states probe a lower density, all compared to Sn II. These differences increase with time. The trend may originate from our line-of-sight integration of emission intensity. Alternatively, the trend may point towards here unexplored contributions in the Stark parameters that serve as input.

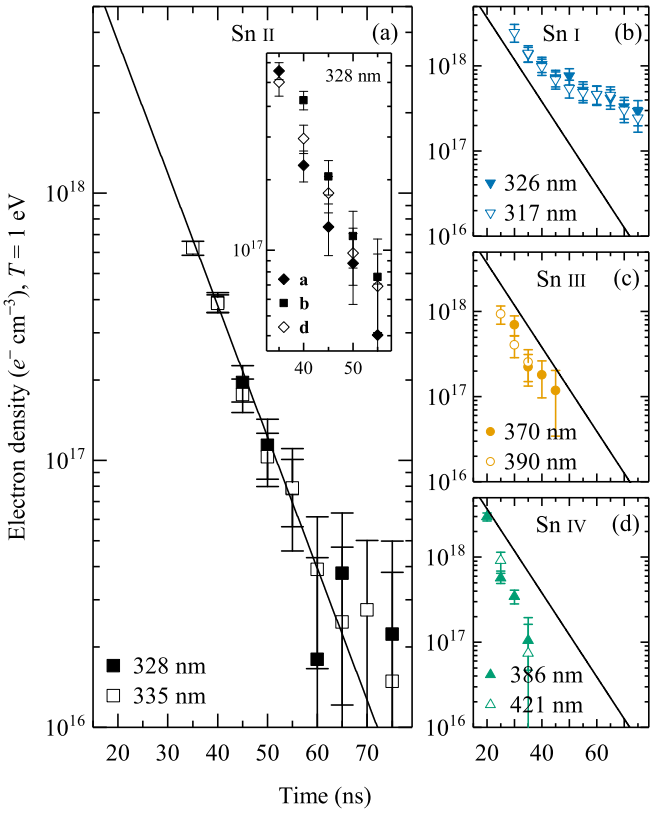

FIGURE 4.5: Plasma electron density determined from measurements taken at fiber core **b** (see Fig. 4.1) as a function of time (relative to the first moment of the 15 ns-long laser pulse hitting the droplet). The densities are calculated using experimental Stark widths in case of Sn II [185], and theoretical widths from Sn I [183], Sn III [182] and Sn IV [120] taken at their $T = 1$ eV values; details are given in Table 4.1. Uncertainty estimates combine uncertainties on the input parameters (a 20% error margin is assumed where no value was provided), with statistical ones and a constant 0.05 nm uncertainty that captures systematic deviations seen, e.g., in Fig. 4.3. The solid black line results from an exponential fit to the 328 nm data of Sn II. The inset in panel (a) shows 328 nm data also from fiber cores **a** and **d** (see Fig. 4.1). Panels (b), (c), and (d) show the densities as derived from lines of Sn I, Sn III, and Sn IV, respectively, from fiber core **b**. The black lines are identical to the one shown in panel (a).

4.5 Conclusion

The Stark effect were observed in optical lines in the emission from laser-produced tin plasma in the afterglow phase 20–40 ns after the end of the 15-ns-long temporally box-shaped laser pulse that illuminates the tin droplets. Time- and space-resolved spectroscopy of Sn I–IV ions was performed on 11 lines from Sn I–IV ions, in an ∼315–425-nm wavelength range. Stark shift-to-width ratios, which are here largely independent of temperature and density, served as the basis for experimental tests of atomic physics theory predictions. These predictions are found to be in poor agreement with the experimental data and cases are found where theory and experiment disagree on the sign of the Stark line shift. Previous experimental input for the Stark width parameter was used, in tandem with Saha-Boltzmann fits of Sn I and Sn II lines, to obtain the temperature and density evolution of the plasma with time. A strong, exponential reduction of density from $\sim 10^{18}$–10^{17} e^- cm^{-3} in a 20 ns time window, was established using the Sn II lines. A clear cool-down from a ∼2 to 1 eV temperature is observed in this same time window, having started at ∼30 eV, and $\sim 10^{21}$ e^- cm^{-3}, when emitting EUV light during the application of the 15 ns-long laser pulse. No significant difference in density was observed from our studies of Sn II when translating the region of observation 250 μm in the direction of the laser beam origin, indicating, locally, a spatially rather flat plasma density profile. Stark widths of the other charge states Sn I, III, and IV gave similar density values at early times but a tentative trend was established where, over time, lower charge states probe higher plasma densities.

Our work is relevant for understanding the interaction of the expanding plasma with the local environment in an EUV nanolithography machine. Future studies could include higher charge states with observable transitions in the deep ultraviolet range to be able to probe the dense part of the plasma most relevant for the production of EUV light.

4.6 Acknowledgments

This work was carried out at the Advanced Research Center for Nanolithography, a public-private partnership between the University of Amsterdam, the Vrije Universiteit Amsterdam, the Netherlands Organization for Scientific Research (NWO), and the semiconductor equipment manufacturer ASML. This project received funding from the European Research Council (ERC) Starting Grant No. 802648 and is part of the VIDI research program with Project No. 15697, which is financed by NWO.

References

[1] J. Bardeen and W. H. Brattain, "The transistor, a semi-conductor triode", Phys. Rev. **74**, 230–231 (1948).

[2] T. Lund, "The apollo command module", in *Early exploration of the moon: ranger to apollo, luna to lunniy korabl* (Springer International Publishing, Cham, 2018), pp. 155–212.

[3] G. E. Moore, "Cramming more components onto integrated circuits", Proc. IEEE **86**, 82–85 (1998).

[4] G. E. Moore, "Progress in digital integrated electronics", Proc. IEDM Tech. Dig., 11–13 (1975).

[5] G. D. Hutcheson, "Moore's law, lithography, and how optics drive the semiconductor industry", in Extreme ultraviolet (EUV) lithography IX, Vol. 10583, edited by K. A. Goldberg (International Society for Optics and Photonics, 2018), pp. 1–14.

[6] C. D. Young, *Enabling semiconductor innovation and growth*, BAML 2018 APAC TMT Conference Taipei, Taiwan, 2018.

[7] C. Wagner and N. Harned, "Lithography gets extreme", Nat. Photonics **4**, 24–26 (2010).

[8] I. Y. Tolstikhina, S. S. Churilov, A. N. Ryabtsev, and K. N. Koshelev, "Atomic tin data", in *EUV sources for lithography*, Vol. 149, edited by V. Bakshi (SPIE Press, 2006), p. 113.

[9] W. Svendsen and G. O'Sullivan, "Statistics and characteristics of XUV transition arrays from laser-produced plasmas of the elements tin through iodine", Phys. Rev. A **50**, 3710–3718 (1994).

[10] S. S. Churilov, R. R. Kildiyarova, A. N. Ryabtsev, A. Kramida, and Y. N. Joshi, "Analysis of the $4d^9$–$4d^8(4f+6p)$ transition array of Sn VI", Phys. Scr. **50**, 463–468 (1994).

[11] V. I. Azarov, Y. N. Joshi, S. S. Churilov, and A. N. Ryabtsev, "Analysis of the $4d^7(4f+6p)$ and $4p^54d^9$ configurations of Sn VII, Sb VIII and Te IX", Phys. Scr. **50**, 642–653 (1994).

[12]G. O'Sullivan, B. Li, R. D'Arcy, P. Dunne, P. Hayden, D. Kilbane, T. McCormack, H. Ohashi, F. O'Reilly, P. Sheridan, E. Sokell, C. Suzuki, and T. Higashiguchi, "Spectroscopy of highly charged ions and its relevance to EUV and soft x-ray source development", J. Phys. B **48**, 144025 (2015).

[13]J. Benschop, V. Banine, S. Lok, and E. Loopstra, "Extreme ultraviolet lithography: Status and prospects", J. Vac. Sci. Technol. B **26**, 2204 (2008).

[14]V. Y. Banine, K. N. Koshelev, and G. H. P. M. Swinkels, "Physical processes in EUV sources for microlithography", J. Phys. D **44**, 253001 (2011).

[15]F. Torretti, F. Liu, M. Bayraktar, J. Scheers, Z. Bouza, W. Ubachs, R. Hoekstra, and O. O. Versolato, "Spectral characterization of an industrial EUV light source for nanolithography", J. Phys. D **53**, 055204 (2019).

[16]S. S. Churilov and A. N. Ryabtsev, "Analysis of the Spectra of In XII–XIV and Sn XIII–XV in the Far-VUV Region", Opt. Spectrosc. **101**, 169–178 (2006).

[17]S. S. Churilov and A. N. Ryabtsev, "Analysis of the $4p^6 4d^7$–$(4p^6 4d^6 4f + 4p^5 4d^8)$ transitions in the Sn VIII spectrum", Opt. Spectrosc. **100**, 660–666 (2006).

[18]S. S. Churilov and A. N. Ryabtsev, "Analyses of the Sn IX–Sn XII spectra in the EUV region", Phys. Scr. **73**, 614 (2006).

[19]A. N. Ryabtsev, É. Y. Kononov, and S. S. Churilov, "Spectra of rubidium-like Pd X–Sn XIV ions", Opt. Spectrosc. **105**, 844–850 (2008).

[20]H. Ohashi, S. Suda, H. Tanuma, S. Fujioka, H. Nishimura, K. Nishihara, T. Kai, A. Sasaki, H. A. Sakaue, N. Nakamura, and S. Ohtani, "Complementary spectroscopy of tin ions using ion and electron beams", J. Phys. Conf. Ser. **163**, 012071 (2009).

[21]C. Suzuki, T. Kato, H. A. Sakaue, D. Kato, K. Sato, N. Tamura, S. Sudo, N. Yamamoto, H. Tanuma, H. Ohashi, R. D'Arcy, and G. O'Sullivan, "Analysis of EUV spectra of Sn XIX–XXII observed in low-density plasmas in the Large Helical Device", J. Phys. B **43**, 074027 (2010).

[22]F. Torretti, R. Schupp, D. Kurilovich, A. Bayerle, J. Scheers, W. Ubachs, R. Hoekstra, and O. O. Versolato, "Short-wavelength out-of-band EUV emission from Sn laser-produced plasma", J. Phys. B **51**, 045005 (2018).

[23]R. Schupp, F. Torretti, R. Meijer, M. Bayraktar, J. Scheers, D. Kurilovich, A. Bayerle, K. Eikema, S. Witte, W. Ubachs, R. Hoekstra, and O. Versolato, "Efficient generation of extreme ultraviolet light from Nd:YAG-driven microdroplet-tin plasma", Phys. Rev. Appl. **12**, 014010 (2019).

[24]O. O. Versolato, "Physics of laser-driven tin plasma sources of EUV radiation for nanolithography", Plasma Sources Sci. Technol. **28**, 083001 (2019).

[25]S. Bajt, J. B. Alameda, T. W. B. Jr., W. M. Clift, J. A. Folta, B. B. Kaufmann, and E. A. Spiller, "Improved reflectance and stability of Mo-Si multilayers", Opt. Eng. **41**, 1797–1804 (2002).

[26]D. Kurilovich, T. d. F. Pinto, F. Torretti, R. Schupp, J. Scheers, A. S. Stodolna, H. Gelderblom, K. S. E. Eikema, S. Witte, W. Ubachs, R. Hoekstra, and O. O. Versolato, "Expansion dynamics after laser-induced cavitation in liquid tin microdroplets", Phys. Rev. Applied **10**, 054005 (2018).

[27]D. Kurilovich, M. M. Basko, D. A. Kim, F. Torretti, R. Schupp, J. C. Visschers, J. Scheers, R. Hoekstra, W. Ubachs, and O. O. Versolato, "Power-law scaling of plasma pressure on laser-ablated tin microdroplets", Physics of Plasmas **25**, 012709 (2018).

[28]D. Kurilovich, A. L. Klein, F. Torretti, A. Lassise, R. Hoekstra, W. Ubachs, H. Gelderblom, and O. O. Versolato, "Plasma propulsion of a metallic microdroplet and its deformation upon laser impact", Phys. Rev. Applied **6**, 014018 (2016).

[29]D. Kurilovich, "Laser-induced dynamics of liquid tin microdroplets", PhD thesis (Vrije Universiteit Amsterdam, 2019).

[30]M. M. Basko, V. G. Novikov, and A. S. Grushin, "On the structure of quasi-stationary laser ablation fronts in strongly radiating plasmas", Physics of Plasmas **22**, 053111 (2015).

[31]F. Torretti, "Spectroscopy of highly-charged Sn ions for extreme ultraviolet nanolithography", PhD thesis (Vrije Universiteit Amsterdam, 2019).

[32]R. Schupp, F. Torretti, R. A. Meijer, M. Bayraktar, J. Sheil, J. Scheers, D. Kurilovich, A. Bayerle, A. A. Schafgans, M. Purvis, K. S. E. Eikema, S. Witte, W. Ubachs, R. Hoekstra, and O. O. Versolato, "Radiation transport and scaling of optical depth in Nd:YAG laser-produced microdroplet-tin plasma", Appl. Phys. Lett. **115**, 124101 (2019).

[33]M. Lysaght, D. Kilbane, N. Murphy, A. Cummings, P. Dunne, and G. O'Sullivan, "Opacity of neutral and low ion stages of Sn at the wavelength 13.5 nm used in extreme-ultraviolet lithography", Phys. Rev. A **72**, 014502 (2005).

[34]S. Fujioka, H. Nishimura, K. Nishihara, A. Sasaki, A. Sunahara, T. Okuno, N. Ueda, T. Ando, Y. Tao, Y. Shimada, K. Hashimoto, M. Yamaura, K. Shigemori, M. Nakai, K. Nagai, T. Norimatsu, T. Nishikawa, N. Miyanaga, Y. Izawa, and K. Mima, "Opacity effect on extreme ultraviolet radiation from laser-produced tin plasmas", Phys. Rev. Lett. **95**, 235004 (2005).

[35]F. Torretti, J. Sheil, R. Schupp, M. M. Basko, M. Bayraktar, R. A. Meijer, S. Witte, W. Ubachs, R. Hoekstra, O. O. Versolato, A. J. Neukirch, and J. Colgan, "Prominent radiative contributions from multiply-excited states in laser-produced tin plasma for nanolithography", Nat. Commun. **11**, 2334 (2020).

[36]V. Kaufman, J. Sugar, T. A. M. Van Kleef, and Y. Joshi, "Resonance transitions $4d^{10}5s$–$4d^{9}5s5p$ in the Ag I sequence of In III, Sn IV, Sb V, and Te VI", J. Opt. Soc. Am. A **2**, 426–429 (1985).

[37]H. Ohashi, S. Suda, H. Tanuma, S. Fujioka, H. Nishimura, A. Sasaki, and K. Nishihara, "EUV emission spectra in collisions of multiply charged Sn ions with He and Xe", J. Phys. B **43**, 065204 (2010).

[38]F. Torretti, A. Windberger, A. Ryabtsev, S. Dobrodey, H. Bekker, W. Ubachs, R. Hoekstra, E. V. Kahl, J. C. Berengut, J. R. Crespo López-Urrutia, and O. O. Versolato, "Optical spectroscopy of complex open-4d-shell ions Sn^{7+}–Sn^{10+}", Phys. Rev. A **95**, 042503 (2017).

[39]A. Windberger, F. Torretti, A. Borschevsky, A. Ryabtsev, S. Dobrodey, H. Bekker, E. Eliav, U. Kaldor, W. Ubachs, R. Hoekstra, J. R. Crespo López-Urrutia, and O. O. Versolato, "Analysis of the fine structure of Sn^{11+}–Sn^{14+} ions by optical spectroscopy in an electron-beam ion trap", Phys. Rev. A **94**, 012506 (2016).

[40]J. Scheers, C. Shah, A. Ryabtsev, H. Bekker, F. Torretti, J. Sheil, D. A. Czapski, J. C. Berengut, W. Ubachs, J. R. C. López-Urrutia, R. Hoekstra, and O. O. Versolato, "EUV spectroscopy of highly charged Sn^{13+}–Sn^{15+} ions in an electron-beam ion trap", Phys. Rev. A **101**, 062511 (2020).

[41]E. R. Kieft, J. J. A. M. van der Mullen, G. M. W. Kroesen, V. Banine, and K. N. Koshelev, "Stark broadening experiments on a vacuum arc discharge in tin vapor", Phys. Rev. E **70**, 066402 (2004).

[42]S. Namba, S. Fujioka, H. Sakaguchi, H. Nishimura, Y. Yasuda, K. Nagai, N. Miyanaga, Y. Izawa, K. Mima, K. Sato, and K. Takiyama, "Characterization of out-of-band radiation and plasma parameters in laser-produced Sn plasmas for extreme ultraviolet lithography light sources", J. Appl. Phys. **104**, 013305 (2008).

[43]S. S. Harilal, B. O'Shay, M. S. Tillack, and M. V. Mathew, "Spectroscopic characterization of laser-induced tin plasma", J. Appl. Phys. **98**, 013306 (2005).

[44]H. R. Griem, *Spectral line broadening by plasmas* (Academic Press, 1974).

[45]R. D'Arcy, H. Ohashi, S. Suda, H. Tanuma, S. Fujioka, H. Nishimura, K. Nishihara, C. Suzuki, T. Kato, F. Koike, J. White, and G. O'Sullivan, "Transitions and the effects of configuration interaction in the spectra of Sn XV–Sn XVIII", Phys. Rev. A **79**, 042509 (2009).

[46]C. Suzuki, T. Kato, H. A. Sakaue, D. Kato, I. Murakami, K. Sato, N. Tamura, S. Sudo, N. Yamamoto, H. Tanuma, H. Ohashi, R. D'Arcy, C. S. Harte, and G. O'Sullivan, "Measurement of EUV spectra from high Z elements in the Large Helical Device", AIP Conf. Proc. **1344**, 21–30 (2011).

[47]C. Biedermann, R. Radtke, R. Seidel, and T. Pütterich, "Spectroscopy of highly charged tungsten ions relevant to fusion plasmas", Phys. Scr. **2009**, 014026 (2009).

[48]J. Yatsurugi, E. Watanabe, H. Ohashi, H. A. Sakaue, and N. Nakamura, "EUV spectroscopy of highly charged ions with high-and low-energy EBITs", Phys. Scr. **2011**, 014031 (2011).

[49]S. Ali and N. Nakamura, "High resolution EUV spectroscopy of xenon ions with a compact electron beam ion trap", J. Quant. Spectrosc. Radiat. Transf. **198**, 112–116 (2017).

[50]K. Fahy, E. Sokell, G. O'Sullivan, A. Aguilar, J. M. Pomeroy, J. N. Tan, and J. D. Gillaspy, "Extreme-ultraviolet spectroscopy of highly charged xenon ions created using an electron-beam ion trap", Phys. Rev. A **75**, 032520 (2007).

[51]J. Reader, J. D. Gillaspy, D. Osin, and Y. Ralchenko, "Extreme ultraviolet spectra and analysis of Δn=0 transitions in highly charged barium", J. Phys. B **47**, 145003 (2014).

[52]W. Li, Z. Shi, Y. Yang, J. Xiao, T. Brage, R. Hutton, and Y. Zou, "Tungsten spectroscopy in the EUV range observed at a high-temperature superconducting electron-beam ion trap", Phys. Rev. A **91**, 062501 (2015).

[53]E. Träbert, P. Beiersdorfer, N. S. Brickhouse, and L. Golub, "Low-density laboratory spectra near the He II λ304 line", Astron. Astrophys. **586**, A115 (2016).

[54]J. K. Lepson, P. Beiersdorfer, G. V. Brown, S. M. Kahn, D. A. Liedahl, C. W. Mauche, and S. B. Utter, "Cataloguing emission line spectra from Fe VII–Fe XXIV in the extreme ultraviolet", Rev. Mex. Astron. Astrophys. **9**, 137–139 (2000).

[55]J. K. Lepson, P. Beiersdorfer, G. V. Brown, D. A. Liedahl, S. B. Utter, N. S. Brickhouse, A. K. Dupree, J. S. Kaastra, R. Mewe, and S. M. Kahn, "Emission lines of Fe VII–Fe X in the extreme ultraviolet region, 60–140Å", Astrophys. J. **578**, 648–656 (2002).

[56]J. K. Lepson, P. Beiersdorfer, E. Behar, and S. M. Kahn, "Comparisons of laboratory wavelength measurements with theoretical calculations for neon-like through lithium-like argon, sulfur and silicon", Nucl. Instrum. Methods Phys. Res. B **235**, 131–134 (2005).

[57]I. E. Golovkin, R. C. Mancini, S. J. Louis, R. W. Lee, and L. Klein, "Analysis of X-ray spectral data with genetic algorithms", J. Quant. Spectrosc. Radiat. Transf. **75**, 625–636 (2002).

[58]R. D. Cowan, *The Theory of Atomic Structure and Spectra*, modified by A. Kramida (University of California Press, 1981).

[59]M. F. Gu, "The flexible atomic code", Can. J. Phys. **86**, 675–689 (2008).

[60]K. M. Aggarwal and F. P. Keenan, "Radiative rates for E1, E2, M1, and M2 transitions in Br-like ions with $43 \leq Z \leq 50$", At. Data Nucl. Data Tables **107**, 221–366 (2016).

[61]E. V. Kahl and J. C. Berengut, "AMBiT: A programme for high-precision relativistic atomic structure calculations", Comput. Phys. Comm. **238**, 232–243 (2019).

[62]S. W. Epp, J. R. C. López-Urrutia, M. C. Simon, T. Baumann, G. Brenner, R. Ginzel, N. Guerassimova, V. Mäckel, P. H. Mokler, B. L. Schmitt, H. Tawara, and J. Ullrich, "X-ray laser spectroscopy of highly charged ions at FLASH", J. Phys. B **43**, 194008 (2010).

[63]T. Harada and T. Kita, "Mechanically ruled aberration-corrected concave gratings", Appl. Opt. **19**, 3987–3993 (1980).

[64]A. Kramida, Y. Ralchenko, J. Reader, and N. A. Team, NIST Atomic Spectra Database (ver. 5.5.6), [Online]. Available: `https://physics.nist.gov/asd` [2018, July 3]. National Institute of Standards and Technology, Gaithersburg, MD. 2018.

[65]J. Sugar, W. L. Rowan, and V. Kaufman, "Resonance lines $4p^6$–$4p^5 4d$ of the Kr I isoelectronic sequence", J. Opt. Soc. Am. B **8**, 2026–2027 (1991).

[66]J. Sugar, W. L. Rowan, and V. Kaufman, "Rb-like spectra: Pd X to Nd XXIV", J. Opt. Soc. Am. B **9**, 1959–1961 (1992).

[67]H. Bekker, O. O. Versolato, A. Windberger, N. S. Oreshkina, R. Schupp, T. M. Baumann, Z. Harman, C. H. Keitel, P. O. Schmidt, J. Ullrich, and J. R. C. López-Urrutia, "Identifications of $5s_{1/2}$–$5p_{3/2}$ and $5s^2$–$5s5p$ EUV transitions of promethium-like Pt, Ir, Os and Re", J. Phys. B **48**, 144018 (2015).

[68]Q. Lu, J. He, H. Tian, M. Li, Y. Yang, K. Yao, C. Chen, J. Xiao, J. G. Li, B. Tu, and Y. Zou, "Observation of indirect ionization of W^{7+} in an electron-beam ion-trap plasma", Phys. Rev. A **99**, 042510 (2019).

[69]M. S. Gockenbach, *Finite-dimensional linear algebra* (CRC Press, 2010), p. 361.

[70]M. W. Berry, M. Browne, A. N. Langville, V. P. Pauca, and R. J. Plemmons, "Algorithms and applications for approximate nonnegative matrix factorization", Comput. Stat. Data Anal. **52**, 155–173 (2007).

[71]G. C. Rodrigues, P. Indelicato, J. P. Santos, P. Patté, and F. Parente, "Systematic calculation of total atomic energies of ground state configurations", At. Data Nucl. Data Tables **86**, 117–233 (2004).

[72]A. Kramida, "A suite of atomic structure codes originally developed by R. D. Cowan adapted for Windows-based personal computers", NIST Public DATA Repository, `10.18434/T4/1502500` (2018).

[73]C. Shah, P. Amaro, R. Steinbrügge, C. Beilmann, S. Bernitt, S. Fritzsche, A. Surzhykov, J. R. Crespo López-Urrutia, and S. Tashenov, "Strong higher-order resonant contributions to x-ray line polarization in hot plasmas", Phys. Rev. E **93**, 061201 (2016).

[74]C. Shah, H. Jörg, S. Bernitt, S. Dobrodey, R. Steinbrügge, C. Beilmann, P. Amaro, Z. Hu, S. Weber, S. Fritzsche, A. Surzhykov, J. R. Crespo López-Urrutia, and S. Tashenov, "Polarization measurement of dielectronic recombination transitions in highly charged krypton ions", Phys. Rev. A **92**, 042702 (2015).

[75]R. D'Arcy, H. Ohashi, S. Suda, H. Tanuma, S. Fujioka, H. Nishimura, K. Nishihara, C. Suzuki, T. Kato, F. Koike, A. O'Connor, and G. O'Sullivan, "Identification of $4d$–$5p$ transitions in the spectra of Sn XV–Sn XIX recorded from collisions between Sn ions and He", J. Phys. B **42**, 165207 (2009).

[76]J. O. Ekberg, J. E. Hansen, and J. Reader, "Analysis of the spectrum of seven-times-ionized molybdenum (Mo VIII) and isoelectronic comparison of the spectra Y V–Mo VIII", J. Opt. Soc. Am. **62**, 1143–1148 (1972).

[77]L. J. Curtis and P. S. Ramanujam, "Isoelectronic predictions for ground state ^2P fine structures using the extended regular doublet law", Phys. Scr. **27**, 417–421 (1983).

[78]L. J. Curtis, "Fine-structure intervals for the lowest P terms in the Cu, Zn, Ga, and Br isoelectronic sequences for $Z \leq 92$", Phys. Rev. A **35**, 2089 (1987).

[79]M. Even-Zohar and B. S. Fraenkel, "A study of EUV spectra in the fifth period", J. Phys. B **5**, 1596–1613 (1972).

[80]G. O'Sullivan, J. T. Costello, and P. K. Carroll, "4p–5s transitions in Ag XI to Ag XIV in a laser-produced plasma", J. Phys. B **17**, 345 (1984).

[81]J. T. Costello and G. O'Sullivan, "4p–5s transitions in Cd XII, Cd XIII and Cd XIV", J. Phys. B **17**, 4477–4483 (1984).

[82]J. Reader, "Spectrum and energy levels of four-times ionized yttrium (Y V)", Atoms **4**, 31 (2016).

[83]J. Reader and M. D. Lindsay, "Spectrum and energy levels of five-times ionized zirconium (Zr VI)", Phys. Scr. **91**, 025401 (2016).

[84]J. O. Ekberg, J. E. Hansen, and J. Reader, "Analysis of the spectrum of six-times-ionized niobium Nb VII", J. Opt. Soc. Am. **62**, 1139–1142 (1972).

[85]A. Goyal, I. Khatri, S. Aggarwal, A. K. Singh, and M. Mohan, "Atomic structure calculations for Br-like ions", Can. J. Phys. **93**, 487–495 (2014).

[86]V. A. Dzuba, V. V. Flambaum, and M. G. Kozlov, "Combination of the many-body perturbation theory with the configuration-interaction method", Phys. Rev. A **54**, 3948–3959 (1996).

[87]J. C. Berengut, V. V. Flambaum, and M. G. Kozlov, "Calculation of isotope shifts and relativistic shifts in C I, C II, C III, and C IV", Phys. Rev. A **73**, 012504 (2006).

[88]J. C. Berengut, "Particle-hole configuration interaction and many-body perturbation theory: Application to Hg^+", Phys. Rev. A **94**, 012502 (2016).

[89]V. V. Flambaum and J. S. M. Ginges, "Radiative potential and calculations of QED radiative corrections to energy levels and electromagnetic amplitudes in many-electron atoms", Phys. Rev. A **72**, 052115 (2005).

[90]J. S. M. Ginges and J. C. Berengut, "QED radiative corrections and many-body effects in atoms: vacuum polarization and binding energy shifts in alkali metals", J. Phys. B **49**, 095001 (2016).

[91]J. S. M. Ginges and J. C. Berengut, "Atomic many-body effects and Lamb shifts in alkali metals", Phys. Rev. A **93**, 052509 (2016).

[92] A. J. Geddes, D. A. Czapski, E. V. Kahl, and J. C. Berengut, "Saturated-configuration-interaction calculations for five-valent Ta and Db", Phys. Rev. A **98**, 042508 (2018).

[93] Q. Huang, V. Medvedev, R. van de Kruijs, A. Yakshin, E. Louis, and F. Bijkerk, "Spectral tailoring of nanoscale EUV and soft x-ray multilayer optics", Appl. Phys. Rev. **4**, 011104 (2017).

[94] K. Liu, Y. Li, F. Zhang, and M. Fan, "Transient thermal and structural deformation and its impact on optical performance of projection optics for extreme ultraviolet lithography", Jpn. J. Appl. Phys. **46**, 6568–6572 (2007).

[95] G. Yang and Y. Li, "Analysis and control of thermal and structural deformation of projection optics for 22-nm EUV lithography", in Extreme Ultraviolet (EUV) Lithography III, Vol. 8322 (International Society for Optics and Photonics, 2012), p. 83222V.

[96] A. Kramida, "COWAN code: 50 years of growing impact on atomic physics", Atoms **7**, 64 (2019).

[97] T. M. Baumann, "Spektroskopische Untersuchungen resonanter Rekombinationsprozesse an hochgeladenem Silizium in einer Elektronenstrahl-Ionenfalle", PhD thesis (Ruprecht-Karls-Universität Heidelberg, 2012).

[98] G. Y. Liang, J. R. C. López-Urrutia, T. M. Baumann, S. W. Epp, A. Gonchar, A. Lapierre, P. H. Mokler, M. C. Simon, H. Tawara, V. Mäckel, K. Yao, G. Zhao, Y. Zou, and J. Ullrich, "Experimental investigations of ion charge distributions, effective electron densities, and electron-ion cloud overlap in electron beam ion trap plasma using extreme-ultraviolet spectroscopy", Astrophys. J. **702**, 838–850 (2009).

[99] S. J. Goh, H. J. M. Bastiaens, B. Vratzov, Q. Huang, F. Bijkerk, and K. J. Boller, "Fabrication and characterization of free-standing, high-line-density transmission gratings for the vacuum UV to soft X-ray range", Opt. Express **23**, 4421–4434 (2015).

[100] M. Bayraktar, H. M. J. Bastiaens, C. Bruineman, B. Vratzov, and F. Bijkerk, "Broadband transmission grating spectrometer for measuring the emission spectrum of EUV sources", NEVAC blad **54**, 14–19 (2016).

[101] J. Bauche, C. Bauche-Arnoult, and M. Klapisch, "Transition arrays in the spectra of ionized atoms", Adv. Atom. Mol. Phys. **23**, 131–195 (1988).

[102] J. Bauche, C. Bauche-Arnoult, and O. Peyrusse, *Atomic properties in hot plasmas* (Springer, 2015).

[103] A. Bayerle, M. J. Deuzeman, S. van der Heijden, D. Kurilovich, T. de Faria Pinto, A. Stodolna, S. Witte, K. S. E. Eikema, W. Ubachs, R. Hoekstra, and O. O. Versolato, "Sn ion energy distributions of ns- and ps-laser produced plasmas", Plasma Sourc. Sci. Tech. **27**, 045001 (2018).

[104] S. S. Churilov, Y. N. Joshi, and A. N. Ryabtsev, "The $4d^{10}\ {}^1S_0$–$4d^9$(np+nf) transitions in the Pd I isoelectronic sequence from Cd III to Cs X", J. Phys. B **27**, 5485–5495 (1994).

[105] Y. V. Ralchenko and Y. Maron, "Accelerated recombination due to resonant deexcitation of metastable states", J. Quant. Spectrosc. Radiat. Transf. **71**, 609–621 (2001).

[106] G. J. van het Hof and Y. N. Joshi, "The analysis of the $4d^8$, $4d^7 5s$ and $4d^7 5p$ configurations of six-times ionized tin: Sn VII", Phys. Scr. **48**, 714 (1993).

[107] A. Ryabtsev, R. Kildiyarova, and E. Kononov, "Spectrum of Sn^{5+} in the region 500–1300Å", Atoms **5**, 47 (2017).

[108] M. A. Lysaght, D. Kilbane, A. Cummings, N. Murphy, P. Dunne, P. van Kampen, J. T. Costello, and E. T. Kennedy, "4*d* photoabsorption spectra of Sn II and Sn IV in the 30–65 eV region", J. Phys. B **38**, 4247 (2005).

[109] J. W. Coenen, G. D. Temmerman, G. Federici, V. Philipps, G. Sergienko, G. Strohmayer, A. Terra, B. Unterberg, T. Wegener, and D. C. M. van den Bekerom, "Liquid metals as alternative solution for the power exhaust of future fusion devices: Status and perspective", Phys. Scripta **2014**, 014037 (2014).

[110] G. G. van Eden, T. W. Morgan, D. U. B. Aussems, M. A. van den Berg, K. Bystrov, and M. C. M. van de Sanden, "Self-regulated plasma heat flux mitigation due to liquid Sn vapor shielding", Phys. Rev. Lett. **116**, 135002 (2016).

[111] G. G. Eden, V. Kvon, M. C. M. van de Sanden, and T. W. Morgan, "Oscillatory vapour shielding of liquid metal walls in nuclear fusion devices", Nat. Commun. **8**, 192 (2017).

[112] M. S. Mason and G. Eng, "Understanding tin plasmas in vacuum: A new approach to tin whisker risk assessment", J. Vac. Sci. Technol. A **25**, 1562–1566 (2007).

[113] L. M. Hobbs, D. E. Welty, D. C. Morton, L. Spitzer, and D. G. York, "The interstellar abundances of tin and four other heavy elements", Astrophys. J. **411**, 750–755 (1993).

[114] C. R. Proffitt, C. J. Sansonetti, and J. Reader, "Lead, tin, and germanium in the Small Magellanic Cloud main-sequence B star AV 304", Astrophys. J. **557**, 320 (2001).

[115] P. Chayer, S. Vennes, J. Dupuis, and J. W. Kruk, "Abundance of elements beyond the iron group in cool DO white dwarfs", Astrophys. J. Lett. **630**, L169 (2005).

[116] S. J. Adelman, W. P. Bidelman, and D. M. Pyper, "The peculiar A star Γ Equulei-A line identification study of λλ 3086–3807", Astrophys. J. Suppl. Ser. **40**, 371–424 (1979).

[117] B. D. Savage and K. R. Sembach, "Interstellar abundances from absorption-line observations with the Hubble Space Telescope", Annu. Rev. Astron. Astrophys. **34**, 279–329 (1996).

[118] U. J. Sofia, D. M. Meyer, and J. A. Cardelli, "The abundance of interstellar tin and cadmium", Astrophys. J. Lett. **522**, L137 (1999).

[119] I. de Andrés-García, A. Alonso-Medina, and C. Colón, "Stark widths and shifts for spectral lines of Sn IV", Mon. Not. R. Astron. Soc. **455**, 1145–1155 (2016).

[120]M. S. Dimitrijević, Z. Simić, R. Stamm, J. Rosato, N. Milovanović, and C. Yubero, "Stark broadening of Se IV, Sn IV, Sb IV and Te IV spectral lines", Atoms **6**, 10 (2018).

[121]S. Biswas, A. Das, A. Bhowmik, and S. Majumder, "Accurate estimations of electromagnetic transitions of Sn IV for stellar and interstellar media", Mon. Not. R. Astron. Soc. **477**, 5605–5611 (2018).

[122]A. Roy, S. S. Harilal, S. M. Hassan, A. Endo, T. Mocek, and A. Hassanein, "Collimation of laser-produced plasmas using axial magnetic field", Laser Part. Beams **33**, 175–182 (2015).

[123]R. W. Coons, S. S. Harilal, D. Campos, and A. Hassanein, "Analysis of atomic and ion debris features of laser-produced Sn and Li plasmas", J. Appl. Phys. **108**, 063306 (2010).

[124]H. Lan, H. Lei, D. Zuo, X. Wang, and G. Zheng, "Ion and extreme ultraviolet emission features of CO_2 laser produced Sn and SnO_2 plasmas", Vacuum **135**, 86–92 (2017).

[125]J. Iqbal, R. Ahmed, M. Rafique, M. Anwar-ul Haq, and M. A. Baig, "Spatial diagnostics of the laser-produced tin plasma in air", Laser Phys. **26**, 076001 (2016).

[126]C. E. Moore, *Atomic Energy Levels*, Vol. III (Nat. Bur. Stand., 1958).

[127]J. Reader, C. H. Corliss, W. L. Wiese, and G. A. Martin, "Wavelengths and transition probabilities for atoms and atomic ions: Part 1. Wavelengths, Part 2. Transition probabilities", NSRDS-NBS **68** (1980).

[128]J. A. Carroll, "The vacuum spark spectra of some of the heavier elements, and series classification in the spectra of ionised atoms homologous with copper, silver, and gold", Phil. Trans. R. Soc. A **225**, 357–420 (1926).

[129]K. R. Rao, "Series in the spectrum of trebly-ionised tin (Sn IV)", Proc. Phys. Soc. **39**, 408 (1926).

[130]R. C. Gibbs, A. M. Vieweg, and C. W. Gartlein, "The use of series inductance in vacuum spark spectra", Phys. Rev. **34**, 406 (1929).

[131]R. J. Lang, "The second spark spectrum of antimony and a note on the first spark spectrum of tin", Phys. Rev. **35**, 445 (1930).

[132]A. N. Ryabtsev, S. S. Churilov, and É. Y. Kononov, "Autoionizing and highly excited states in the spectrum of triply ionized tin Sn IV", Opt. Spectr. (USSR) (English Transl.) **100**, 652–659 (2006).

[133]C.-M. Wu, "Atomic spark spectra of tin, Sn III, Sn IV, Sn V", MA thesis (University of British Columbia, 1967).

[134]E. H. Pinnington, J. A. Kernahan, and W. Ansbacher, "Beam-foil measurements of lifetimes of energy levels belonging to Sn III and Sn IV", Can. J. Phys. **65**, 7–12 (1987).

[135]J. A. Kernahan, E. H. Pinnington, W. Ansbacher, and J. L. Bahr, "Experimental mean lives for levels in Sn III and Sn IV", Nucl. Instr. Meth. Phys. Res. B **9**, 616–620 (1985).

[136]T. Andersen, A. K. Nielsen, and G. Sørensen, "A systematic study of atomic lifetimes of levels belonging to the Ag I, Cd I, Au I, and Hg I isoelectronic sequences", Phys. Scripta **6**, 122 (1972).

[137]P. Dunne and G. O'Sullivan, "$4d^{10}5s$–$4d^{9}5s5p$ transitions in Sn IV, Sb V and Te VI", J. Phys. B **25**, L593 (1992).

[138]A. N. Ryabtsev, S. S. Churilov, and E. Y. Kononov, "$4d^{9}5p^{2}$ configuration in the spectra of In III–Te VI", Opt. Spectr. (USSR) (English Transl.) **102**, 354–362 (2007).

[139]U. I. Safronova, I. M. Savukov, M. S. Safronova, and W. R. Johnson, "Third-order relativistic many-body calculations of energies and lifetimes of levels along the silver isoelectronic sequence", Phys. Rev. A **68**, 062505 (2003).

[140]E. P. Ivanova, "Transition probabilities for $5s$–$5p$, $5p$–$5d$, $4f$–$5d$, and $5d$–$5f$ transitions in Ag-like ions with Z = 50–86", At. Data Nucl. Data Tables **97**, 1–22 (2011).

[141]X.-B. Ding, F. Koike, I. Murakami, D. Kato, H. A. Sakaue, C.-Z. Dong, and N. Nakamura, "M1 transition energies and probabilities between the multiplets of the ground state of Ag-like ions with Z = 47–92", J. Phys. B **45**, 035003 (2012).

[142]J. Grumer, R. Zhao, T. Brage, W. Li, S. Huldt, R. Hutton, and Y. Zou, "Coronal lines and the importance of deep-core–valence correlation in Ag-like ions", Phys. Rev. A **89**, 062511 (2014).

[143]K.-T. Cheng and Y.-K. Kim, "Excitation energies and oscillator strengths in the silver isoelectronic sequence", J. Opt. Soc. Am. **69**, 125–131 (1979).

[144]W. F. Meggers, "First spectrum of tin", J. Res. Nat. Bur. Stand. **24**, 153 (1940).

[145]K. Haris, A. Kramida, and A. Tauheed, "Extended and revised analysis of singly ionized tin: Sn II", Phys. Scripta **89**, 115403 (2014).

[146]K. Haris and A. Tauheed, "Revised and extended analysis of doubly ionized tin: Sn III", Phys. Scripta **85**, 055301 (2012).

[147]T. A. M. Van Kleef and Y. N. Joshi, "Analysis of the $4d^{9}5d$, $4d^{8}5s^{2}$ and $4d^{9}6s$ configurations of In IV and Sn V", Phys. Scripta **24**, 557 (1981).

[148]A. N. Ryabtsev, S. S. Churilov, and E. Y. Kononov, "Extended analysis of the Sn V spectrum", Phys. Scripta **72**, 377 (2005).

[149]B. Edlén, "Atomic spectra", in *Spektroskopie I (Handbuch der Physik)* (Springer, 1964), pp. 80–220.

[150]A. E. Kramida, "The program LOPT for least-squares optimization of energy levels", Comput. Phys. Commun. **182**, 419–434 (2011).

[151]C. J. Sansonetti, *Fortran computer code polar*, private communication, 2005.

[152] J. Sucher, "Foundations of the relativistic theory of many-electron atoms", Phys. Rev. A **22**, 348 (1980).

[153] Y. Ishikawa, R. Baretty, and R. C. Binning Jr, "Relativistic Gaussian basis set calculations on one-electron ions with a nucleus of finite extent", Chem. Phys. Lett. **121**, 130–133 (1985).

[154] E. Eliav, M. J. Vilkas, Y. Ishikawa, and U. Kaldor, "Extrapolated intermediate Hamiltonian coupled-cluster approach: Theory and pilot application to electron affinities of alkali atoms", J. Chem. Phys. **122**, 224113 (2005).

[155] G. L. Malli, A. B. F. Da Silva, and Y. Ishikawa, "Universal Gaussian basis set for accurate ab initio relativistic Dirac-Fock calculations", Phys. Rev. A **47**, 143–146 (1993).

[156] TRAFS-3C code (Tel-Aviv Relativistic Atomic Fock-Space coupled cluster code), written by E. Eliav, U. Kaldor and Y. Ishikawa (1990–2013), with contributions by A. Landau.

[157] V. M. Shabaev, I. I. Tupitsyn, and V. A. Yerokhin, "QEDMOD: Fortran program for calculating the model Lamb-shift operator", Comput. Phys. Commun. **189**, 175–181 (2015).

[158] J. C. Berengut, "Isotope shifts and relativistic shifts of Cr II for the study of α variation in quasar absorption spectra", Phys. Rev. A **84**, 052520 (2011).

[159] T. W. Morgan, P. Rindt, G. G. van Eden, V. Kvon, M. A. Jaworksi, and N. J. L. Cardozo, "Liquid metals as a divertor plasma-facing material explored using the Pilot-PSI and Magnum-PSI linear devices", Plasma Phys. Control. Fusion **60**, 014025 (2017).

[160] S. J. O'Toole, "Beyond the iron group: Heavy metals in hot subdwarfs", Astron. Astrophys. **423**, L25–L28 (2004).

[161] S. Vennes, P. Chayer, and J. Dupuis, "Discovery of photospheric germanium in hot DA white dwarfs", Astrophys. J. **622**, L121–L124 (2005).

[162] S. J. O'Toole, J. Simon, and U. Heber, "Abundance studies of sdB stars using UV echelle HST-STIS spectroscopy", Astron. Astrophys. **452**, 579–590 (2006).

[163] K. Werner, T. Rauch, E. Ringat, and J. W. Kruk, "First detection of krypton and xenon in a white dwarf", Astrophys. J. **753**, L7 (2012).

[164] M. Dorsch, M. Latour, and U. Heber, "Heavy metals in intermediate He-rich hot subdwarfs: the chemical composition of HZ 44 and HD 127493", Astron. Astrophys. **630**, A130 (2019).

[165] J. Scheers, A. Ryabtsev, A. Borschevsky, J. C. Berengut, K. Haris, R. Schupp, D. Kurilovich, F. Torretti, A. Bayerle, E. Eliav, W. Ubachs, O. O. Versolato, and R. Hoekstra, "Energy-level structure of Sn^{3+} ions", Phys. Rev. A **98**, 062503 (2018).

[166] A. Hauer, K. G. Whitney, P. C. Kepple, and J. Davis, "Detailed observation and analysis of radiation from high-density laser-imploded targets", Phys. Rev. A **28**, 963–975 (1983).

[167] A. Lesage, "Experimental Stark widths and shifts for spectral lines of neutral and ionized atoms. A critical review of selected data for the period 2001–2007", New Astron. Rev. **52**, 471–535 (2009).

[168] N. Konjević, A. Lesage, J. R. Fuhr, and W. L. Wiese, "Experimental stark widths and shifts for spectral lines of neutral and ionized atoms (a critical review of selected data for the period 1989 through 2000)", J. Phys. Chem. Ref. Data **31**, 819–927 (2002).

[169] A. Kramida and J. R. Fuhr, Atomic Line Broadening Bibliographic Database (version 3.0). [Online] Available: `https://physics.nist.gov/linebrbib` [2020, March 4]. National Institute of Standards and Technology, Gaithersburg, MD.

[170] S. Sahal-Bréchot, M. S. Dimitrijević, and N. Moreau, STARK-B database, [online]. `https://stark-b.obspm.fr` [April 27, 2020]. Observatory of Paris, LERMA and Astronomical Observatory of Belgrade, 2020.

[171] M. S. Dimitrijević and N. Konjević, "Stark broadening of isolated spectral lines of heavy elements in plasmas", J. Quant. Spectrosc. Radiat. Transf. **30**, 45–54 (1983).

[172] S. Djeniže, A. Srećković, J. Labat, R. Konjević, and M. Brnović, "Stark widths and shifts of Sn I, Hg II, Hg III and Pb II spectral lines", Z. Phys. B **24**, 1–4 (1992).

[173] B. Blagojević and N. Konjević, "Semiclassical calculations of electron impact Stark widths and shifts of singly ionized atom lines revisited", J. Quant. Spectrosc. Radiat. Transf. **198**, 9–24 (2017).

[174] J. Purić, M. Ćuk, and I. S. Lakićević, "Regularities and systematic trends in the Stark broadening and shift parameters of spectral lines in plasma", Phys. Rev. A **32**, 1106–1114 (1985).

[175] J. D. Hey and P. Breger, "Stark broadening of isolated lines emitted by singly-ionized tin", J. Quant. Spectrosc. Radiat. Transf. **23**, 311–321 (1980).

[176] I. S. Lakićević and J. Purić, "Stark shift trends in homologous ions", J. Phys. B **16**, 1525–1530 (1983).

[177] S. Djeniže, A. Srećković, and J. Labat, "Stark width and shift of singly-ionized tin spectral lines", Z. Phys. D **17**, 85–86 (1990).

[178] C. Colón, A. Alonso-Medina, C. Rivero, and F. Fernández, "Stark width and shift parameter predictions and regularities of Sn II", Phys. Scr. **73**, 410–419 (2006).

[179] Z. Simić, M. S. Dimitrijević, A. Kovačević, and M. Dačić, "Stark broadening of Sn III lines in a type stellar atmospheres", Publ. Astron. Obs. Belgrade **84**, 487–490 (2008).

[180] A. Alonso-Medina and C. Colón, "Stark broadening of Sn III spectral lines of astrophysical interest: Predictions and regularities", Mon. Not. R. Astron. Soc. **414**, 713–726 (2011).

[181] H. M. Johns, D. P. Kilcrease, J. Colgan, E. J. Judge, J. E. Barefield II, R. C. Wiens, and S. M. Clegg, "Improved electron collisional line broadening for low-temperature ions and neutrals in plasma modeling", J. Phys. B **48**, 224009 (2014).

[182] A. Alonso-Medina and C. Colón, "Measured Stark widths of several Sn I and Sn II spectral lines in a laser-induced plasma", Astrophys. J. **672**, 1286–1291 (2008).

[183] B. Martinez and F. Blanco, "Experimental and theoretical Stark width and shift parameters of neutral and singly ionized tin lines", J. Phys. B **32**, 241–247 (1999).

[184] S. Djeniže, A. Srećković, and Z. Nikolić, "On the Sn I and Sn II Stark broadening", J. Phys. B **39**, 3037–3045 (2006).

[185] M. H. Miller, R. A. Roig, and R. D. Bengtson, "Experimental transition probabilities and Stark-broadening parameters of neutral and singly ionized tin", Phys. Rev. A **20**, 499–506 (1979).

[186] S. Djeniže, "The role of the He I and He II metastables in the population of the Sn II, Sn III and Sn IV ion levels", Spectrochim. Acta, Part B **62**, 403–409 (2007).

[187] M. A. Mazing and N. A. Vrublevskaya, "The broadening of spectral lines in a strongly ionized plasma. III. wavelengths of the lines of multiply charged ions", Opt. Spectr. (USSR) (English Transl.) **16** (1964).

[188] M. Burger, M. Skocic, M. Gavrilov, S. Bukvic, and S. Djenize, "Spectral line characteristics in the Sn IV spectrum", Publ. Atron. Obs. Belgrade **91**, 53–56 (2012).

[189] H. R. Griem, *Principles of Plasma Spectroscopy* (Cambridge University Press, 2005).

[190] R. A. Meijer, A. S. Stodolna, K. S. E. Eikema, and S. Witte, "High-energy Nd:YAG laser system with arbitrary sub-nanosecond pulse shaping capability", Opt. Lett. **42**, 2758–2761 (2017).

[191] H. R. Griem, "Semiempirical formulas for the electron-impact widths and shifts of isolated ion lines in plasmas", Phys. Rev. **165**, 258–266 (1968).

[192] M. Baranger, "General impact theory of pressure broadening", Phys. Rev. **112**, 855–865 (1958).

[193] M. J. Seaton, *Atomic and molecular processes*, edited by D. Bates, Vol. 374 (Academic Press, 1962).

[194] H. van Regemorter, "Rate of collisional excitation in stellar atmospheres", Astrophys. J. **136**, 906 (1962).

[195] V. Milosavljević and G. Poparić, "Atomic spectral line free parameter deconvolution procedure", Phys. Rev. E **63**, 036404 (2001).

[196]N. Konjević, "Plasma broadening and shifting of non-hydrogenic spectral lines: Present status and applications", Phys. Rep. **316**, 339–401 (1999).

[197]E. V. Kondratyeva, "Stark shift in the wavelengths of the spectral lines of Si I, Ge I, Sn I, and Pb I in a spark discharge", Opt. Spectry. (USSR) (English Transl.) **28**, 449–450 (1970).

[198]J. A. Aguilera and C. Aragón, "Characterization of a laser-induced plasma by spatially resolved spectroscopy of neutral atom and ion emissions: Comparison of local and spatially integrated measurements", Spectrochim. Acta B **59**, 1861–1876 (2004).

[199]T. Fujimoto and R. W. P. McWhirter, "Validity criteria for local thermodynamic equilibrium in plasma spectroscopy", Phys. Rev. A **42**, 6588–6601 (1990).

[200]H.-K. Chung, M. H. Chen, W. L. Morgan, Y. Ralchenko, and R. W. Lee, "FLYCHK: Generalized population kinetics and spectral model for rapid spectroscopic analysis for all elements", High Energ. Dens. Phys. **1**, 3–12 (2005).

List of publications

Chapter 1:
J. Scheers, C. Shah, A. Ryabtsev, H. Bekker, F. Torretti, J. Sheil, D. A. Czapski, J. C. Berengut, W. Ubachs, J. R. Crespo López-Urrutia, R. Hoekstra, and O. O. Versolato, "EUV spectroscopy of highly charged Sn^{13+}–Sn^{15+} ions in an electron-beam ion trap", Phys. Rev. A **101**, 062511 (2020).

Chapter 2:
Z. Bouza, **J. Scheers**, A. Ryabtsev, R. Schupp, L. Behnke, C. Shah, J. Sheil, M. Bayraktar, J. R. Crespo López-Urrutia, W. Ubachs, R. Hoekstra, and O. O. Versolato, "EUV spectroscopy of Sn^{5+}–Sn^{10+} ions in an electron-beam ion trap and laser-produced plasmas", J. Phys. B: At. Mol. Opt. Phys. **53**, 195001 (2020)

Chapter 3:
J. Scheers, A. Ryabtsev, A. Borschevsky, J. C. Berengut, K. Haris, R. Schupp, D. Kurilovich, F. Torretti, A. Bayerle, E. Eliav, W. Ubachs, O. O. Versolato, and R. Hoekstra, "Energy-level structure of Sn^{3+} ions", Phys. Rev. A **98**, 062503 (2018).

Chapter 4:
J. Scheers, R. Schupp, R. Meijer, W. Ubachs, R. Hoekstra, and O. O. Versolato, "Time- and space-resolved optical Stark spectroscopy in the afterglow of laser-produced tin-droplet plasma", Phys. Rev. E **102**, 013204 (2020)

The author has also contributed to the following publications:

F. Torretti, R. Schupp, D. Kurilovich, A. Bayerle, **J. Scheers**, W. Ubachs R. Hoekstra, and O. O Versolato, "Short-wavelength out-of-band EUV emission from Sn laser-produced plasma", J. Phys. B: At. Mol. Opt. Phys. **51**, 045005 (2018)

D. Kurilovich, T. de Faria Pinto, F. Torretti, R. Schupp, **J. Scheers**, A. S. Stodolna, H. Gelderblom, K. S. E. Eikema, S. Witte, W. Ubachs, R. Hoekstra, and O. O. Versolato, "Expansion dynamics after laser-induced cavitation in liquid tin microdroplets", Phys. Rev. Appl. **10**, 054005 (2018)

D. Kurilovich, M. M. Basko, D. A. Kim, F. Torretti, R. Schupp, J. C. Visschers, **J. Scheers**, R. Hoekstra, W. Ubachs, and O. O. Versolato, "Power-law scaling of plasma pressure on laser-ablated tin microdroplets", Phys. Plasmas, **25**, 012709 (2018)

R. Schupp, F. Torretti, R. A. Meijer, M. Bayraktar, **J. Scheers**, D. Kurilovich, A. Bayerle, K. S. E. Eikema, S. Witte, W. Ubachs, R. Hoekstra, O. O. Versolato, "Efficient generation of extreme ultraviolet light from Nd:YAG-driven microdroplet-tin plasma", Phys. Rev. Appl. **12**, 014010 (2019)

F. Torretti, F. Liu, M. Bayraktar, **J. Scheers**, Z. Bouza, W. Ubachs, R. Hoekstra, and O. O. Versolato, "Spectral characterization of an industrial EUV light source for nanolithography", J. Phys. D: Appl. Phys. **53**, 055204 (2019)

R. Schupp, F. Torretti, R. A. Meijer, M. Bayraktar, J. Sheil, **J. Scheers**, D. Kurilovich, A. Bayerle, A. A. Schafgans, M. Purvis, K. S. E. Eikema, S. Witte, W. Ubachs, R. Hoekstra, and O. O. Versolato, "Radiation transport and scaling of optical depth in Nd:YAG laser-produced microdroplet-tin plasma", Appl. Phys. Lett. **115**, 124101 (2019)

Acknowledgments

Na bijna vijf jaar onderzoek te hebben gedaan zit het er opeens op. Het was een groot avontuur dat ik heb kunnen doen met behulp van collega's, familie en vrienden die ik hier graag wil bedanken. Oscar, bedankt voor al deze mooie jaren. Je oneindige enthousiasme werkt aanstekelijk. Wim en Ronnie, bedankt voor de hoeveelheid tijd die jullie hebben vrijgemaakt om mij te helpen met mijn onderzoek. Ik zal de levendige discussies nooit vergeten: van complexe fysica tot lijndiktes in figuren, geen detail bleef onbesproken.

De vele uren in het lab waren zeker niet saai door de intensieve samenwerking binnen de groep, ik ben trots op de resultaten die we samen hebben bereikt. Dmitry, Francesco, Ruben, Alex, Bo, Lars, Lucas, Zoi, John, Diko, Mart-Johan, Subam, Klaas, Adam, Javier, Jaap, Job, Paul, Jim, Tiago en Randy wil ik daarvoor hartelijk bedanken. In het bijzonder wil ik mijn paranimfen Ruben en John bedanken voor hun support in de laatste fase van mijn promotietraject. Onze onvergetelijke trip naar de overkant van de oceaan was een mooie belevenis vol spectroscopie en historie. Paul, ondanks dat we helaas geen tin hydrides hebben weten te vinden heb ik een leuke tijd met je gehad. Onze werkzaamheden in het lab waren nooit zover gekomen zonder de hulp van Thomas en Laurens.

Ik heb het werken met diverse mensen van verschillende achtergronden bij ARCNL als erg prettig ervaren, het was inspirerend om aan een gemeenschappelijk thema te werken. Joost en Marjan, mijn complimenten hoe jullie deze groep eigenwijze onderzoekers weten te managen. Onderzoekspartner ASML wil ik bedanken voor het mede mogelijk maken van dit werk. Onze ASML contactpersoon Wim wil ik bedanken voor de interessante discussies over spectra, ik weet nog goed hoe je de volgende slides wist te voorspellen van mijn presentatie over Sn^{3+}. Ook de andere leden van de leescommissie wil ik hierbij bedanken.

De support afdelingen van naburig instituut AMOLF hebben ook bijgedragen aan dit werk. De slimme ontwerpen voor de experimentele opstelling heb ik aan Henk-Jan en Ricardo te danken, van de werkplaats wil ik specifiek Wessel bedanken voor zijn nauwkeurige werkstukken. Duncan, dank voor de boeiende gesprekken over elektronica. De software ontwikkeld door Jorijn en Marco heeft er mede voor gezorgd dat het vierde hoofdstuk er toch nog is gekomen.

De samenwerkingen met andere onderzoekers heb ik altijd als zeer waardevol ervaren. Alexander, bedankt voor de intensieve samenwerking in de afgelopen jaren. Zodra we de Skype verbinding met Troitsk werkend kregen hebben we uren atomaire spectra

besproken. Het was me een genoegen om met je kennis en kunde aan complexe atomaire structuren te werken. Ook dank aan Julian, Anastasia en James, een experimenteel resultaat wordt immers mooier als de theorie hierop aansluit. Julian, dank voor het bedenken van een afkorting, het is jammer dat deze het peer-review proces niet doorstaan heeft. Mijn korte verblijf in het prachtige Heidelberg heeft meer opgeleverd dan waar ik op had gehoopt. Mijn dank gaat uit naar Chintan, Hendrik en José voor de mogelijkheid om bij jullie een deel van mijn onderzoek te mogen doen.

Mijn leven in Amsterdam werd nog leuker door de klimsessies met Rob en Britt, het ontdekken van koffietentjes met Fiona en Anna, de Zeeuwse avonden met Mischa, en mijn huisgenoten op de Foeliestraat met wie het nooit saai was. De eindeloze discussies met Karsten, Thom en Lisa bleven gelukkig ook na het afstuderen nog doorgaan. De tripjes naar Genua en omstreken zorgden voor nodige ontspanning in de afgelopen jaren, waarbij het altijd gezellig was met de nuchtere Zeeuwen Quinten, Justin, Paul, Tim en Daniël.

Graag wil ik ook mijn familie bedanken voor hun steun. In het bijzonder mijn ouders Ruud en Hannie en broer Pim, ik ben blij dat jullie mij steunden om dit te gaan doen. In coronatijd hebben jullie ervoor gezorgd dat ik mijn proefschrift rustig kon afmaken. Voor haar liefde, steun en positiviteit wil ik Charlotte bedanken. Ik hoop er de komende tijd voor jou te kunnen zijn zoals je er ook voor mij was.